



REVIEW

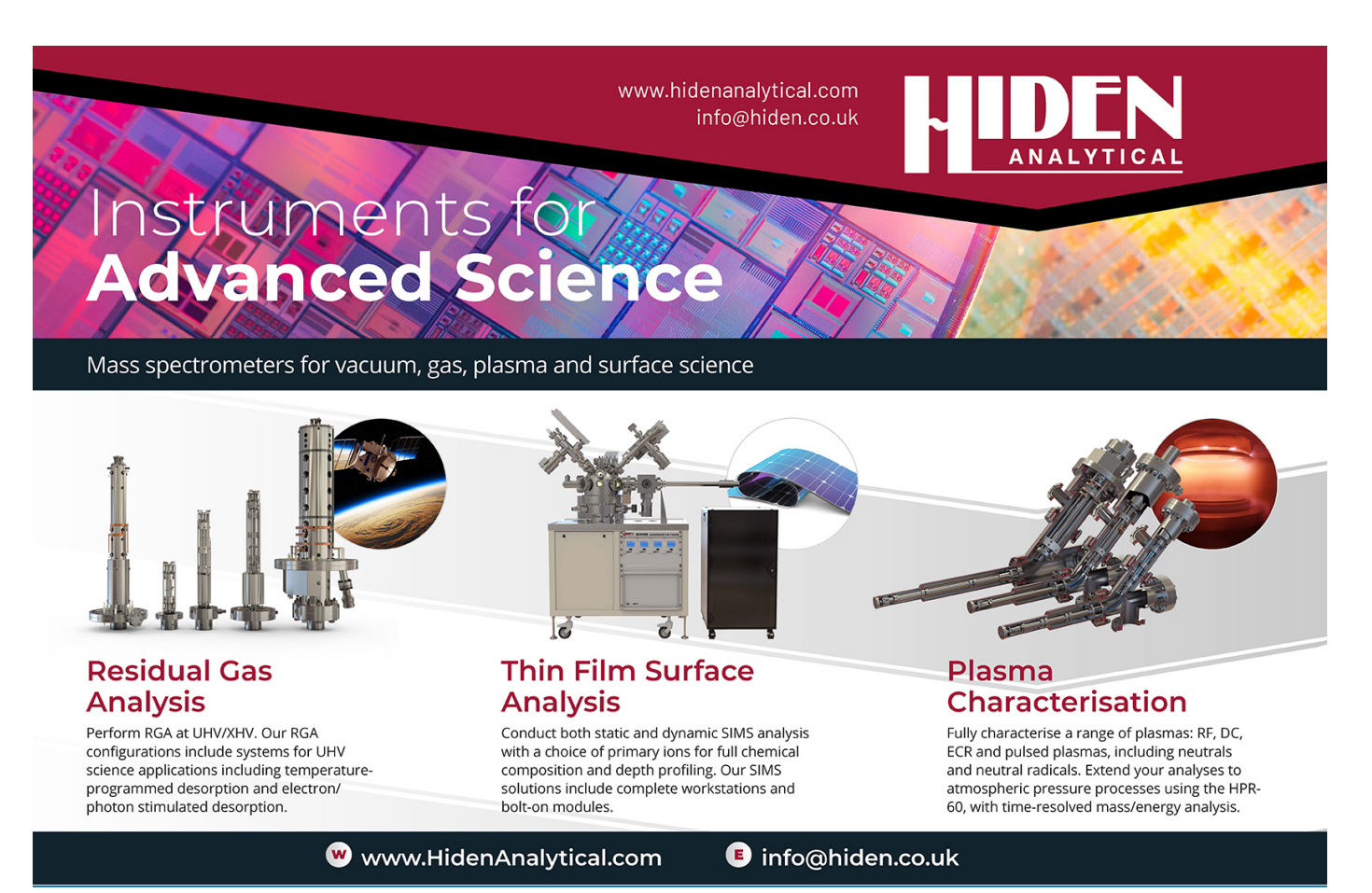
Schottky barrier heights in two-dimensional field-effect transistors: from theory to experiment

To cite this article: Yangyang Wang et al 2021 Rep. Prog. Phys. 84 056501

View the article online for updates and enhancements.

You may also like

- Two-dimensional silicon nanomaterials for optoelectronics
 Xuebiao Deng, Huai Chen and Zhenyu Yang
- Acoustic wave diffraction at the upper edge of a two-dimensional periodic array of finite rigid cylinders. A comprehensive design model of periodicity-based devices
 S. Castiñeira-Ibáñez, C. Rubio and J. V. Sánchez-Pérez
- Quantification of amplitude modulation in wall-bounded turbulence
 Eda Dogan, Ramis Örlü, Davide Gatti et al



Rep. Prog. Phys. 84 (2021) 056501 (50pp)

https://doi.org/10.1088/1361-6633/abf1d4

Review

Schottky barrier heights in two-dimensional field-effect transistors: from theory to experiment

Yangyang Wang^{1,11}, Shiqi Liu^{2,11}, Qiuhui Li^{2,11}, Ruge Quhe^{3,11}, Chen Yang², Ying Guo⁴, Xiuying Zhang², Yuanyuan Pan⁵, Jingzhen Li², Han Zhang⁶, Lin Xu⁷, Bowen Shi², Hao Tang², Ying Li², Jinbo Yang^{2,8,10}, Zhiyong Zhang⁷, Lin Xiao^{1,*}, Feng Pan^{9,*} and Jing Lu^{2,8,7,10,*}

- ¹ Nanophotonics and Optoelectronics Research Center, Qian Xuesen Laboratory of Space Technology, China Academy of Space Technology, Beijing 100094, People's Republic of China
- ² State Key Laboratory for Mesoscopic Physics and Department of Physics, Peking University, Beijing 100871, People's Republic of China
- ³ State Key Laboratory of Information Photonics and Optical Communications and School of Science, Beijing University of Posts and Telecommunications, Beijing 100876, People's Republic of China
- ⁴ School of Physics and Telecommunication Engineering, Shaanxi Key Laboratory of Catalysis, Shaanxi University of Technology, Hanzhong 723001, People's Republic of China
- State Key Laboratory of Heavy Oil Processing, Institute of New Energy, College of Chemical Engineering, China University of Petroleum (East China), Qingdao, 266580, People's Republic of China School of Information Science and Technology, Northwest University, Xi'an, 710127, People's Republic of China
- ⁷ Key Laboratory for the Physics and Chemistry of Nanodevices and Department of Electronics, Peking University, Beijing 100871, People's Republic of China
- ⁸ Collaborative Innovation Center of Quantum Matter, Beijing 100871, People's Republic of China
- ⁹ School of Advanced Materials, Peking University, Shenzhen Graduate School, Shenzhen 518055, People's Republic of China
- ¹⁰ Beijing Key Laboratory for Magnetoelectric Materials and Devices (BKL-MEMD), Beijing 100871, People's Republic of China

E-mail: xiaolin@qxslab.cn, panfeng@pkusz.edu.cn and jinglu@pku.edu.cn

Received 16 May 2020, revised 17 December 2020 Accepted for publication 24 March 2021 Published 27 April 2021



Abstract

Over the past decade, two-dimensional semiconductors (2DSCs) have aroused wide interest due to their extraordinary electronic, magnetic, optical, mechanical, and thermal properties, which hold potential in electronic, optoelectronic, thermoelectric applications, and so forth. The field-effect transistor (FET), a semiconductor gated with at least three terminals, is pervasively exploited as the device geometry for these applications. For lack of effective and stable substitutional doping techniques, direct metal contact is often used in 2DSC FETs to inject carriers. A Schottky barrier (SB) generally exists in the metal–2DSC junction, which significantly affects and even dominates the performance of most 2DSC FETs. Therefore, low SB or Ohmic contact is highly preferred for approaching the intrinsic characteristics of the 2DSC channel. In this review, we systematically introduce the recent progress made in

^{*} Authors to whom any correspondence should be addressed.

¹¹These authors contributed equally to this work. Corresponding Editor: Professor Piers Coleman.

theoretical prediction of the SB height (SBH) in the 2DSC FETs and the efforts made both in theory and experiments to achieve low SB contacts. From the comparison between the theoretical and experimentally observed SBHs, the emerging first-principles quantum transport simulation turns out to be the most powerful theoretical tool to calculate the SBH of a 2DSC FET. Finally, we conclude this review from the viewpoints of state-of-the-art electrode designs for 2DSC FETs.

Keywords: Schottky barrier, two-dimensional materials, transistor, first-principles quantum transport simulation

(Some figures may appear in colour only in the online journal)

1. Introduction

The field-effect transistor (FET), the fundamental building block of the most modern devices, kickstarted the digital revolution and impelled our society into the information age. The critical component of FETs is semiconductors (SCs). Over the last 50 years, transistors based on silicon, the dominant SC material, have kept shrinking in size at the pace of Moore's law. As a result, the information technology industry grows rapidly, fueled by the exponential improvement in performance, speed, and cost per function of every new generation of integrated circuits. However, now it is hard to further sustain Moore's law as the node length beyond 7 nm due to the severe short channel effects in silicon-based transistors [1]. In this context, two dimensional (2D) SCs have come into focus recently owing to their advantages over silicon (figure 1): 1. Atomically thin thickness, leading to enhanced gate control capability; 2. Smooth surface without dangling bond, which reduces the scattering from trap state and roughness and benefits carrier transportation; and 3. Mechanical flexibility, in favor of flexible electronics [2–5]. Therefore, 2DSC is a powerful candidate for the next-generation FET channel materials, especially for sub-7 nm node technology.

The family of 2DSCs now includes a large variety of materials, like transition metal chalcogenides (TMCs), group VA elemental material, group III-V, III-VI, and IV-VI compound materials, which have triggered intensive interests for their diverse characteristics [2-5, 7]. In the 2D limit, the contact properties tend to govern everything and mask the intrinsic properties of 2D materials [8]. Therefore, a low-resistance Ohmic contact is always preferred in 2DSC FETs. However, due to the ultrathin body of 2DSCs, the traditional technique of selective ion implantation is not applicable for 2DSC FETs. Alternative doping schemes such as surface charge transfer suffer from long-term instability or low spatial selectivity [9–12]. Consequently, direct metal contact is often used in 2DSC FETs, and Schottky barrier (SB) is generally established at the metal-2DSC interface, which degrades the device performance significantly. There are two different interface geometries between metal and 2DSCs: top contact and edge contact. The top contact is prevalently adopted due to its simple fabrication process, while the pure edge contact is difficult to make. In some experiments, the metal-2DSC contact is a combination of these two geometries (combined-contact) [13–16].

An essential figure of merit for the metal-2DSC contacts is the SB height (SBH), which regulates the carrier injection efficiency and the extent of performance deterioration. In the ideal case, the SBH can be predicted by the Schottky-Mott rule, that is

$$\Phi_{\mathrm{SB,n}} = W_{\mathrm{M}} - \chi_{\mathrm{S}} \tag{1}$$

$$\Phi_{\rm SB,p} = I_{\rm S} - W_{\rm M} \tag{2}$$

where $\Phi_{\rm SB,n}$ and $\Phi_{\rm SB,p}$ are the SBHs for electrons and holes, respectively, $W_{\rm M}$ is the work function of the metal, $\chi_{\rm S}$, and $I_{\rm S}$ are the electron affinity and ionization potential of the SC, respectively. Unfortunately, owing to the Fermi level pinning (FLP) effect, the SBH generally deviates from the Schottky–Mott rule and thus is hard to be predicted. Although the SBH in 2DSC FETs can be measured experimentally, it is still imperative to develop a prediction technique that is both costand time-effective for state-of-the-art designs.

Herein, we systemically review the latest progress made in theoretical prediction of the SBH in 2DSC FETs and the efforts made both in theory and experiments to achieve low SB contacts in all kinds of 2DSC FETs. Firstly, we focus on the basic concepts about the SB in 2DSC FETs. 2D transistor model and the impact of SB on transport characteristics are illustrated. The causes of the FLP effect are discussed in detail, as well as the different methods, especially the theoretical methods to derive the SBHs. Furthermore, we present an overview of the SBH in FETs based on the different classes of 2DSCs. Comparisons of the SBHs assessed from both the theoretical and experimental methods are provided and highlight the importance of the *ab initio* quantum transport simulation (QTS). Finally, a summary and outlook conclude the paper in the last section.

2. General knowledge of the Schottky barriers in FETs based on two-dimensional semiconductors (2DSCs)

2.1. Fermi level pinning effect

The SBH problem can be roughly stated as 'alignment of the energy levels at an SC-metal interface'. If the Schottky-Mott rule holds, the SBH varies with the work function

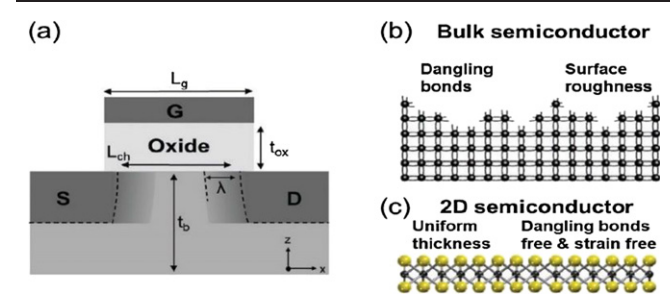


Figure 1. Comparison of 3D bulk SCs with two-dimensional semiconductors (2DSCs) for transistor scaling. (a) Schematic of a typical metal—oxide—semiconductor FET. (b) Schematic illustration of a conventional bulk 3D semiconductor, featured by rich surface dangling bonds, thickness variation, or film discontinuity. (c) Schematic illustration of an atomically thin 2D semiconductor, free of surface dangling-bonds. Reproduced from [6] with permission of the Royal Society of Chemistry.

of the metal electrode $(W_{\rm M})$ with a slope of ± 1 , as indicated by equations (1) and (2). However, the FLP phenomenon is generally observed in experiments; that is, the SBH is insensitive to $W_{\rm M}$. The FLP strength for a specific SC with a group of metals is determined by $S=|\Phi_{\rm SB,n/p}/W_{\rm M}|$. Pinning factor S=1 means no FLP; S=0 indicates a complete FLP, namely, the Fermi level is pinned to a fixed position; and 0 < S < 1 implies partial FLP, namely, the Fermi level is pinned to a certain region.

There are many models to explain FLP, which have been discussed in detail in the review by Tung [17]. Here we list out the factors in regard to 2DSCs. First, an interface dipole forms at the 2DSC-metal contact interface due to the charge redistribution, which can shift the relative energy levels of the 2DSC and metal contact [18–20]. Second, chemical bonding takes place at the 2DSC-metal contact interface and modifies their band structures [13, 21]. Meanwhile, strain and structure distortion may be created by the chemical bonding, working in synergy together, changing the energy levels [22, 23]. Third, metal-induced gap states (MIGS) at the interface. They are the gap states that originate from the tails of the metal Bloch wave functions and penetrate a small distance into the SC. MIGS have a characteristic charge neutral level (CNL). They act as a reservoir for carriers injected from the metal electrode and therefore pin the Fermi level [13, 18, 24, 25]. Fourth, defects and chemical disorders generated during the processes of material and device fabrications lead to defect or chemical disorder-induced gap states in the 2DSC and result in FLP as well [26-29]. For example, crystal damage at or near the interface is caused during the aggressive electron beam metal deposition processes [30]. Yet this factor could be neglected for perfect metal contact interfaces formed through damagefree metal deposition strategies with high-quality 2DSCs [31]. Last, if metal contact forms at or near the end of 2DSCs, dangling bonds or reconstructions at the 2DSC edges lead to surface states, which will be responsible for the FLP as well [17, 32].

After considering the voltage drop $V_{\rm int}$ raised from the interface dipole, the SBH can be written as

$$\Phi_{SB n} = W_{M} - \chi_{S} + eV_{int}. \tag{3}$$

Gap state model [21, 33] assumes that MIGS, defect, and disorder-induced gap states, or surface states fill the 2DSC band gap near the interface with a distribution of electronic states with a density of N (per area per eV) and decay length of δ , and with a charge neutrality level (CNL) of W_0 . The perarea charge of the gap states is thus $eN(\Phi_{SB,n} - W_0)$, which builds an interface dipole and a corresponding voltage difference $\frac{eN\delta}{\varepsilon}(\Phi_{SB,n} - W_0)$, where ε is the dielectric constant around the interface. Then equation (3) is rewritten as

$$\Phi_{\mathrm{SB,n}} = W_{\mathrm{M}} - \chi_{\mathrm{S}} + eV_{\mathrm{int}} - \frac{e^2N\delta}{\varepsilon} (\Phi_{\mathrm{SB,n}} - W_0). \tag{4}$$

We can derive that the pinning factor $S = \frac{1}{1 + \frac{e^2N\delta}{e^2}}$.

2.2. Structure of Schottky barrier in a 2D FET

Here we use the geometry of ML 2DSC-metal top contacts as an illustration since it is simplest and can be easily extended to other configurations. We denote the interface between the metal and ML 2DSC under the metal in the source region (regions A and B) as interface I and the interface between ML 2DSC in the source and channel regions (regions B and C) as interface II. Carriers flow from the electrode into the 2DSC channel mainly through two trajectories: the first one is through interface I and then through interface II into the channel, and the second one is directly from the source metal edge into the channel as shown in figures 2(a)–(c). It has been reported that the carrier injection through interface I is negligible in MoS₂ FETs with Au electrodes in monolayer limits because the region of the MoS₂ film under the contact is depleted [34]. By contrast, considerable contributions from both the two trajectories are found in the ML arsenene FETs with metallic multilayer arsenene electrodes [35] and in ML black phosphorene (BP) FETs with BN-Ni electrodes [36]. Therefore, both the vertical and lateral SBs are analyzed in 2DSC transistors in this paper. The effective SBH (ESBH) of a 2D FET is either the greater one of the vertical and lateral SBHs or the later if the injection from the source metal edge is dominant. The vertical SB at interface I is defined as

$$\Phi_{\rm SB,n}^{\rm V} = E_{\rm c-B} - E_{\rm f} \tag{5}$$

$$\Phi_{\rm SB,p}^{\rm V} = E_{\rm f} - E_{\rm v-B},\tag{6}$$

where $E_{\rm f}$ is the Fermi level of the 2DSC transistor at zero bias, and $E_{\rm c-B}$ and $E_{\rm v-B}$ are the conduction band minimum (CBM) and the valence band maximum (VBM) of the contacted 2DSC (region B), respectively. The lateral SB at interface II is defined as

$$\Phi_{SRn}^{L} = E_{c-II} - E_{f} \tag{7}$$

$$\Phi_{\text{SB,p}}^{\text{L}} = E_{\text{f}} - E_{\text{v-II}},\tag{8}$$

where $E_{\text{c-II}}$ and $E_{\text{v-II}}$ are the conduction and valence band edges of the channel 2DSC at interface II, respectively.

The ML 2DSC-metal top contact in the source region can be classified into van der Waals (vdW) bonding (figures 2(a) and (d)), weak chemical bonding (figures 2(b) and (e)) and strong chemical bonding (figures 2(c) and (f)) according

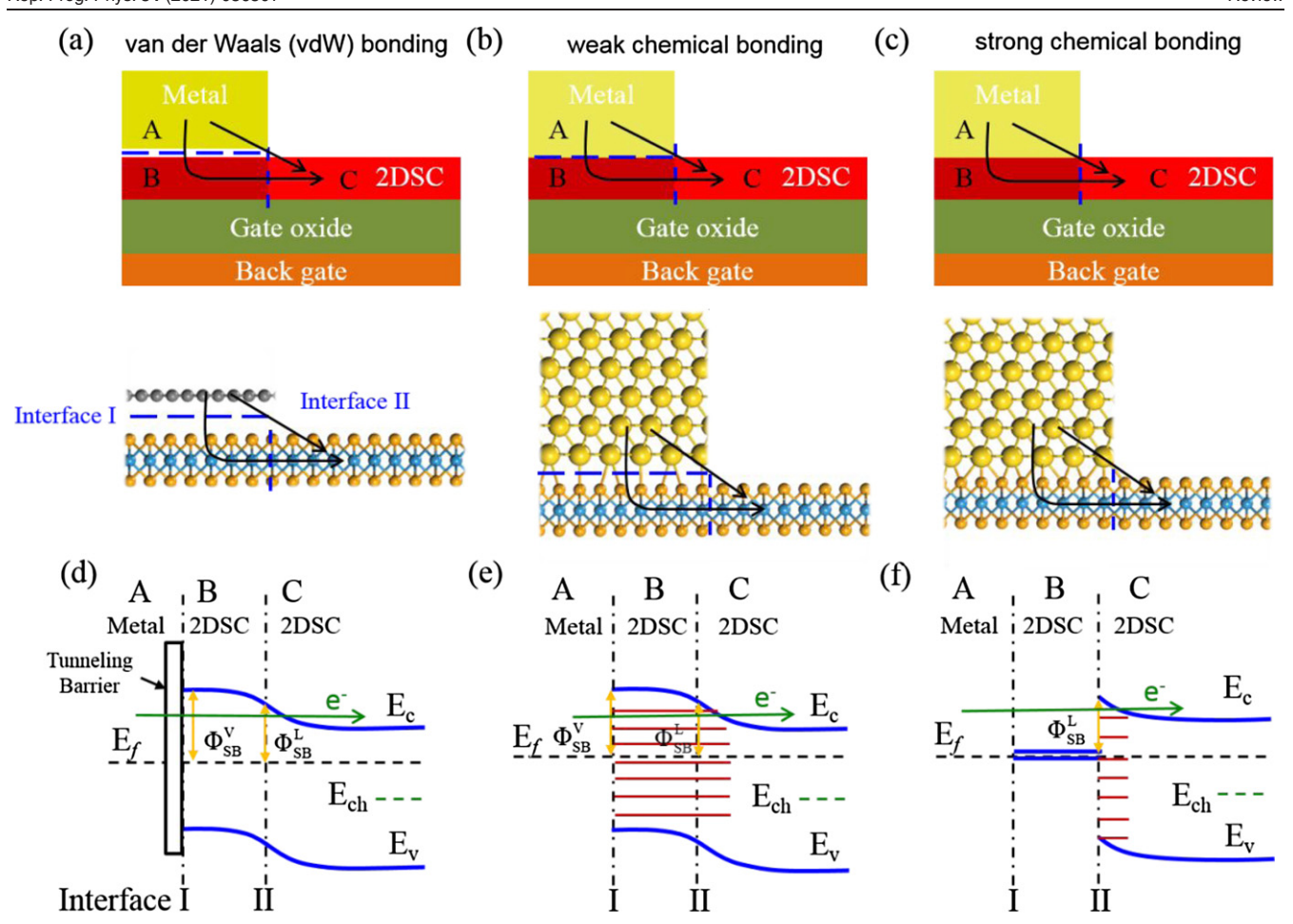


Figure 2. (a)–(c) Schematics and (d)–(f) corresponding band diagrams of a ML 2DSC–metal top contact with the (a) and (d) van der Waals (vdW) bonding type, (b) and (e) weak chemical bonding type, and (c) and (f) strong chemical bonding type in a ML 2DSC FET with top contact electrodes. The SB may form at the interface I and/or II (blue dashed lines in (a)–(c) in the vertical and lateral directions, respectively. A denotes the metal electrode, B the 2DSC under the metal contact, and C the 2DSC channel. The arrows represent the pathways of carrier injection from a metal electrode to the 2DSC channel. In (d)–(f) E_f and E_{ch} are the Fermi levels of the FET and the free-standing channel, respectively. E_c and E_v are the conduction and valence band edges of the 2DSC, respectively. Φ_{SB}^V and Φ_{SB}^L are the vertical and lateral SB, respectively. The red lines denote the gap states.

to the interfacial distance and interaction strength [8, 13]. Such a classification corresponds to very weak adhesion, medium adhesion, and strong adhesion, respectively, proposed by Banerjee et al [13]. The interfacial distance is about 3 Å in the vdW bonding type of contacts, and the band structure of the 2DSC is well preserved without hybridization. Therefore, in FETs with this kind of electrode contact, a tunneling barrier (TB) may exist at interface I due to the large interfacial distance as illustrated in figure 2(d). The SB is formed in the vertical and lateral directions. The vertical SB would be different from the lateral one when a band bending of region B occurs. The band bending or a built-in potential in region B is induced by the charge transfers between regions B and C and is observed in the weak and medium adhesion contacts, where FLP is absent or weak. The example can be found in the ML antimonene transistor with graphene electrodes (weak adhesion) (section 3.1.4) and in the ML MoS₂ transistors with Pt electrodes (medium adhesion) (section 4.1.4). If the band edges are flat in region B at zero bias, the vertical and lateral SBHs are equal to each other. No MIGS exist because of the non-damaging ultraclean vdW interface. Therefore, FLP is rather weak as *S* approaches 1 [31, 37]. More intriguing is that the SBH is regulable by gates when graphene, the first synthesized 2D half-metal, is used as the back electrodes [38–40]. The Fermi level of graphene is gate tunable due to the finite density states, which makes the SBH tunable toward Ohmic contact. 2D material like graphene, h-BN, etc, are also utilized as the buffer layer between the common metals with ultralow or high work function (for example, Co, Ni, or Pt) and 2DSCs to obtain a sharp clean vdW interface, thereby avoiding the FLP and achieving a reduced and even demolished SBH [41–43].

On the other hand, the interfacial distance is generally below 3 Å in the chemical bonding type of contacts, and the band structure of the 2DSC is slightly or strongly hybridized according to the bonding strength. TB generally disappears at interface I due to the small interfacial distance and large orbital overlap. Gap states are formed in the 2DSC of region B (figures 2(e) and (f)). The gap states herein include not only the MIGS but also the states from the 2DSC originating from

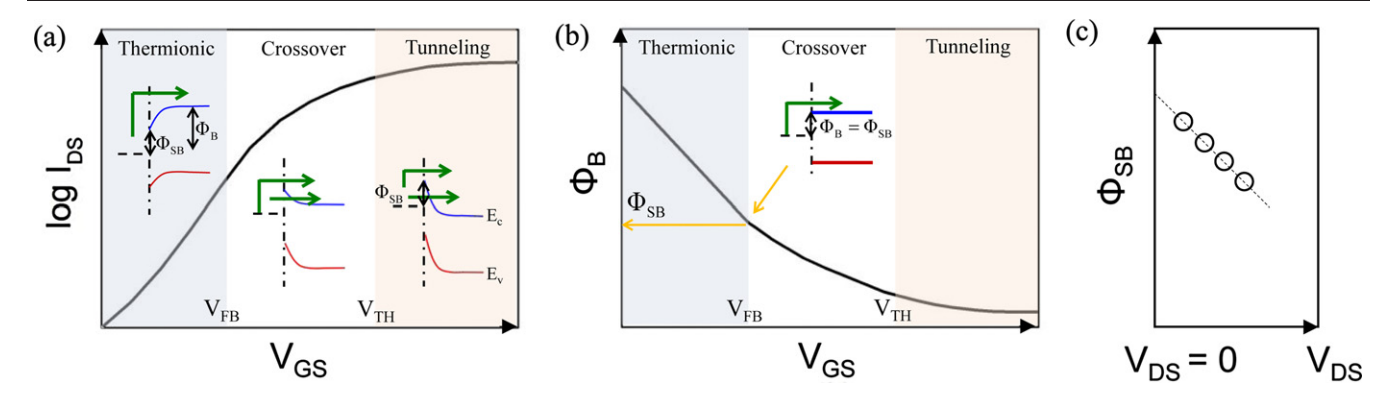


Figure 3. (a) Transfer characteristic of a typical SB FET. (b) The activation energy (Φ_B) as a function of gate voltage V_{GS} . V_{FB} is the flat band voltage, and V_{TH} is the threshold voltage. At $V_{GS} = V_{FB}$, the effective barrier height gives the SBH Φ_{SB} . (c) SBH lowering at finite bias V_{DS} induced by image charges. The SBH at zero bias can be derived through extrapolating the Φ_{SB} at finite V_{DS} to zero bias (dashed line). (c) Reprinted by permission from Springer Nature Customer Service Centre GmbH: Nature Materials [8] © 2015.

hybridization with the metal states. The charge can flow from the metal into the gap states. The model is close to the vdW type if the density of gap states is quite low (figure 2(e)). For the strong chemical bonding type, the covalent bonds disturb strongly the band structure of the 2DSC so that the bandgap of the 2DSC entirely vanishes in region B and carrier injection is barrier-free in the vertical direction (figure 2(f)). The ML 2DSC-metal junction in the source region can be treated as a new metal, which contacts with the 2DSC of region C in an edge geometry and may even generate gap states at interface II. The SB is formed in the lateral direction at interface II in the ML 2DSC FETs with this type of electrode contact.

In FETs based on multilayer 2DSCs with top electrodes, carrier injection goes through multiple interfaces: the interface between the metal electrodes and top layer 2DSC (interface I) and the vdW type of interfaces between adjacent 2DSC layers. As the thickness of 2DSC increases, interlayer resistance should be considered and carriers flow in the top few layers of the 2DSC [44]. SBs at the different interfaces can be derived separately according to equations (5)–(7). An example of few-layer BP FETs is provided in section 3.1.1 to illustrate the implementation.

The studies about edge contact are much fewer compared with the top contact. Despite the limited studies, edge contact is reported to be advantageous compared with top contacts for ML and especially multilayer 2DSCs [8, 45, 46]. The main reason lies in the shorter bonding distance with large orbital overlaps, the reduction or even disappearance of TB [13], weakened FLP, and gate-tunable SBH [47-51]. The large orbital overlap in the edge contact leads to a high density of states in the original band gap and minimum valence electron densities at the interface, implying a decrease in the contact resistance when altering the contact configuration from top contact to edge contact [13]. In the study of Banerjee et al [13], SB is absent (In other words, FLP is absent) and TB is low or absent for the ML MoS_2 and WSe_2 -metal edge contacts (metal = In, Ti, Au, and Pd). In the study of Liu et al [47], TB is absent, and SB remains in the 1T'-2H edge contact of ML MX₂. However, the SBH is tunable by a gate voltage due to a masked FLP. Experimentally, a low contact resistance has been found in the 1T'-2H edge contact of ML MX₂ (accompanied by a low SBH) [52] and the Au-MoS₂ [14], Ti-MoS₂ [16], and In-WSe₂ [15] combined-contact (top contact and edge contact). More explanations about the origin of the lower contact resistance in the 1T'-2H edge contact of ML MX₂ can be found in section 4.1.7.

For multilayer 2DSCs, the edge contact performs better than the top contact also because the in-plane conductivity of the multilayer 2DSCs is much larger than that in the out-of-plane direction. Another good merit of edge contact is its immunity to contact scaling [53], while the top contact electrode performs better for large contact area [13]. Hence, the edge contact is surely a good contact strategy to design the high-performance 2DSC transistors when the fabrication process is more accessible.

As mentioned above, most electrodes in use today are in pure top contact geometry or in geometry involving both top and edge contact geometries. Moreover, owing to the sizeable surface-area-to-edge-area ratio in the combo contact geometries, the top surface has a major contribution to conduction. Therefore, we mainly focus on the SBH in 2DSC FETs with top contact geometry in this review. The SBH in FETs with edge contact geometry is also summarized in section 4.1.7 based on the channel material of transition metal dichalcogenides (TMDs).

2.3. Experimental and theoretical methods to determine the SBH in 2DSC FETs

Due to an SBH, the transfer characteristic of an SB FET shows three transport regimes, as illustrated in figure 3(a), that is, thermionic emission, tunneling emission (or field emission), and a crossover regime that the both thermionic and tunneling injections coincide [8]. For gate voltage, $V_{\rm GS} < V_{\rm FB}$ (the flat band voltage), thermionic emission is the dominant mechanism. Charge carriers must overcome the activation energy $\Phi_{\rm B}$ to access the channel. The thermionic current over $\Phi_{\rm B}$ is:

$$I_{\rm THER} = SA_{\rm 2D}^*T^{3/2}\,\exp\left(-\frac{\Phi_{\rm B}}{k_{\rm b}T}\right)\left(1-\exp\left(-\frac{qV_{\rm DS}}{k_{\rm b}T}\right)\right),\eqno(9)$$

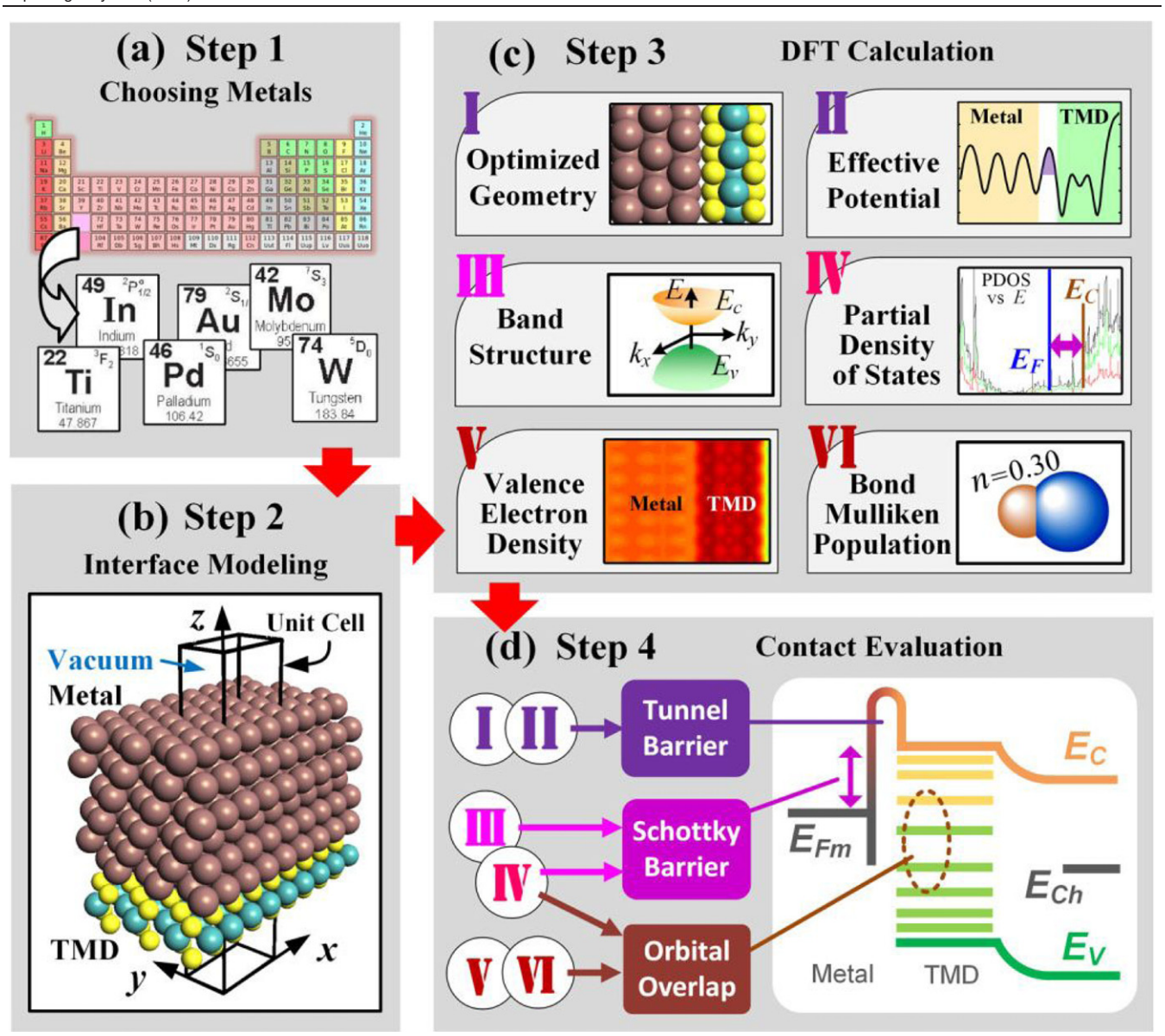


Figure 4. Flow chart of the framework for the SBH calculations using electronic BSC and WFA. (a) Step 1: choosing metals, (b) step 2: interface modeling, (c) step 3: density-functional theory (DFT) calculations, and (d) step 4: contact evaluation. Reproduced from [13]. CC BY 4.0.

where S is the contact area, $A_{\rm 2D}^*$ is the 2D equivalent Richardson's constant, T is temperature, q is the electronic charge, k_b is the Boltzmann's constant, and V_{DS} is the drain bias. $\Phi_{\rm B}$ depends linearly on $V_{\rm GS}$ in the thermionic region and becomes equal to Φ_{SB} when $V_{GS} = V_{FB}$, as shown in figure 3(b) with a relation of $\Phi_{\rm B} = q\Phi_{\rm SB} - (1 + C_{\rm it}/C_{\rm ox})^{-1}(V_{\rm GS} - V_{\rm FB}),$ where C_{it} and C_{ox} are the 2DSC interface trap capacitance and gate oxide capacitance, respectively. Tunneling emission occurs as $V_{\rm GS} > V_{\rm FB}$ and dominates the transport as $V_{\rm GS}$ beyond the threshold voltage, $V_{\rm TH}$. $V_{\rm TH}$ is defined as $V_{\rm GS}$ beyond which the band movement in the SC channel ceases. And correspondingly, the $\Phi_{\rm B}$ is non-linearly dependent on $V_{\rm GS}$ as $V_{\rm FB} < V_{\rm GS} < V_{\rm TH}$ and is nearly constant as $V_{\rm GS} > V_{\rm TH}$. Therefore, one method to obtain the SBH is to determine the gate voltage where $\Phi_{\rm B}$ stops depending linearly on $V_{\rm GS}$. The SBH can be measured experimentally by Arrhenius plot, i.e., $\ln(I_{\rm THER}/T^{3/2})$ against 1000/T. $\Phi_{\rm B}$ can be derived from the slope $\frac{\dim(I_{\rm THER}/T^{3/2})}{\det(1000/T)}$ at a fixed $V_{\rm DS}$. $\Phi_{\rm B}$ is plotted as a function of $V_{\rm GS}$, and the SBH $\Phi_{\rm SB}$ is equal to the $\Phi_{\rm B}$ at the crossing point of the linear and non-linear regions (figure 3(b)).

The thermionic current after considering SBH lowing to first order is:

$$I_{\rm THER} = SA_{\rm 2D}^* T^{3/2} \, \exp\left(-\frac{1}{k_{\rm b}T} \left(\Phi_{\rm SB} - \frac{qV_{\rm DS}}{n}\right)\right), \quad (10)$$

where n is the ideal factor. According equation (10), the slope of the Arrhenius plot $\frac{\text{dln}(I_{\text{THER}}/T^{3/2})}{\text{d}(1000/T)} = -\frac{q}{1000k}(\Phi_{\text{SB}} - \frac{V_{\text{DS}}}{n})$ can be plotted as a function of V_{DS} . The SBH Φ_{SB} at zero bias can be extracted from the y-intercept, as shown in figure 3(c).

Now we pay attention to the theoretical methods for the SBH prediction in FETs with top contact electrodes. The

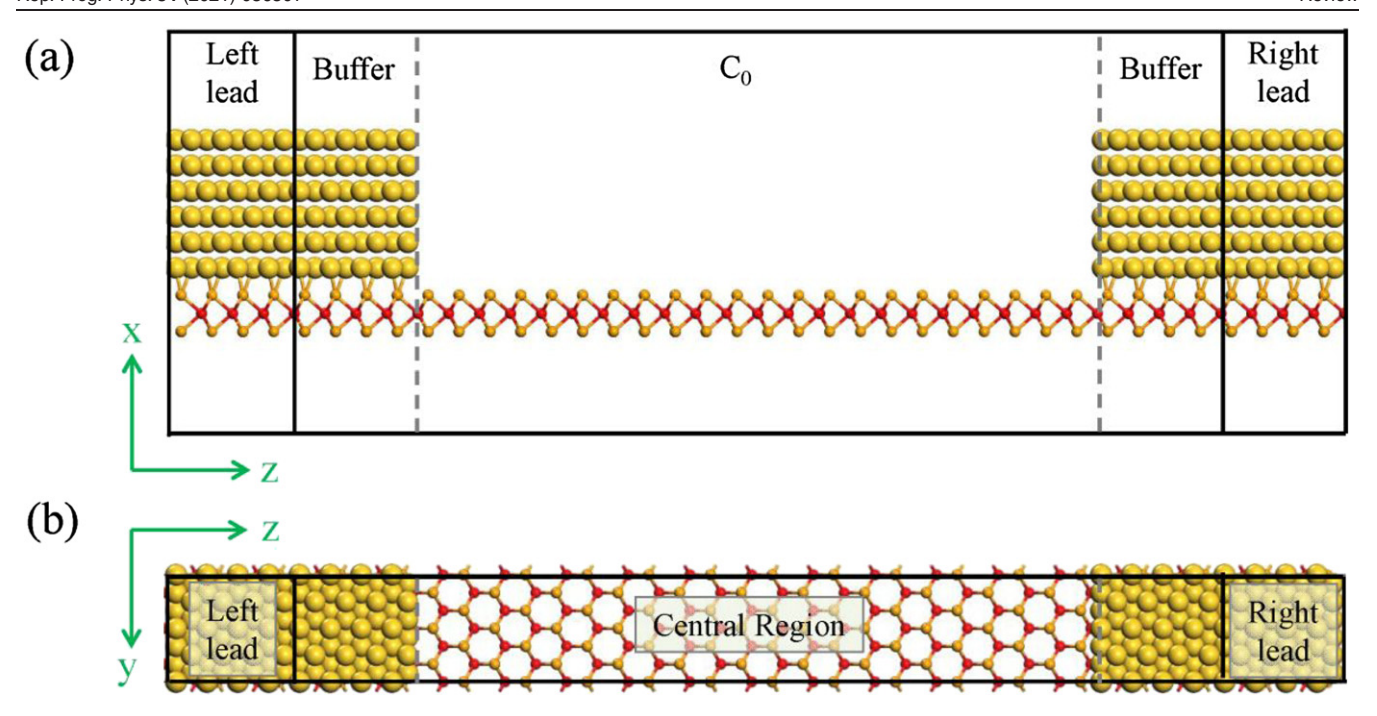


Figure 5. (a) Side and (b) top views of a 2DSC transistor model with semi-infinite left and right leads along the z-axis and central region consisting of central region (C_0) and buffer regions, under periodic, Neumann- and Dirichlet-type boundary conditions along the y, x, and z directions, respectively.

popular theoretical method to evaluate the SBH in 2DSC FETs is through the electronic band structure calculations (BSC) and work function approximation (WFA) [13]. Effective potential, band structure, the partial density of states (PDOS), valence electron population, and bond Mulliken populations of the contact are also calculated, from which the information of the TB and orbital overlap can be evaluated together. The whole flow path has been summarized in the review article [13] about the interfacial properties of 2DSC-metal contacts, as presented in figure 4. The vertical SBH was obtained from the band structure or PDOS as the energy difference between E_f of the contact and the CBM or the VBM of the contacted 2DSC. The band structure of the contacted 2DSC is distinguishable for the vdW and weak chemical bonding types. Therefore, the vertical SBH in FETs with these two types of electrode contact was derived through the BSC method. Some studies assume that the band edges are flat near the interface II for the vdW and weak chemical types of contacts, and the lateral SBH is regarded as equal to the vertical SBH derived from the BSC. For the strong chemical bonding type, the band structure of the contacted 2DSC is strongly destroyed. The lateral SBH was estimated using the WFA, defined as the difference of $E_{\rm f}$ of the contact and the CBM or VBM of the pristine 2DSC channel.

It worth noting that the interaction between the source/drain and the 2DSC channel is neglected using the BSC/WFA method, and the FLP effect at the lateral interface is not considered at all. However, such a drawback can be fully overcome through the *ab initio* QTS of a 2DSC FET. In the QTS method, the transistors with different electrodes are simulated as a whole by using a two-probe model and the DFT or Hartree–Fork (HF) theory coupled with the nonequilibrium Green's function (NEGF). The couplings at both interfaces I

and II are considered, and thus FLP effects at both the vertical and lateral interfaces are included.

The two-probe model used in the QTS method consists of the fully relaxed left and right leads and the central region, as shown in figure 5 (top contact geometry is adopted here for illustration). The central region includes the cell denoted as C_0 and left and right buffers. The length of 2DSC channels (C_0) is generally no less than 5 nm in the transmission direction (z-direction here). The left and right leads are semiinfinite. The electronic structure of the leads is calculated self-consistently using DFT or HF method beforehand. Then NEGF calculation of the device is performed incorporating the self-energy matrices of the leads with Dirichlet boundary condition between the central region and leads in the z-direction. Neumann and periodic boundary conditions are adopted in the x- and y-directions, respectively. It is necessary to evaluate the bulk modes for a considerable number of different energies (chemical potentials) and k points along the periodic y-axis for accuracy.

DFT at the generalized gradient approximation (GGA) level is often adopted during the QTS [25, 54, 55]. The first reason is that the 2DSC channel is doped by intrinsic defects, source/drain electrodes, and gates. The quasi-particle (QP) bandgap of the 2DSC shrinks as the doping density increases as a result of synergistic mechanisms of carrier-occupation self-energy $\Sigma_1 = i\delta GW_{\rm int}$, carrier screening $\Sigma_2 = iG_{\rm int}\delta W$, and double-difference term $\Sigma_3 = i\delta G_{\rm int}\delta W$ [56]. In this case, the single electron theory of DFT-GGA is a good approximation to predict the transport gap, although it generally underestimates the intrinsic bandgap of 2DSCs. For examples, the band gap of intrinsic ML phosphorene is 0.91 eV at the GGA of Perdew–Burke–Ernzerhof (PBE) level [55], which is 90%

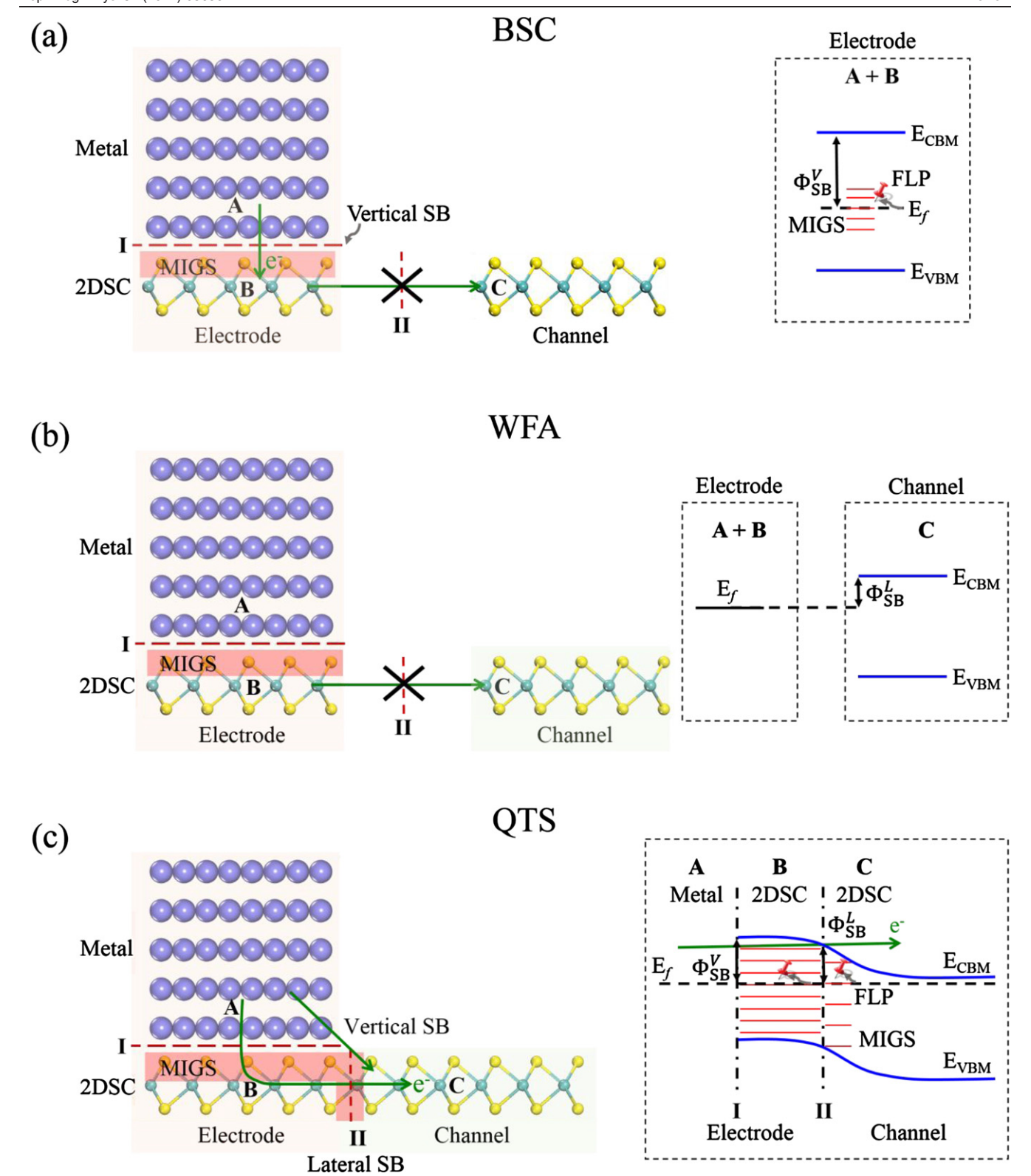


Figure 6. Schematics and corresponding band diagrams of the (a) BSC, (b) WFA, and (c) QTS methods used for a 2DSC-metal contact of weak chemical bonding type in a FET configuration. The BSC method is used to determine the vertical SBH, and the coupling between the metal electrode and underlying 2DSC at interface I is considered. There are MIGS and FLP at interface I. The WFA is used to determine the lateral SBH of a FET, and the coupling between the electrode compound (metal + underlying 2DSC) and the 2DSC channel and the FLP at interface II are ignored. The QTS can determine accurately both the vertical and lateral SBH because the MIGS and thus the FLP effect at both interfaces I and II are considered.

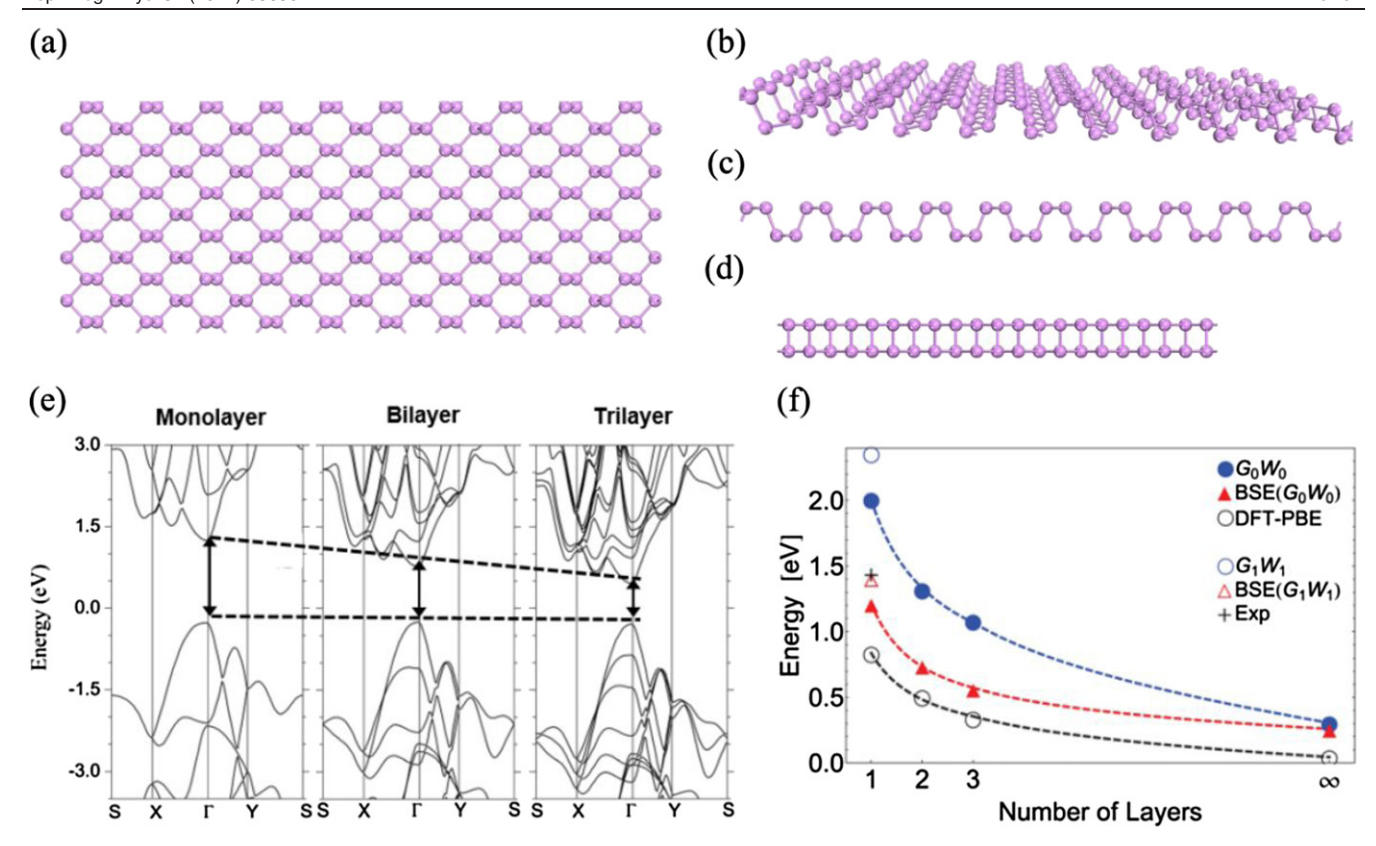


Figure 7. (a)—(d) Schematic structure of ML BP: (a) top view, (b) schematic view, (c) and (d) side views. (e) Bandstructure for ML, BL, and TL BP. Reprinted by permission from Springer Nature Customer Service Centre GmbH: Science Reports [61] © 2014. (f) Bandgap changes with the number of BP layers. Reprinted figure with permission from [59] Copyright (2014) by the American Physical Society.

of the experimental value (1.0 eV) [57], while the QP GW bandgap and hybrid functional Heyd–Scuseria–Ernzerhof (HSE) bandgap of the pristine ML phosphorene are 2.0–2.2 [58, 59] and 1.5 eV [60, 61], respectively. The ML MoSe₂ doped by a graphene substrate has a bandgap of 1.58 eV according to the angle-resolved photoelectron spectroscopy (ARPES) measurement [61]. The GGA-PBE method produces a bandgap of 1.52 eV, which is in excellent agreement with the experimental value and the GW calculated value of 1.59 eV at the experimental doping level (5.3 \times 10¹³ cm⁻²) [56, 62]. Besides, GGA-PBE is much cheaper and faster than the GW method.

Local device density of states (LDDOS) can be calculated and projected on the channel material, which clearly depicts the states' distributions and band edges in the real space. The vertical/lateral electron (hole) SBHs are derived from the energy difference between $E_{\rm f}$ of the transistor system and the CBM (VBM) of the channel 2DSC at the interface I/II, as illustrated in figures 2(d)-(f). The upper and lower bounds of colormap of the LDDOS plots are chosen to reproduce the measured transport bandgap of the 2DSC channel. If no experimental transport bandgap is available, one can choose to reproduce the transport gap by calculating the QP bandgap of the degenerately doped 2DSC based on the GW method [56, 62]. If neither bandgap is available, one can choose the LDDOS bounds to reproduce the GGA-PBE bandgap of the intrinsic 2DSC or preferably a 10% larger band gap. After marking the upper and lower bounds of LDDOS correctly, the lateral SBH is acquired at the electrode–2DSC interface. Meanwhile, the vertical SBH can be read from the LDDOS of the 2DSC under the metal electrode (region B).

In figure 6, we illustrate the mechanism difference between the BSC, WFA, and QTS methods using a weak chemical bonding type of contact. The BSC method is generally used to determine the vertical SBH and estimate the lateral SBH. In the BSC method, the coupling between the metal electrode and underlying 2DSC at interface I is considered (figure 6(a)). Correspondingly, the MIGS and FLP at interface I are considered, and the calculated vertical SBH is accurate. However, the coupling between the electrode compound (metal + underlying 2DSC) and the 2DSC channel at interface II is ignored, and its estimation to the lateral SBH is thus less reliable and is actually totally invalidated when underlying 2DSC is metallized. The WFA is often used to determine the lateral SBH of a FET when a metallization of underlying 2DSC occurs, but the coupling between the electrode compound and the 2DSC channel and the FLP at interface II are also ignored (figure 6(b)), resulting in an inaccuracy too. The QTS can accurately determine both the vertical and lateral SBHs because the MIGS and thus the FLP effect at both interfaces I and II are considered (figure 6(c)). The discrepancy between the SBHs obtained from the QTS and BSC/WFA is generally observed. For example, the pinning factor of the ML MoS₂ is 0.187 and 0.27-0.32, respectively, from the QTS and BSC/WFA methods [63–66]. The value of 0.187 is well consistent with the experimentally reported S of 0.09–0.11 [31], suggesting

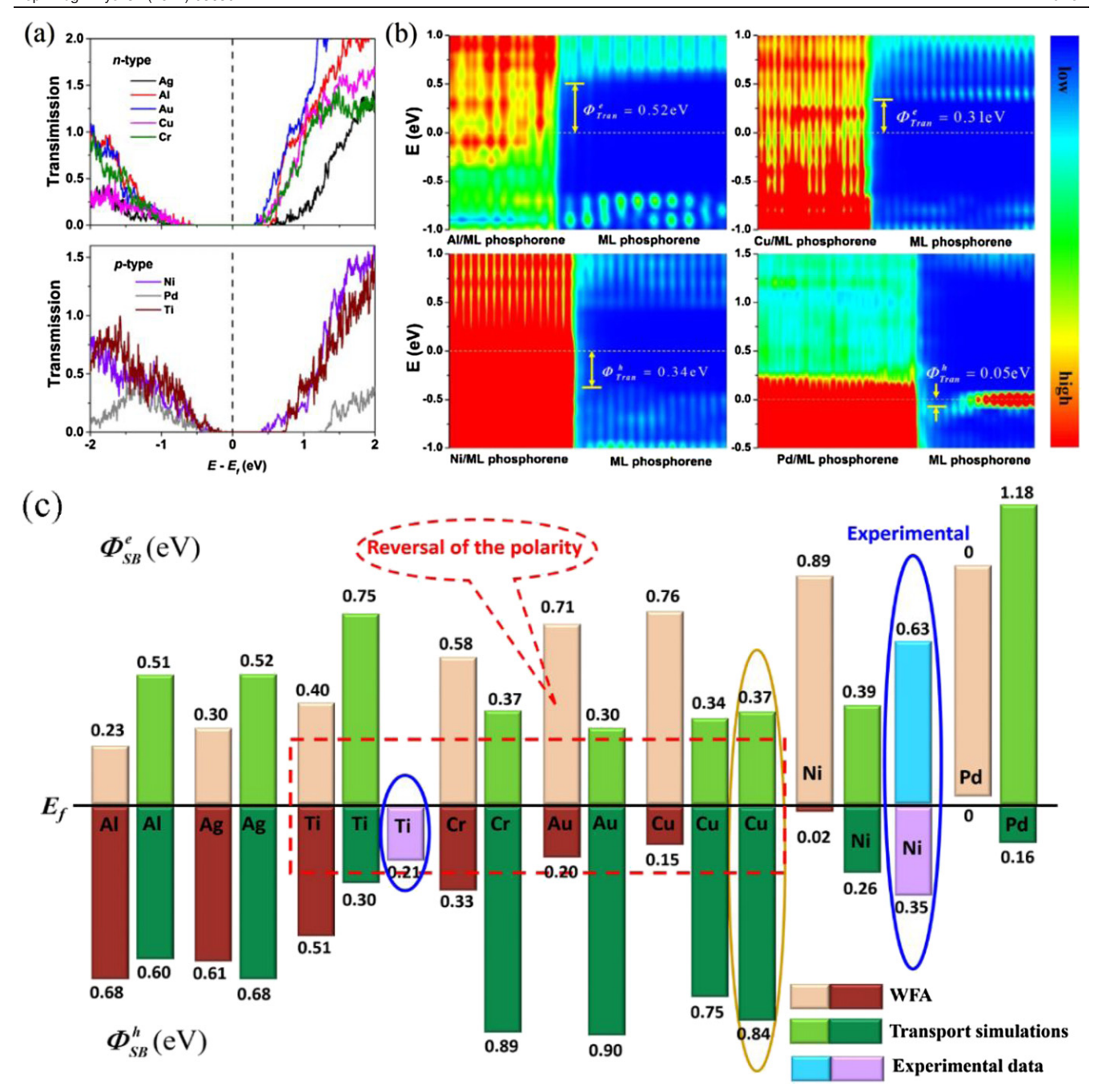


Figure 8. (a) Transmission spectra of the channel and (b) LDDOS in color coding in the ML BP FET under zero bias with Ag, Cu, Cr, Al, Au, Ni, Ti, and Pd as electrodes and the channel length of L = 5 nm. (c) Lateral SBHs of the ML BP-metal contacts from the WFA, quantum transport calculations, and experimental results. The values in the yellow and blue circles are extracted from references [18, 58, 73]. Reprinted with permission from [74]. Copyright (2016) American Chemical Society.

that the coupling between the source/drain and the channel is essential during the SBH assessment. Moreover, the scheme of the *ab initio* QTS can also be applied to the 2D FETs with edge contacts [47, 67].

3. Schottky barriers in the FETs based on elemental 2DSCs

3.1. Group V 2DSC

3.1.1. Black phosphorene-metal top contacts. BP, as the 2D structure of black phosphorus, has been firstly

mechanically cleaved from bulk black phosphorus in 2014 [68] and then has attracted broad interest among scientists [69, 70]. BP possesses the plucked honeycomb structure (figures 7(a)–(d)). Similar to other layered 2D materials, BP layers are stacked together through vdW interaction. Different from the isotropic graphene and semiconducting TMDs, BP possesses anisotropic optical, electronic, mechanical, and thermal properties [68, 71]. Especially, BP shows prominent semiconducting properties in electronic and photoelectronic applications. The bandgap of BP is direct and layer-dependent

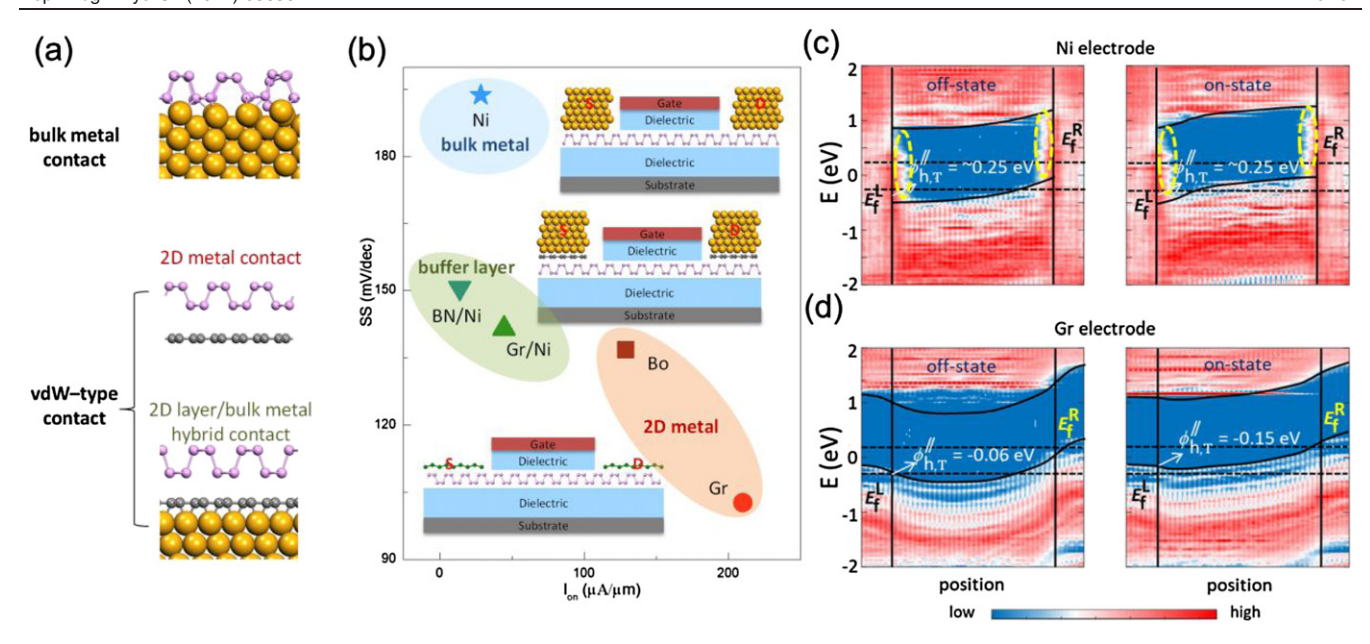


Figure 9. (a) ML BP transistors with bulk Ni, 2D metal, and 2D layer/Ni hybrid electrodes. (b) SS versus the on-state current in the ML BP FETs with different types of electrode configurations. (c), (d) LDDOS projected on the position of the ML BP transistors with Ni and graphene electrodes at off- and on-states. The applied bias is $V_b = 0.5$ V. The black dotted lines stand for the Fermi level of the left and right electrodes, denoted by E_f^L and E_f^R , respectively. The lateral hole SBH of the transistor with graphene electrode is reduced from -0.06 eV in the off state to -0.15 eV in the on state, but that of the transistor with bulk Ni electrode is intact. The MIGS (circled by the yellow dashed lines) in the transistor with bulk Ni electrode decrease the SB width. Reproduced from [82] with permission of The Royal Society of Chemistry.

from 0.3 eV for bulk BP to 1.0 eV for ML counterpart (figure 7) [58, 72]. The BP FETs have been fabricated with a high hole mobility (up to 1000 cm V^{-1} s⁻¹) and also a high on/off ratio (10⁵) [58, 68, 73]. These properties indicate that BP is capable of using as the channel materials in nanoelectronic devices.

3.1.1.1 Interfacial properties of ML BP-metals in theory Pan et al investigated the interactions between ML BP and a variety of metal electrodes Au, Cu, Cr, Al, Ag, Ti, Ni, and Pd by using the BSC and QTS methods [74]. A band hybridization is appeared at the interface between the metal electrode and ML BP, leading to the metallization of ML BP and an Ohmic contact in the vertical direction. When Au, Cu, Cr, Al, and Ag are chosen as electrodes, n-type lateral Schottky contacts are formed with the electron SBHs of 0.30, 0.34, 0.37, 0.51, and 0.52 eV, respectively, through the QTS method. When Ti, Ni, and Pd are chosen as electrodes, p-type lateral Schottky contacts are formed with the lateral hole SBHs of 0.30, 0.26, and 0.16 eV, respectively (figure 8).

Gong *et al* reported the electrical contacts between ML BP and Cu(111), Zn(0001), In(110), TaP(110), and NbP(110) by using first-principles BSC and QTS [18]. They predict that most of the metals form Schottky contact with ML BP in the vertical direction except Cu, which form Ohmic contact. According to the LDDOS from the QTS, Cu and Zn electrodes form n-type Schottky contacts in the lateral direction with the electron SBHs of about 0.4 and 0.2 eV, respectively. The interfacial properties of ML BP–MXene ($Zr_{n+1}CnT_2$, T=0, F, OH, n=1,2) also explored by Yuan *et al* in the BSC method [75]. An Ohmic contact is formed at the vertical interfaces for

ML BP–MXenes. Lee *et al* calculated the electron SBH of ML BP–Al contacts of 0.36 eV with n-type polarity, and no SB exists at the ML BP/Ti and Sc interface in the vertical direction [76].

To improve the electrical contacts to BP, novel electrodes with vdW-type electrical contact (such as 2D metals electrodes and bulk metal/2D layer hybrid electrodes) might be a promising choice [37, 76–79]. By utilizing graphene as the source and drain, the fabricated black phosphorus FETs show linear output characteristics [80]. By inserting a TiO₂ buffer layer between BP and cobalt, the SB is reduced, and high drain current modulation and hole mobility are observed in the BP transistor [81].

By *ab initio* QTS, a comparative study of a series of vdW-type contacts and bulk metal Ni(111) contact demonstrate the potential of 2D electrodes for the improvement of the BP transistor performance (figure 9) [82]. Especially, the 2D graphene electrodes show an overall enhancement in both the on-state current and the gate electrostatics (reduced subthreshold swing (SS)). This phenomenon originates from two facts. First, the interfacial interactions between graphene and ML BP are weak, and few MIGS exist at the electrode–channel interface. As a result, the SBH is tunable by changing the gate voltage [80, 82]. By contrast, the SBH is difficult to be tuned by the gate voltage with the bulk Ni electrode (figure 9). Second, the electrode's low dimensionality makes the screening to the electric field weak, leading to strong gate controllability [82].

3.1.1.2. Interfacial properties of the bilayer and trilayer BP-metals in theory The interaction between BL and TL BP

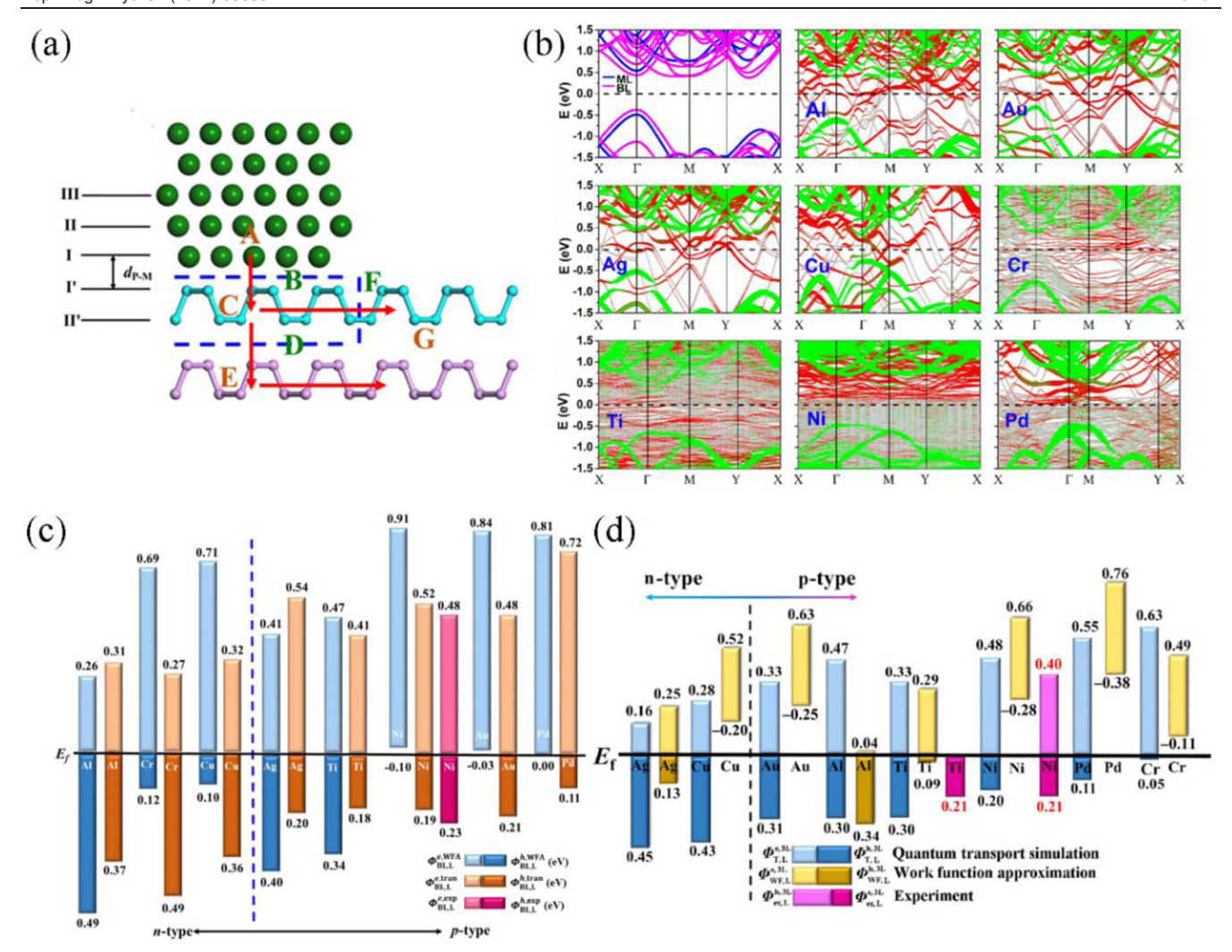


Figure 10. (a) Schematic of a typical metal—BL BP contact system from the cross-sectional view. (b) Band structure of pure ML (blue line) and BL (magenta line) BP, and that of BL BP—metal interface systems. Gray lines: band structures for the interfacial systems; red (green) lines: band structures of the layer of BP close to (far away from) the metal surface. BL (c) and TL (d) BP lateral SBHs obtained from the QTS and the WFA. For comparison, the SBHs of BP obtained from experiments with Ni (for BL and TL BP) and Ti (for few layers of BP thicker than 2 nm) as electrodes are also provided. (a)—(c) Reprinted with permission from [83]. Copyright (2017) American Chemical Society. (d) Reprinted by permission from Springer Nature Customer Service Centre GmbH: Nano Research [84] © 2017.

and metal is systematically explored by Pan et al [83] and Zhang et al, respectively [84]. In an FL BP EFT, SB can appear at a variety of interfaces (figure 10(a) using BL BP as an example). There are no SBs at the interface between the metal electrodes and the top layer of BP as the band structures of the top BP layer are destroyed for both BL and TL. SB appears at the interface between the top BP layer and the bottom BP layer (for BL BP FETs) or the bottom two layers (for TL BP FETs) in the vertical direction as the bandgap is maintained after contact with the metal electrodes (blue lines in figure 10(b)). In the BL BP FET, n-type Schottky contact is formed at the interface D with Cr, Al, Ag, and Ti electrodes while p-type Schottky contact is formed with Cu, Au, Ni, and Pd electrodes (figure 10(b)). In the TL BP FET, n-type Schottky contact is formed with Cr and Al electrodes, and p-type Schottky contact is formed with Ag, Ti, Au, Ni, and Pd. Especially, vertical Ohmic contact is formed with TL BP when Cu is

used as an electrode. Lee *et al* [76] showed that Ti and Al electrodes form n-type Schottky contacts with BL (TL) BP with the electron SBHs of 0.4 (0.54), 0.47 (0.52) eV, respectively, and Sc also forms n-type Schottky contact with TL BP but p-type with BL BP, and the SBHs for the hole and electron are 0.59 and 0.5 eV, respectively, in the vertical direction.

The lateral SB exists at the interface between the BL (TL) BP under the electrodes and the channel. An n-type lateral Schottky contact is shaped between BL BP and the Cr, Al, and Cu electrodes, and the resulting electron SBH is 0.27, 0.31, and 0.32 eV, respectively, whereas a p-type lateral Schottky contact is shaped between BL BP and the Pd, Ti, Ni, Ag, and Au electrodes, and the resulting hole SBH is 0.11, 0.18, 0.19, 0.20, and 0.21 eV, respectively (figure 10(c)) [83]. On the other hand, an n-type lateral Schottky contact is shaped between TL BP and the Ag and Cu electrodes, and the corresponding electron SBH is 0.16 and 0.28 eV, respectively, while a p-type lateral Schottky contact is shaped between TL BP and the Al, Au, Pd, Ni,

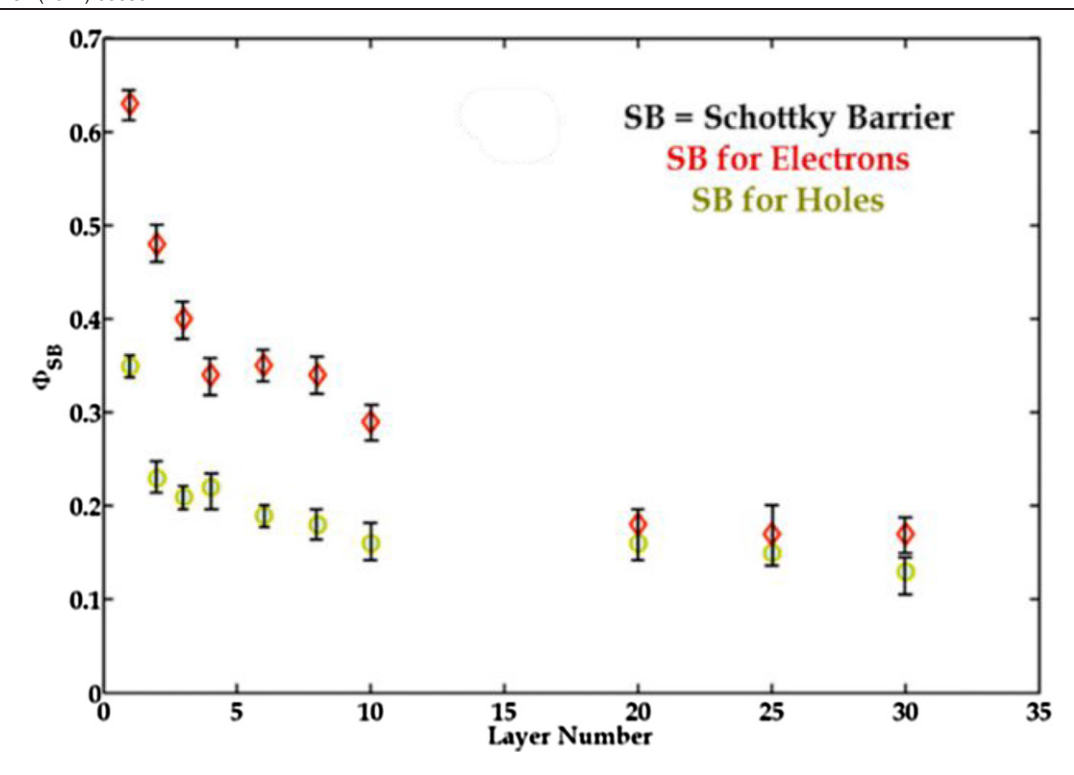


Figure 11. SBH of BP for both electrons and hole with Ni as electrodes as a function of the layer number obtained in experiments. Reprinted with permission from [58]. Copyright (2014) American Chemical Society.

Ti, and Cr electrodes, and the corresponding hole SBH is 0.30, 0.31, 0.11, 0.20, 0.30, and 0.05 eV, respectively (figure 10(d)) [84].

The SB types and heights are dependent on the layer numbers of the channel SCs. For example, Al and Cr form n-type Schottky contact with ML and BL BPs in the lateral direction but form p-type Schottky contact with TL BP in terms of the QTS results, and the SBHs are also changed a lot. Besides, the SBHs generally decrease as the number of layers of BP increases in the lateral direction according to the QTS results because of the decrease of the BP band gap. Interestingly, according to the results obtained on the BL and TL BP FETs, it is suggested that the lateral SBH in an N-layer 2D semiconducting material FET with a strongly interacting electrode can be inferred from a BSC of its (N + 1)-layer counterpart [83, 84].

3.1.1.3. Experimental results In the experiment, Zhang et al tested the few-layer BP FET with Cr/Au as the electrode, and the FET displays clear p-type Schottky behavior [68]. Saptarshi et al used Ni as electrodes and found that the Ni electrode forms p-type Schottky contact with the ML, BL, and TL BP channels [58]. The electrons SBH for ML, BL, and TL BP EFT are 0.64, 0.48, 0.40 eV respectively, and the hole SBH are 0.35, 0.23, 0.21 eV respectively. They also find that the SBHs for both electrons and holes decrease as the number of BP layer increases (figure 11) when using Ni as the electrode because the bandgap decreases. Saptarshi et al also used Ti and Pd as electrodes and found that few layers of BP form p-type Schottky contact with both Ni and Pd electrode [69]. Du et al used Ni and Pd as the electrode in a few layers BP FET

and found that when Ni is used as an electrode, the BP transistors can be switched from the p-type behavior into pronounced n-type once the channel length is scaled down to deep submicron [85]. Miao *et al* found that single Au as an electrode also forms n-type Schottky contact with BP [86]. Liu *et al* used Ti/Au as the electrode and found that BP shows well-behaved p-type Schottky transistor characteristics [73]. Besides, they measured the SBH for holes to be 0.21 eV at the Ti/BP junction. David *et al* reported unipolar n-type BP transistors with the channel thickness of 3–13 nm when using Al as electrode [87]

The lateral SB type and heights of BP from the experiments and QTS are summarized in table 1 and also compared in figures 8(c) and 10(c) and (d). The SBHs obtained from the QTS are in accordance with the experiments, while those from the WFA differ from the experiments greatly. For example, the calculated hole SBHs in the ML/BL/TL BP FET with Ni electrode obtained from the QTS are 0.26/0.19/0.20 eV, respectively, which are in agreement with the experimental values of 0.35/0.23/0.21 eV [58]. By contrast, the corresponding hole SBHs are only 0.02/-0.10/-0.28 eV in the WFA, implying an artificial Ohmic or quasi-Ohmic contact between Ni and BP. The calculated hole SBH of 0.30/0.18/0.21 eV in ML/BL/TL BP FETs with Ti electrode agrees well with the experimental value of 0.21 eV with few-layer BP as the channel [73].

3.1.2. Blue phosphorene–metal top contacts. Blue phosphorene (BlueP), a hexagonal phase of phosphorene, has been fabricated on Au (111) substrate by molecular beam epitaxial growth method [90, 91]. BlueP has an indirect thickness-dependent bandgap of around 1.10 (bulk) \sim 1.98 (ML) eV at

Table 1. Comparison of the SB type and SBH of ML and few-layer BP in the lateral direction between the experiments and QTS for different metal electrodes.

Electrode	Experiments				QTS [74, 83, 84]	
	Reference	Thickness	Polarity	Φe/h (eV)	Polarity	Φe/h (eV)
					n-type (ML)	0.37/0.89 (ML)
					n-type (BL)	0.27/0.49 (BL)
Cr	[88]	Few-layer	p-type		p-type (TL)	0.63/0.03 (TL)
				0.63/0.35 (ML)	p-type (ML)	0.39/0.26 (ML)
				0.47/0.23 (BL)	p-type (BL)	0.52/0.19 (BL)
Ni	[58, 85]	ML to 30 layers	p-type	0.40/0.21 (TL)	p-type (TL)	0.48/0.20 (TL)
					p-type (ML)	0.75/0.30 (ML)
					p-type (BL)	0.41/0.18 (BL)
Ti	[69, 73]	Few-layer	p-type	0.21 for holes	p-type (TL)	0.33/0.30 (TL)
					p-type (ML)	1.18/0.16 (ML)
					p-type (BL)	0.72/0.11 (BL)
Pd	[69, 85]	Few-layer	p-type		p-type (TL)	0.55/0.11 (TL)
					n-type (ML)	0.30/0.90 (ML)
					p-type (BL)	0.48/0.21 (BL)
Au	[88, 89]	Few-layer	p-type		p-type (TL)	0.33/0.31 (TL)
					n-type (ML)	0.51/0.60 (ML)
					n-type (BL)	0.31/0.37 (BL)
Al	[87]	3–13 nm	n-type		p-type (TL)	0.47/0.30 (TL)

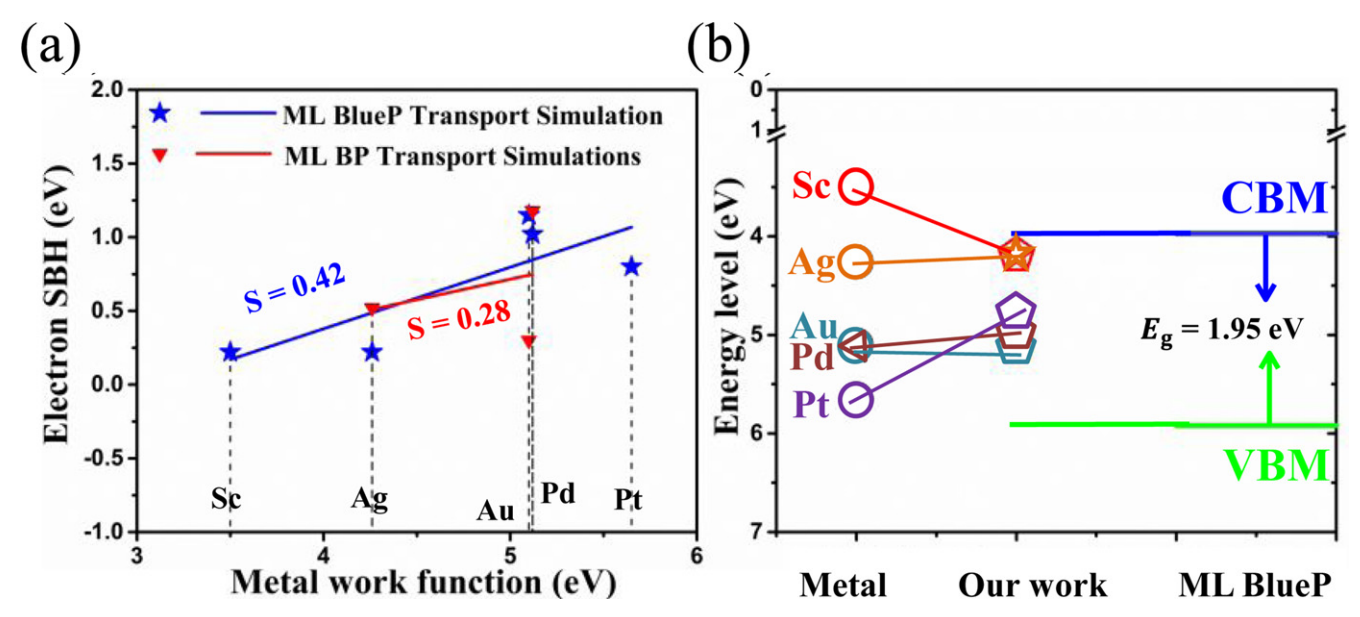


Figure 12. (a) Lateral electron SBHs for the ML BlueP and ML BP transistors against the metal work function. (b) Illustration of FLP in the ML BlueP transistor, Reproduced with permission from [94], © Tsinghua University Press.

the DFT-GGA level [92, 93]. Li *et al* theoretically studied the interfacial properties of ML BlueP transistors with Sc, Ag, Pt, Pd, and Au electrodes by using *ab initio* BSC and QTS methods [94]. ML BlueP on the Sc, Ag, Au, Pd, and Pt surfaces is metalized, resulting in no SB in the vertical direction. In the lateral direction, an n-type Schottky contact takes shapes between ML BlueP forms and Sc, Ag and Pt electrodes, featured by electron SBHs of 0.22, 0.22, and 0.80 eV, respectively, and p-type Schottky contact takes shape between ML BlueP and Au and Pd electrodes, featured by hole SBHs of 0.61 and 0.79 eV, respectively (figure 12(a)). ML BlueP contacted with the common metal electrodes exhibit a pinning

factor of 0.42 and prefers n-type lateral Schottky contact, as shown in figures 12(a) and (b) [94]. This character is different from ML BP, which favors a p-type lateral Schottky contact with the common metal electrodes with a smaller pining factor of 0.28 and thus a stronger FLP [74]. Such a polarity difference is ascribed to a larger work function of ML BlueP (5.92 eV) than that of BP (5.04 eV).

2D electrodes were also applied to reduce the SBH in the BlueP transistors. The DFT calculation confirms a tunable vertical SBH between BlueP and graphene by an external electric field [95]. Such similar electric field tunability of the SBH is also observed in the ML BlueP/1T–MoSe₂ contact [96].

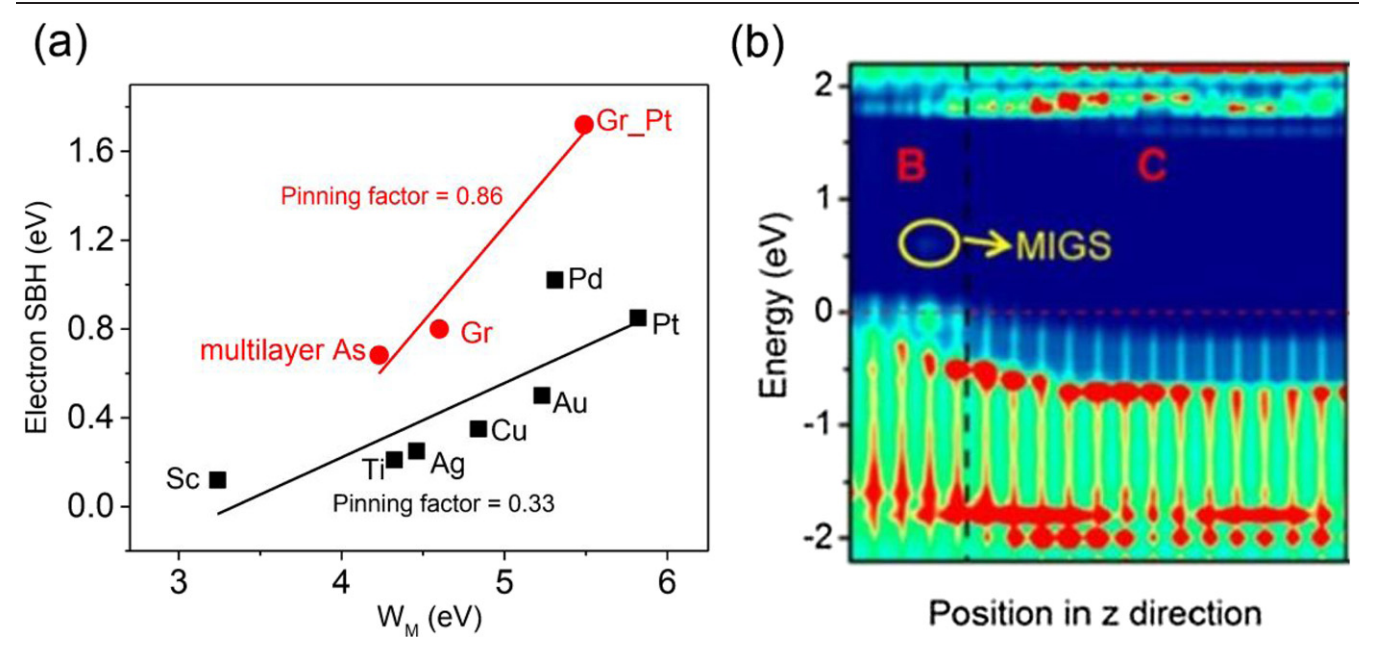


Figure 13. (a) Electron SBHs of the ML arsenene devices with different bulk metals, 2D graphene, multilayer arsenene, and graphene–Pt hybrid electrodes. (b) LDDOS in the ML arsenene device under zero bias with raphene–Pt hybrid electrodes. Adapted with permission from [25]. Copyright (2017) American Chemical Society.

The SBH can be tuned to zero by the external electric field to achieve Ohmic contact. Another possible way to tune the SBH of the BlueP/graphene contact is to apply a strain on the interface [97]. Under compressive strain, the Fermi level gradually shifts from CBM to VBM of BlueP, resulting in the SB type changed from n- to p-type. Other 2D metals with proper work function are also considered to be promising candidates of the contact electrodes, such as borophene and MXenes. ML BlueP forms a vertical weak p-type Schottky contact with the 2D metallic ML borophene electrode with a hole SBH of 0.76 eV [98]. The SBH of the ML BlueP/ML surfaceengineered MXenes (the functionalized groups -F and -OH absorbed on MXenes) contacts vanishes, achieving an Ohmic contact [99]. The 2D-bulk metal combination electrode was also tried in the BlueP FETs. For example, the electron SBH of the ML BlueP/Sc contact is 0.22 eV, while it is reduced to 0.02 eV upon graphene intercalation between ML BlueP and Sc [94].

3.1.3. Arsenene-metal top contacts. Layers of arsenic are stacked together by vdW interaction, and the arsenic atoms of ML arsenene are covalently bonded inside a single layer and form a stable orthorhombic or hexagonal structure, corresponding to the α - and β -phase, respectively [100, 101]. Experimentally, FL α -arsenene FETs, which are fabricated from mechanical exfoliation, show thickness-dependent electronic properties, with the highest carrier mobility of about 59 cm² V⁻¹ s⁻¹ [102]. There is a semimetal–semiconductor transition while thinning the bulk arsenic to FL arsenene [103, 104]. ML α - and β -arsenene have an indirect bandgap of 1.38 eV and 2.21 eV at the HSE06 level of theory, respectively [103]. Wang *et al* calculated the QP bandgap of ML β -arsenene to be 2.47 eV under GW approximation [55]. First-principal simulations show that α - (β -) arsenene possesses high carrier

mobility of the order of several thousand (decade) $cm^2 V^{-1} s^{-1}$ [55, 105]. All these properties make 2D arsenene promising for semiconducting device applications.

Wang *et al* systematically studied the interactions between ML β -arsenene and a variety of metal electrodes by using the *ab initio* BSC and QTS methods (figure 13) [25]. In the following, we denote ' β -arsenene' as 'arsenene' hereafter without a particular statement. After contact with the bulk metals, ML arsenene hybridizes with metal electrodes and forms an Ohmic contact in the vertical direction. However, lateral SBs exist between the metalized arsenene in the source and the channel with a pinning factor of 0.33 (figure 13(a)). When Sc, Ti, Ag, Cu, and Au are chosen as electrodes, n-type lateral Schottky contacts are formed with the SBHs of 0.12, 0.21, 0.25, 0.35, and 0.50 eV, respectively. While Pd and Pt are chosen as electrodes, p-type lateral Schottky contacts are formed with the SBHs of 0.75 and 0.78 eV, respectively.

2D vdW electrodes are tried in the design of high performance ML arsenene FETs to decrease the SB [25]. With graphene, graphene/bulk metal hybrids, and multilayer arsenene used as the electrodes, the FLP effect can be greatly reduced with a pining factor of 0.86 due to the suppression of MIGS (figure 13(a)). When graphene is used as electrodes, gap states are absent. The vertical/lateral hole and electron SBHs are both about 0.8 eV [25]. Owing to the disappeared gap states, $E_{\rm f}$ of graphene not be pinned at the interface, and the SBH is adjustable by gates [38, 39, 106, 107]. A p-type Ohmic contact is achieved when a hybrid electrode of high work function metal Pt and graphene is adopted as electrodes (figure 13(b)). There are only a few MIGS at interface I. The suppression of MIGS significantly alleviates FLP and results in an Ohmic contact. Metallic multilayer arsenene was also studied serving as electrodes of the ML arsenene FETs without

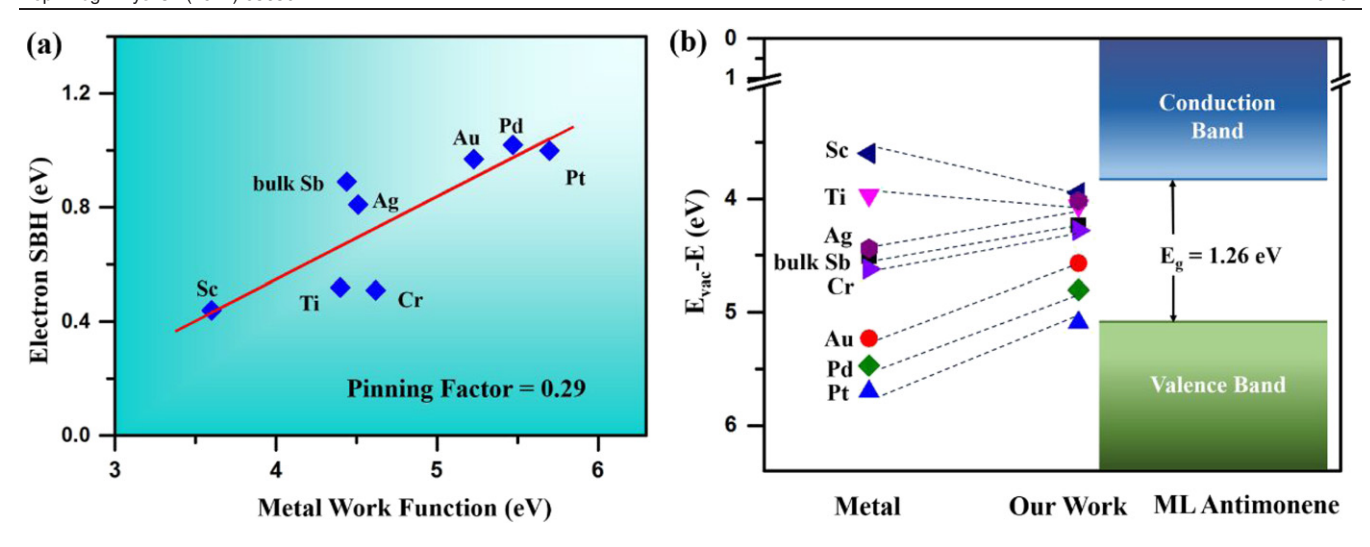


Figure 14. Electron SBHs in the ML antimonene transistors with various bulk metal electrodes. Reprinted figure with permission from [112], Copyright (2019) by the American Physical Society.

doping [35]. The electron SBH is 0.808 eV with BL arsenene electrode and is decreased to 0.682 eV with trilayer, four-layer, and six-layer arsenene electrodes from the DOS analysis. The SBH can be modulated by gates because of the absence of FLP. Therefore, albeit the large SBH, the ML arsenene FETs with trilayer arsenene electrodes can intrinsically offer larger oncurrent as well as better SS than the homostructure metal oxide semicondutor FETs (MOSFETs) with the 5×10^{13} cm² doped source and drain.

3.1.4. Antimonene-metal top contacts. Hexagonal antimonene, another group-VA 2D material, has also attracted the interest of many scientists. High-quality antimonene has been fabricated experimentally by mechanical exfoliation [108], liquid-phase exfoliation [109], and epitaxy growth [110, 111]. Antimonene is quite stable under ambient conditions even in water, while BP is severely damaged when uncovered to the air. According to *ab initio* QTS, the optimal sub-10 nm ML antimonene MOSFETs can meet the requirements of ITRS for both the lower-power and high-performance applications [55].

Zhang *et al* [112] theoretically studied the SBHs in the ML antimonene FETs. The band structures of the examined bulk metal contacts are all destroyed due to the strong coupling interaction between the monolayer antimonene and bulk metals. Hence, there is no SBH in the vertical direction. In the lateral direction, ML antimonene forms n-type Schottky contacts with Sc ($\Phi_L^e = 0.44 \text{ eV}$), Cr ($\Phi_L^e = 0.49 \text{ eV}$) and Ti ($\Phi_L^e = 0.52 \text{ eV}$) electrodes, respectively. Correspondingly, lateral p-type contacts are formed in the ML antimonene–Au ($\Phi_L^h = 0.56 \text{ eV}$), Ag ($\Phi_L^h = 0.4 \text{ eV}$), Pt ($\Phi_L^h = 0.31 \text{ eV}$), Pd ($\Phi_L^h = 0.29 \text{ eV}$) and bulk Sb ($\Phi_L^h = 0.44 \text{ eV}$) contacts as shown in figure 14. There are clear MIGS at the interfaces. The pinning factor is S = 0.29.

To decrease the SBH of ML antimonene transistors, Zhang *et al* also tried the BN/graphene–bulk metal hybrid and pure 2D metal electrodes, as shown in figure 15 [112]. The QTS [112] predicts p-type lateral Ohmic contact with the

graphene–Pt electrode and n-type lateral Ohmic contact with 2D metal $Hf_2N(OH)_2$, according to the LDDOS maps in figures 15(b) and (f). Whereas relatively large lateral electron SBHs of 0.46 and 0.56 eV, respectively, are formed in the ML antimonene-Sc contacts with a BN or graphene inserted layer (figures 15(c) and (d)). 2D metal graphene was also tried and formed a p-type SB with ML antimonene at zero bias with a hole lateral SBH of 0.12 eV (figure 15(e)).

It is noteworthy that there is an apparent band bending for the 2DSC under the 2D metal in the ML antimonene–BN–Sc, -graphene–Sc, and -graphene contacts (figures 15(c)–(e)). There are some MIGSs at interfaces II of the three contacts, as shown in the LDDOS maps. The band bending in the electrode region is ascribed to a charge transfer between the 2DSC under the 2D metal and the MIGS at interface II (or 2DSC in the channel). In the presence of a band bending the 2DSC in the electrode region, the vertical SBH is no longer a constant. At interface II, the vertical and lateral SBHs are equal. In the deep region of the electrode (far away from interface II), the vertical SBH should be equal to that obtained from the BSC performed on an isolated compound electrode. For the graphene-Sc electrode, the vertical SBH at the left edge of the selected electrode region has decreased to 0.21 eV figure 15(d), which already approaches the one of 0.17 eV obtained from the BSC.

3.1.5. Bismuthene–metal top contacts. Bismuthene is the last one of group-V-enes, having a honeycomb structure and is predicted to be a topology insulator [107, 113–115] having an indirect bandgap of about 0.67 eV. Recently, ML bismuthene has been grown on SiC substrate [116]. The ARPES found a band split at the K-point and named it the 'Rashba fingerprint' (figure 16(c)), which is in close agreement with the DFT calculation (as shown in figure 16(b)). Alternatively, bismuthene has some superior characteristics: (1) it is much more stable and resistant to oxidation at room temperature [117]. (2) It has a high carrier mobility of 10^2 (ML) to 10^6 cm² V⁻¹ s⁻¹ (bulk) [118]. (3) Bismuthane (functionalized bismuthene) is also predicted to be a topological insulator that has one of the largest bulk bandgaps [119–122].

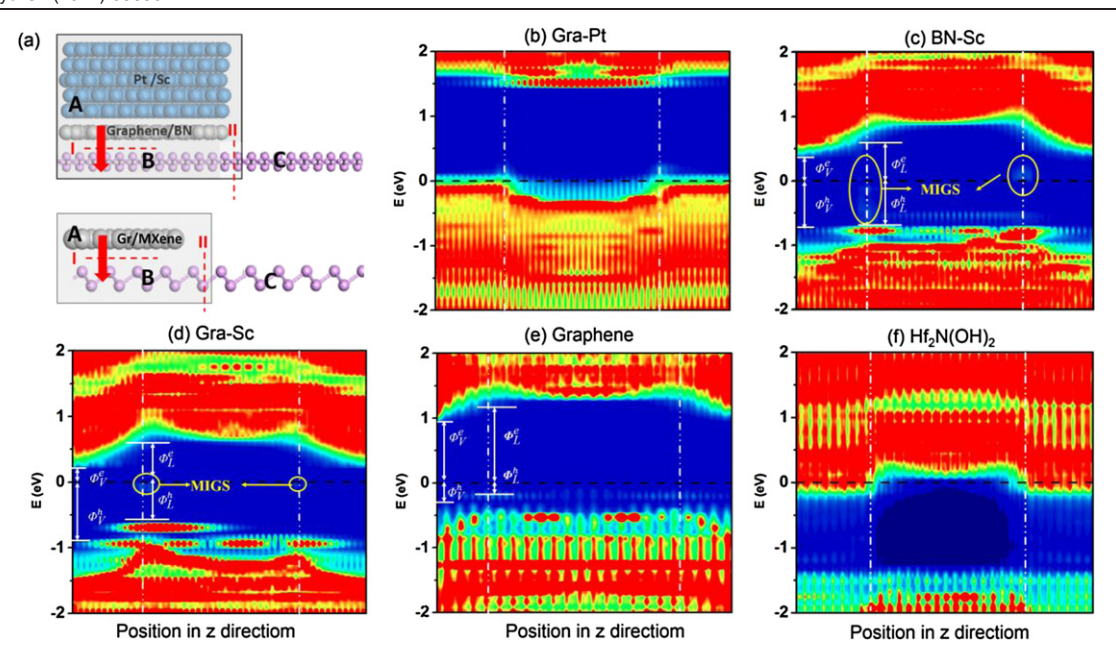


Figure 15. (a) Schematic diagrams of the ML antimonene transistors with vdW-type of electrodes. (b)–(f) LDDOS maps projected on the ML antimonene channel of the transistors at zero bias with the different hetero-contact electrodes and 2D metal electrodes. The yellow circle region shows the MIGS. Reprinted figure with permission from [112], Copyright (2019) by the American Physical Society.

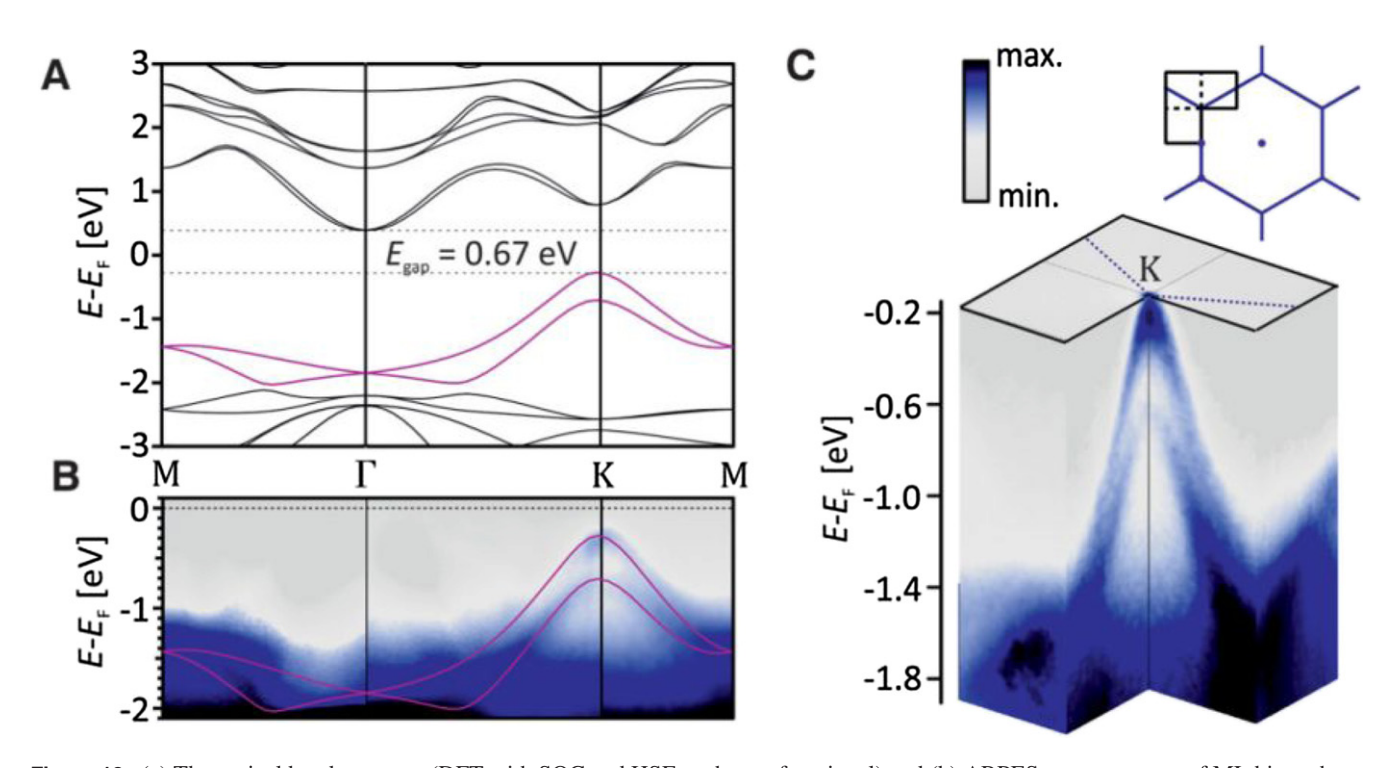


Figure 16. (a) Theoretical band structure (DFT with SOC and HSE exchange functional) and (b) ARPES measurements of ML bismuthene. The Fermi level lies at zero energy. (c) Close-up of the band splitting at the *K*-point from ARPES measurements. From [116]. Reprinted with permission from AAAS.

To study the interfacial properties of the ML bismuthene FETs, Guo *et al* chose Al, Ti, Ag, Au, Ir, Pt, and graphene as electrodes [123]. After contact with the metals, ML bismuthene undergoes a metallization, and the bands of ML bismuthene are hybridization because of a covalent bond formation in the vertical interface. The ML bismuthene FETs have n-type Schottky contact on the Ag, Ti, and Ir electrodes

and p-type Schottky contact on the Pt, Al, and Au electrodes. Strong FLP occurs at interface II because of an obvious MIGS, and the ML bismuthene FETs have a pinning factor S = 0.12 in the lateral interface (as shown in figure 17) [123].

Graphene is selected as an electrode to improve the interfacial properties of the ML bismuthene FETs. In the vertical direction, the direct bandgap is 0.58 eV without the SOC,

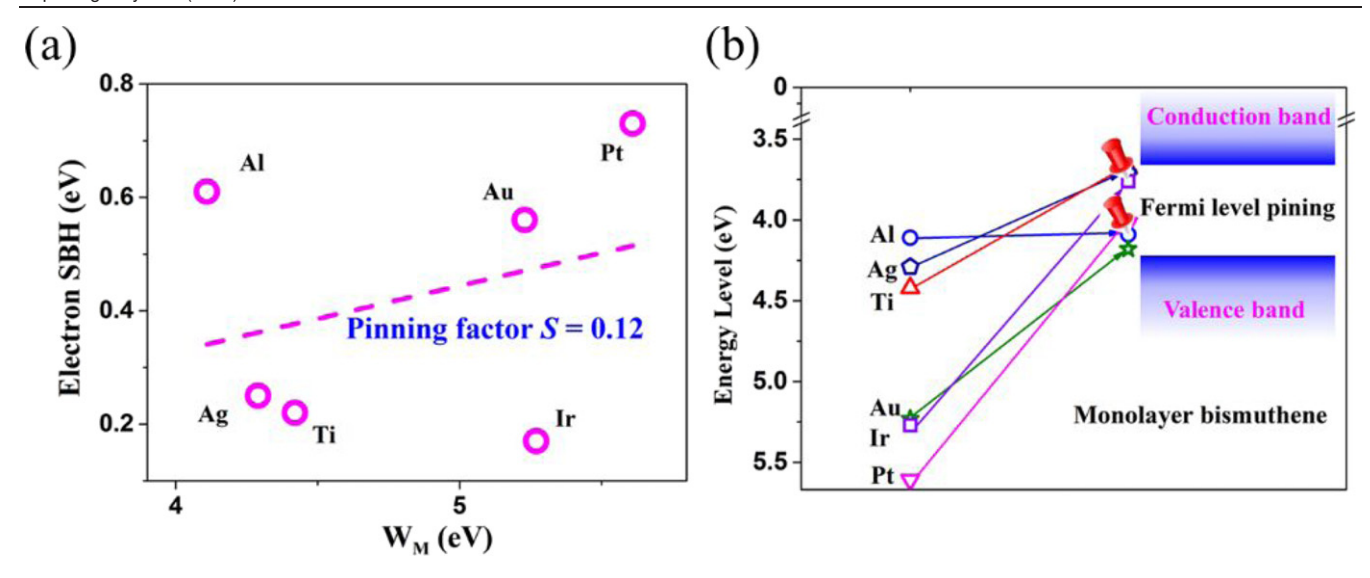


Figure 17. (a) Electron SBH of the ML bismuthene FETs using different metal contacts. (b) Illustration of the FLP in the ML bismuthene FETs. Reprinted with permission from [123]. Copyright (2017) American Chemical Society.

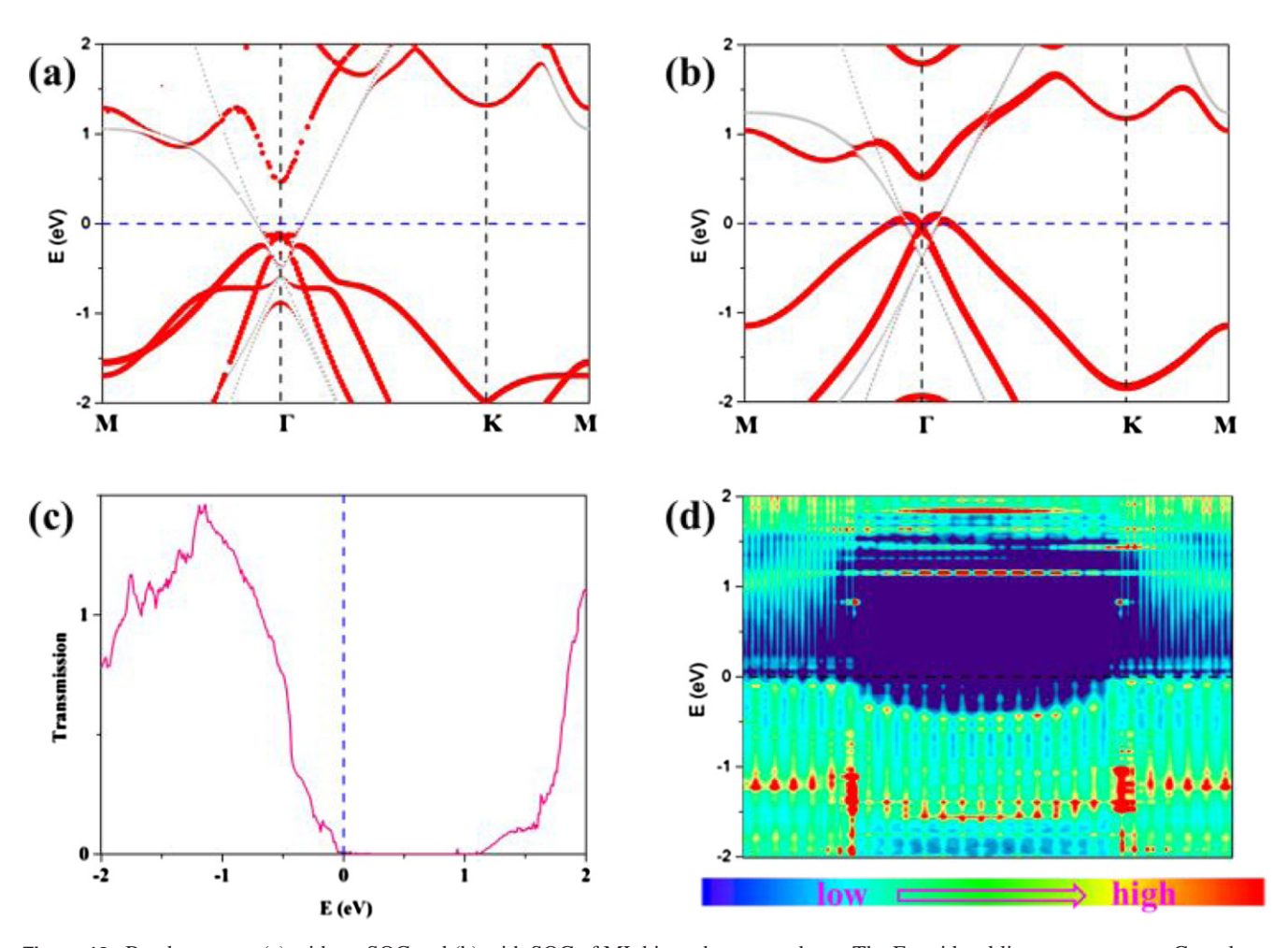


Figure 18. Band structure (a) without SOC and (b) with SOC of ML bismuthene–graphene. The Fermi level lies at zero energy. Gray dots represent the band structure of the compound system. Red dots represent the band structure projected on ML bismuthene, and the size of the dots is the corresponding weight. Transmission spectrum (c) and LDDOS (d) of the ML bismuthene FETs (with a channel-length \sim 5 nm) of graphene electrode without SOC ($V_{Gs}=0$ and $V_b=0$ eV). Reprinted with permission from [123]. Copyright (2017) American Chemical Society.

accompanied by a hole SBH 0.12 eV (p-type Schottky contact), while there is an indirect bandgap of 0.41 eV with the SOC, accompanied by a p-type Ohmic contact (figures 18(a) and (b)). In the lateral interface, the device has a quasi p-type Ohmic contact because of a little hole SBH of 0.06 eV without the SOC (figures 18(c) and (d)).

The VBM of ML bismuthene under graphene in the electrode region is rather flat. In such a case, the vertical and lateral SBH is equal. There is a vertical Ohmic contact from the BSC with the SOC. Hence, if the SOC is included in the QTS, a p-type lateral Ohmic contact should be available for the ML bismuthine FET [123].

3.2. Group VI 2DSC

Group VI tellurium (Te) is one of the chalcogen element family. Bulk Te consists of parallel-arranged helical Te atom chains held by vdW force [124]. Experimentally, both β -phase and α -phase ML and few-layer tellurene have been synthesized [125–127]. Theoretically, more than five stable or metastable phases for tellurene have been reported [128]. The most stable ML tellurene has the tetragonal β -phase, while the most stable few-layer tellurene has the α -phase derived from the bulk trigonal structure (figure 19) [124, 128, 129].

As an emergent star of the 2DSCs, tellurene has attracted much attention because of remarkable electronic properties. For instance, tellurene is an intrinsically p-type semiconductor with a layer-dependent band gap varying from the direct 0.33 eV (bulk) to indirect 0.92 eV (ML) [124, 126, 127, 132–135]. The p-type 2D tellurene FET fabricated by Wang et al has a large current on-off ratio of 10^6 and high field-effect mobility of $700 \text{ cm}^2 \text{ (V}^{-1} \cdot \text{s}^{-1})$ [127], later of which is higher than that of MoS_2 ($100-480 \text{ cm}^2$ ($100-480 \text{ cm}^$

Experimentally, the p-type 2D tellurene FETs have been successfully prepared by employing Pd and Ni metals with high work function as the electrode, and near Ohmic contact is formed [127, 142, 144, 145]. In contrast, the n-type 2D tellurene FETs are fabricated with a low work-function Ti electrode, and a Schottky contact is formed with higher contact resistance than that in the p-type FETs with Pd and Ni electrode, as shown in figure 20 [143].

Yan *et al* studied the interfacial properties of ML β -phase tellurene contacted with metals [130]. Seven common metals Sc, Ag, Cu, Au, Ni, Pt, Pd, and 2D graphene have been selected as electrode materials for the ML β -phase tellurene FETs. No vertical SBH exists in these ML tellurene-bulk metal systems owing to the strong band hybridization. The main band feature of ML tellurene contacted with graphene is maintained, indicating the weak vdW interaction. Moreover, the graphene electrode realizes a vertical p-type Ohmic contact with ML tellurene.

Lateral Schottky contacts are formed for all the bulk metal electrodes in the armchair direction. Sc and Au electrodes

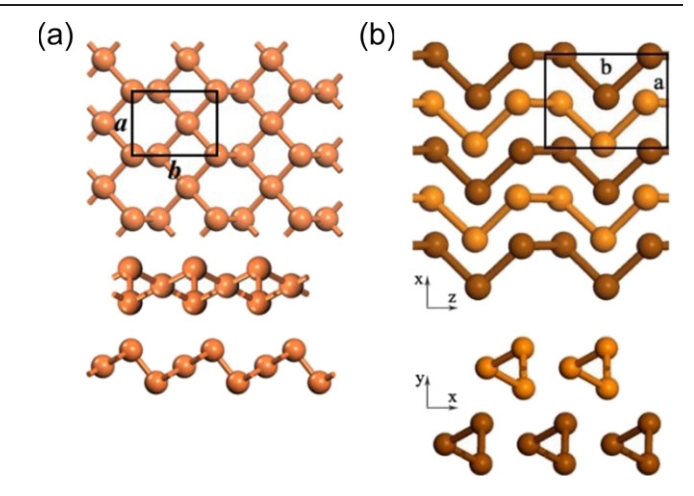


Figure 19. Structures of free-standing (a) ML β -phase and (b) BL α -phase tellurene. (a) Reproduced from [130] with permission of The Royal Society of Chemistry. (b) Reproduced from [131]. © IOP Publishing Ltd. All rights reserved.

generate n-type Schottky contacts while the other five bulk electrodes generate p-type Schottky contacts. Along the zigzag direction, the Sc electrode generates an n-type Schottky contact while the other six bulk metal electrodes form p-type Schottky contacts. Moreover, a lateral p-type Ohmic contact occurs in 2D graphene in these two directions. The calculated armchair-directed *S* is 0.15, and zigzag-directed *S* is 0.09 for the electrode-channel interface, respectively (figure 21). Relatively low *S* indicates that a strong FLP occurs in both the armchair and zigzag directions, and the degree of FLP in the armchair direction is lower than that in the zigzag direction.

For a few-layer tellurene, the α -phase is more stable than the β -phase. Figure 19(b) shows the structure of BL α -phase tellurene. Pristine BL α -phase tellurene is a p-type semiconductor with an indirect bandgap of about 0.96 eV. Experimentally, the mobility along the Te chain is higher than that perpendicular to the chain, and an average anisotropic mobility ratio is about 1.43 \pm 0.10 [127]. Pang *et al* studied the SBH in transistors based on the chain-directed BL tellurene. In the lateral direction, all these eight electrodes generate p-type Schottky contacts with BL tellurene [131]. Pang *et al* figured out a low pinning factor of 0.02 for BL tellurene transistor (figure 22), indicating an extremely intense FLP [131].

Because of the small work function of 4.61 and 4.51 eV for the ML and BL tellurene, a lateral p-type Schottky contact is favored to form both in the ML and BL tellurene contacted with metal electrodes, respectively [130, 131]. When the thickness of the tellurene increases, the band gap becomes smaller, and lateral electronic transmission efficiency is improved. Hence, the SBHs of the BL tellurene contacted with metal electrodes are generally lower than those of the ML ones.

4. Schottky barriers in the FETs based on compound 2DSCs

4.1. 2D transition-metal chalcogenide (TMC)

4.1.1. MoS_2 -metal top contacts. MoS_2 is a prototypical layered material held by weak interlayer vdW force [146, 147].

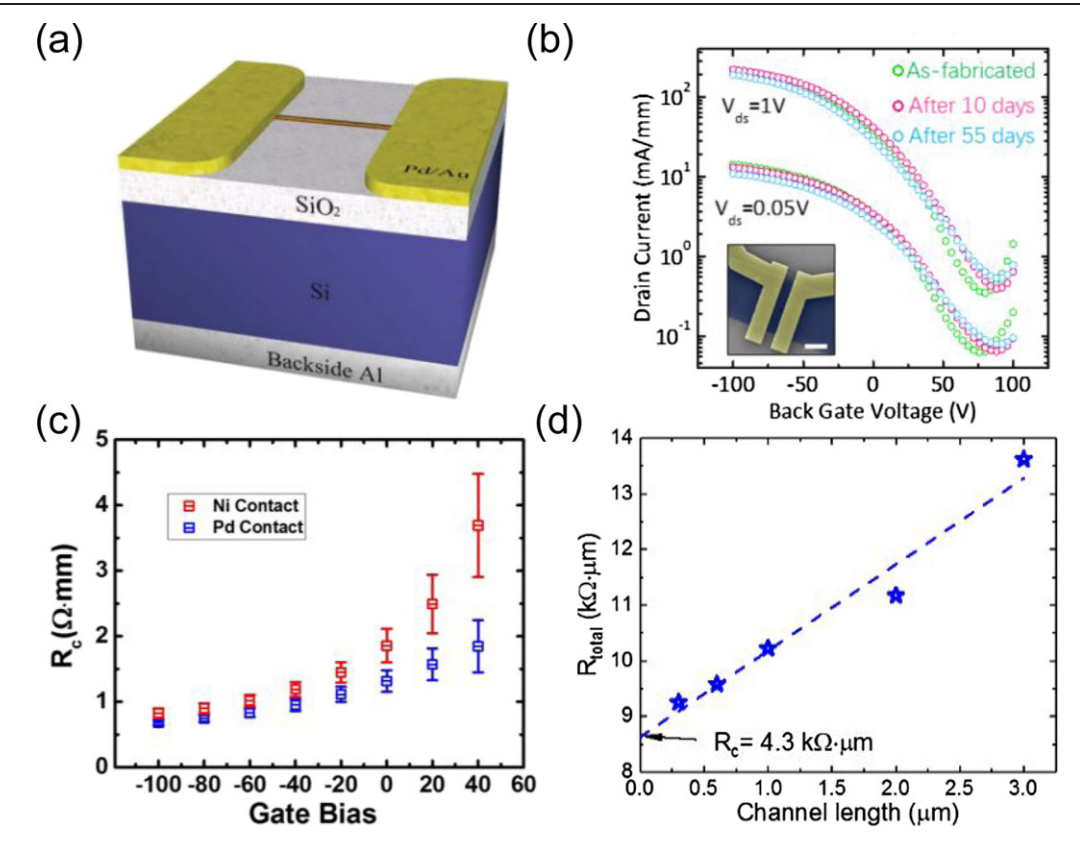


Figure 20. (a) Schematic of the p-type 2D tellurene transistor structure. (b) Transfer curves of 2D tellurene transistor and stability measured for about two months. The contact resistance of the p-type tellurene FET with Pd and Ni contacts (c) and n-type FET with Ti contact (d). (a) [142] John Wiley & Sons. © 2018 WILEY-VCH Verlag GmbH & Co. KGaA, Weinheim. (b), (c) Reprinted by permission from Springer Nature Customer Service Centre GmbH: Nature Electronics [127] © 2018. (d) Reproduced with permission from [143]. © IEEE.

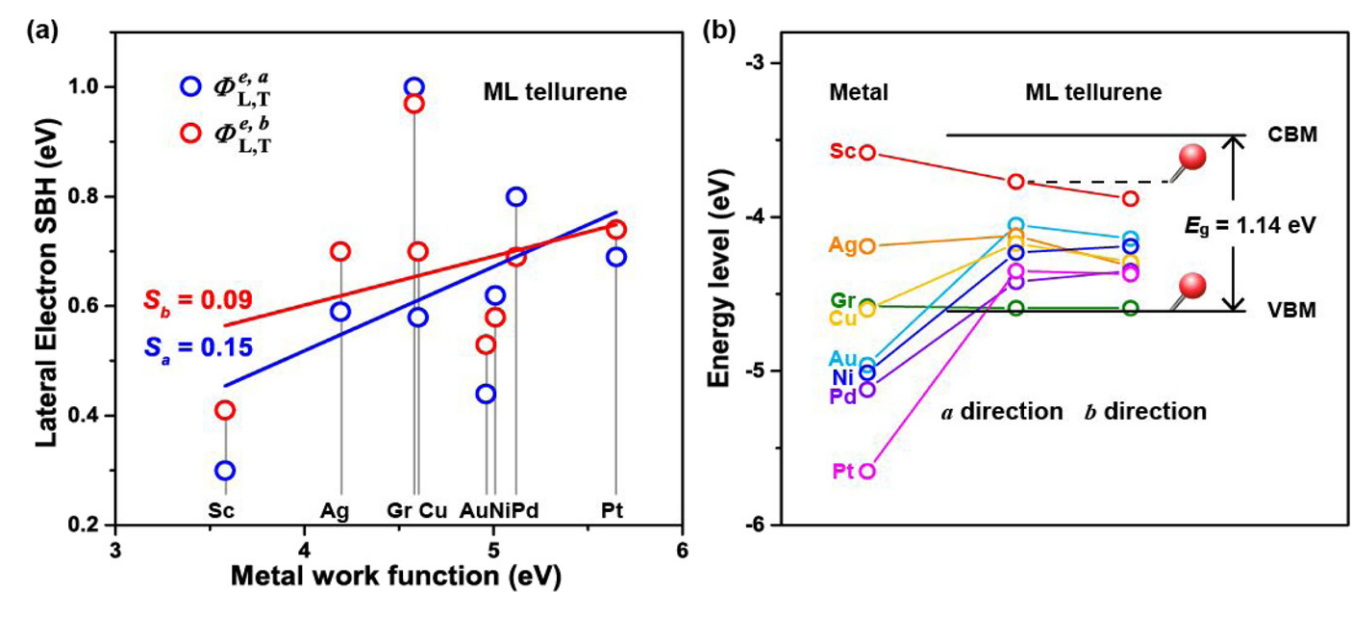


Figure 21. (a) Lateral electron SBH as a function of the metal work function in the armchair and zigzag direction for the ML tellurene FETs. (b) Schematic plot of the FLP for ML tellurene FETs. Reproduced from [130] with permission of The Royal Society of Chemistry, copyright 2018

Each layer is comprised of a sandwich S-Mo-S unit boned by strong intralayer covalent force [146, 148–150]. MoS₂ has three main phases (figure 23(b)): metallic tetragonal phase (1T) has one layer per repeat unit with octahedral coordination

[151–154]; semiconducting hexagonal phase (2H) possesses two layers per unit cell with trigonal prismatic coordination [153, 155, 156]; and semiconducting rhombohedral phase (3R) owns three layers with trigonal prismatic coordination

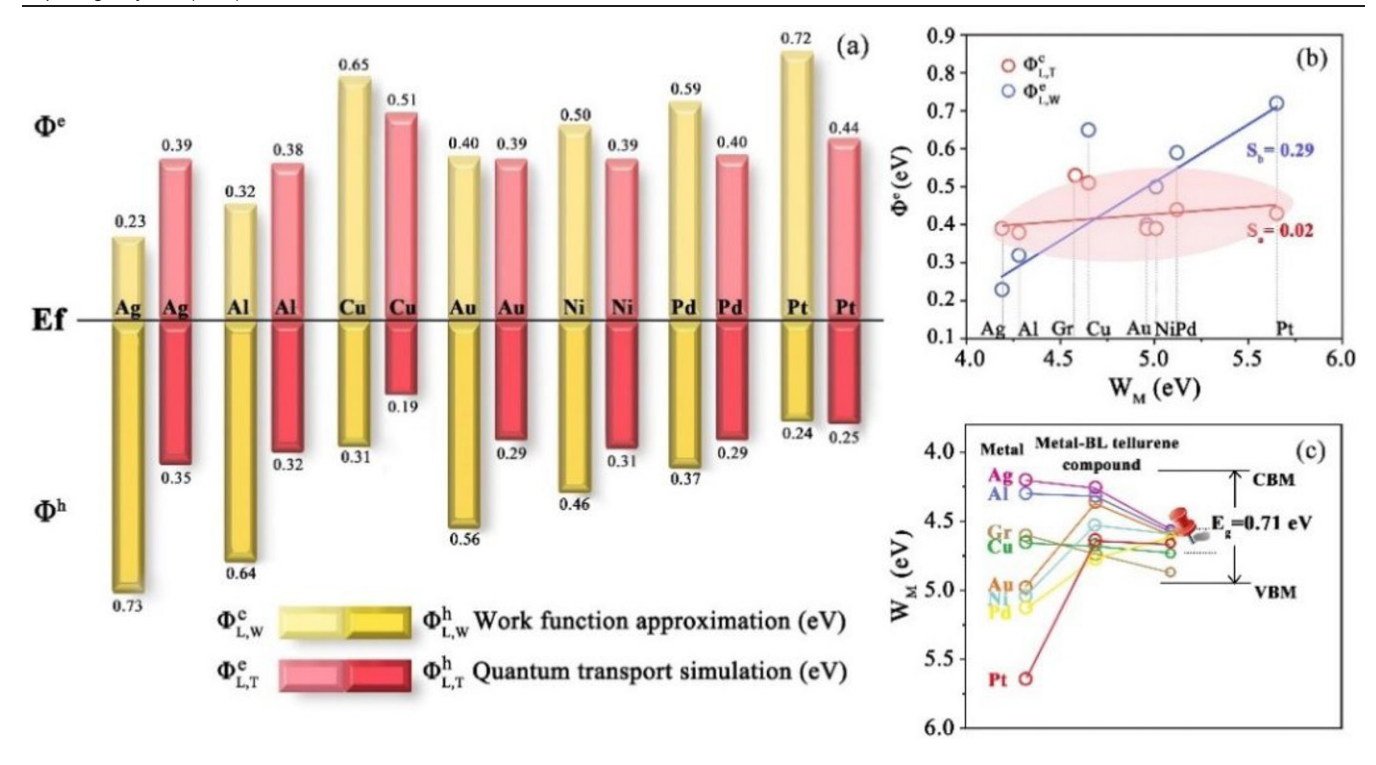


Figure 22. (a) The lateral SBHs of the BL tellurene FETs from the WFA and QTS methods. (b) Lateral electron SBH for BL tellurene FETs as a function of the metal work function. (c) Schematic plot of the FLP for the BL tellurene FETs. Reproduced from [131]. © IOP Publishing Ltd. All rights reserved.

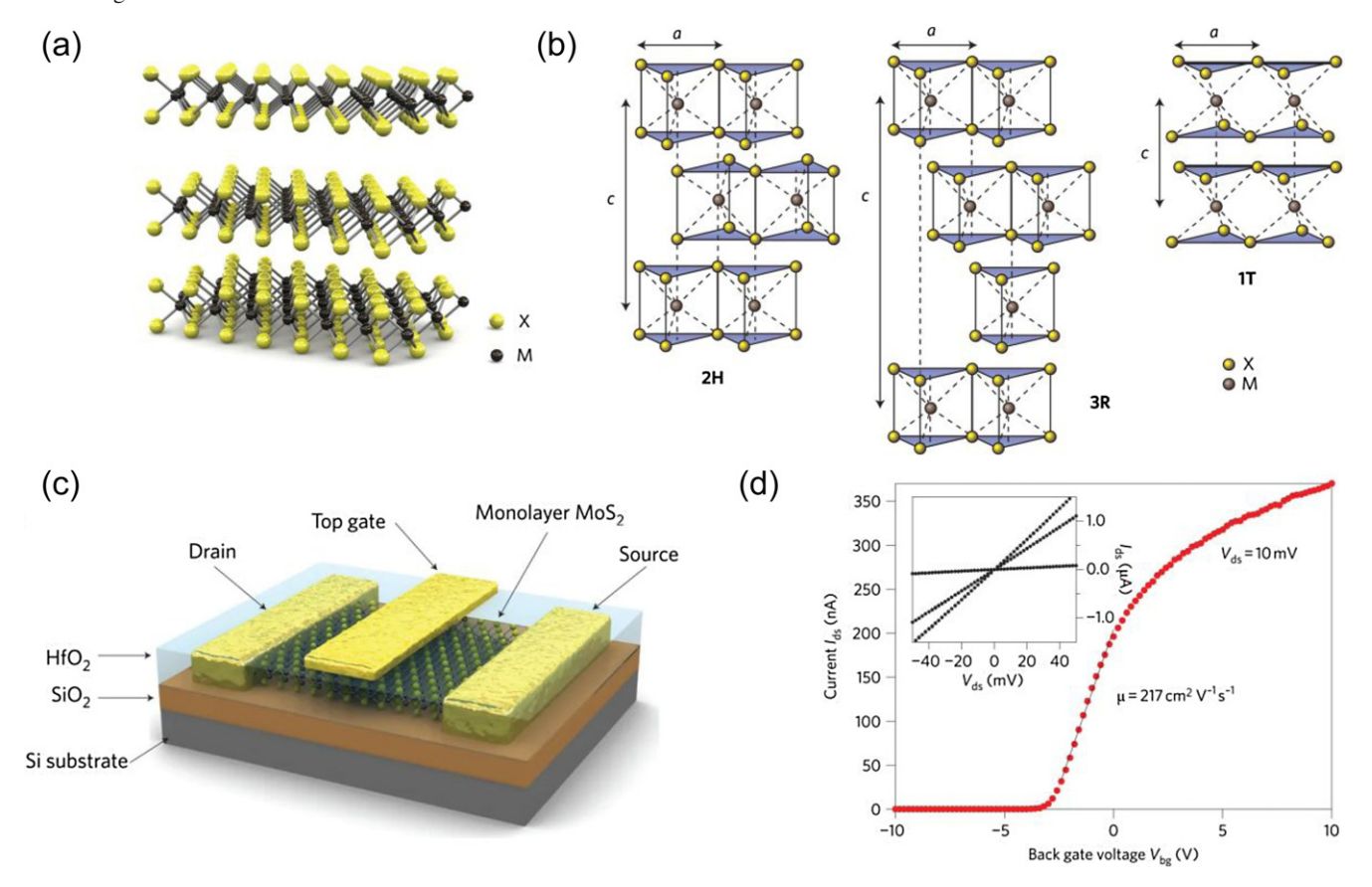


Figure 23. (a) Structure of MoS_2 . (b) Structures of hexagonal 2H, rhombohedral 3R, and tetragonal 1T. (c) Schematic view of one of the ML MoS_2 transistors. (d) Room-temperature transfer characteristic for the ML MoS_2 FET. (b) Reprinted by permission from Springer Nature Customer Service Centre GmbH: Nature Nanotechnology [154] © 2012. Reprinted by permission from Springer Nature Customer Service Centre GmbH: Nature Nanotechnology [14] © 2011.

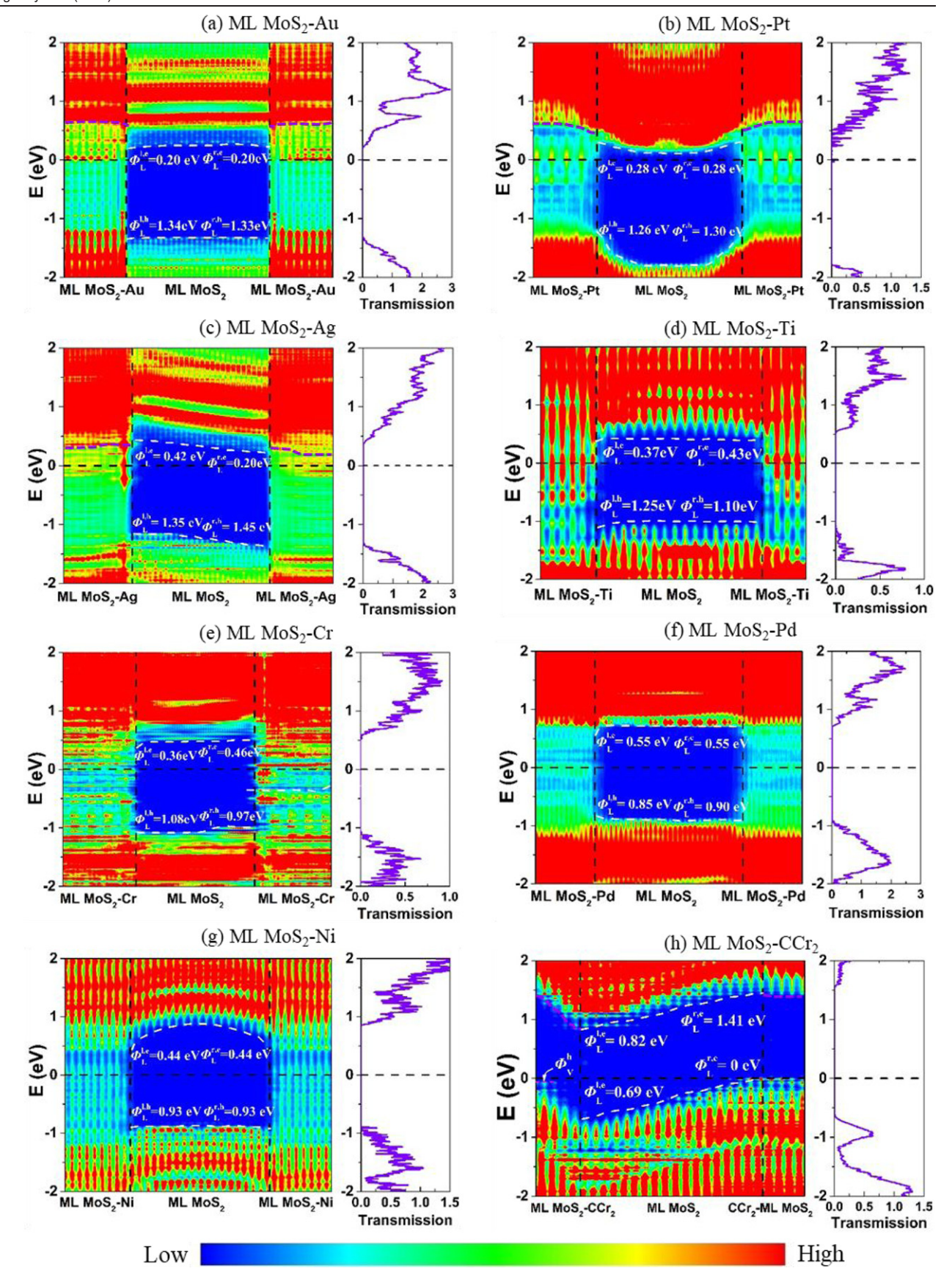


Figure 24. LDDOS and transmission spectra of the ML MoS₂ FETs with different metal electrodes. Adapted with permission from [164]. Copyright (2019) American Chemical Society.

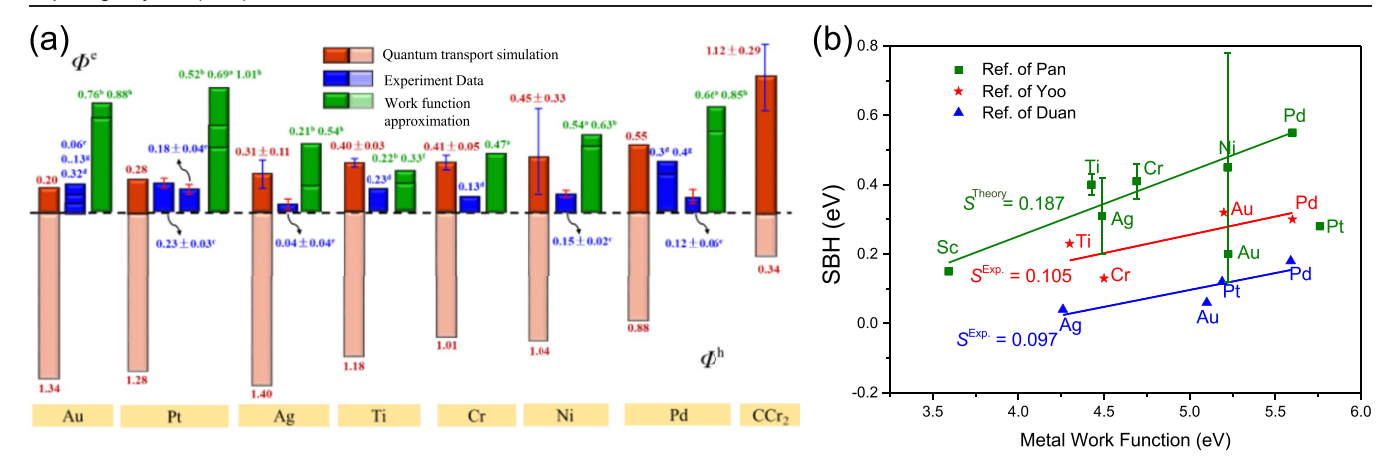


Figure 25. (a) Lateral SBHs of the ML MoS₂ FETs with different metal electrodes from the QTS, WFA, and experiments. (b) SBHs of ML MoS₂ vs the work function of metals. The green squares, red stars, and blue triangles represent the *ab initio* QTS results by Pan *et al* [164] and the experimental results by Kim *et al* [158] and Liu *et al* [31], respectively. Adapted with permission from [164]. Copyright (2019) American Chemical Society.

[154, 156]. 2D 2H–MoS₂ is mostly studied. Therefore, we denote '2H–MoS₂' as 'MoS₂' hereafter without a special statement. MoS₂ undergoes a transition from the indirect bandgap of 1.2 eV in bulk to the direct bandgap of 1.9 eV in ML based on the DFT calculations [146]. The ML MoS₂ FET fabricated by Radisavljevic *et al* [14] possesses high mobility of 200 cm² (V⁻¹·s⁻¹) and a huge current on-off ratio of 10⁸ (figure 23(d)). Besides, Desai *et al* [157] fabricated a 1 nmgate-length BL MoS₂ FET contacted Ni electrode with a high current on-off ratio of 10⁶. Hence, 2D MoS₂ is a promising candidate as the FET channel material.

It is necessary for 2D MoS₂ FETs to realize low resistant contacts by using appropriate metal electrodes. So far, 2D MoS₂-metal contacts have been extensively studied in experiments. Fabricated Co, Cr, Ag, Cu, Au, Pd, and Pt electrodes form n-type Schottky contacts with ML MoS₂ [31,41,66,158], while the contacts for transferred Au, Pd, and Pt electrodes fabricated by Liu *et al* [31] turn to be p-type. Ti electrode is reported to generate n-type Schottky contacts with ML and BL MoS₂ with SBHs of 0.23 and 0.065 eV in experimental work, respectively [155, 158]. Moreover, both n- and p-type characteristics have been reported for the Pd electrode on ML and multilayer MoS₂ transistors [66, 159, 160]. Das *et al* [65] found that Sc, Ti, Ni, and Pt form n-type Schottky contacts with multilayer MoS₂ with SBHs of 0.03, 0.05, 0.15, and 0.23 eV, respectively.

To make a comprehensive examination of metal contacts to ML and few-layer MoS₂, Zhong *et al* [13, 64, 161–163] investigated the interfacial properties of ML and BL MoS₂-metal contacts by using *ab initio* BSC, and Pan *et al* [164] further reexamined the SBHs in ML MoS₂ FETs by using *ab initio* QTS.

Zhong *et al* [64] selected six commonly used metals Sc, Ti, Ag, Pt, Ni, and Au as electrode materials for ML and BL MoS₂ transistors and studied the vertical SBH using the BSC. No vertical SB occurs at the ML/BL MoS₂-metals interface for Sc and Ti electrodes because of the strong band hybridization, resulting in an Ohmic contact. Moreover, Ag

and Ni electrodes realize vertical n-type Schottky contacts while Pt forms a p-type Schottky contact with ML/BL MoS₂. Au surface generates a midgap Schottky contact with ML MoS₂ and a vertical n-type Schottky contact with BL MoS₂. Kang *et al* [13] reported that Mo, Ti, In, and Au form vertical n-type Schottky contacts, and Pd forms a midgap Schottky contact with ML MoS₂. It is reported by Chen *et al* [162] that Ir, Ru, and Pd generate vertical n-type Schottky contacts with ML MoS₂. Gong *et al* [163] reported that ML MoS₂ is formed vertical n-type Schottky contacts with Al, Ag, Au, Pd, and Ir and a vertical p-type Schottky contact with Pt.

Lateral SBH of ML and BL MoS2 were theoretically determined by the Schottky–Mott limit, WFA, and QTS [64, 164, 165]. In order to consider the complex coupling at the electrode-channel regions in transistors, Pan et al examined the lateral SBHs in the ML MoS₂ FETs with Au, Pt, Ag, Ti, Cr, Pd, Ni, and ML CCr₂ electrodes [164] using the QTS. The LDDOS of the ML MoS₂ FETs has been depicted in figure 24. Lateral n-type Schottky contacts are formed for ML MoS₂ contacted with Au, Pt, Ag, Ti, Cr, Pd, and Ni electrodes. On the contrary, ML CCr₂ electrode forms a lateral p-type Schottky contact with ML MoS₂. A band bending occurs for ML MoS₂ under Pt (medium adhesion) as a result of charge transfer between regions B and C. Such a band bending is rather localized compared with that in the case of weak adhesion, such as the ML MoS₂-ML CCr₂ contact (figure 24(h)) and the ML antimonene-BN-Sc, -graphene-Sc, and -graphene contacts (figures 15(c)-(e)).

The SBHs extracted from the QTS are compared with those from other calculations and the experiments in figure 25(a). Notably, a lateral n-type Schottky contact for the Pt electrode obtained by the QTS is consistent with the experimental work [65] when the coupling at the electrode-channel regions is fully considered. In contrast, the other calculation gave the opposite result that Pt forms a p-type contact with ML MoS₂ [64]. The SBHs from the QTS are closer to those from the experiments than those extracted by other calculations for Au, Pt, Ag, Ni, and Pd electrodes. The opposite doping type for ML

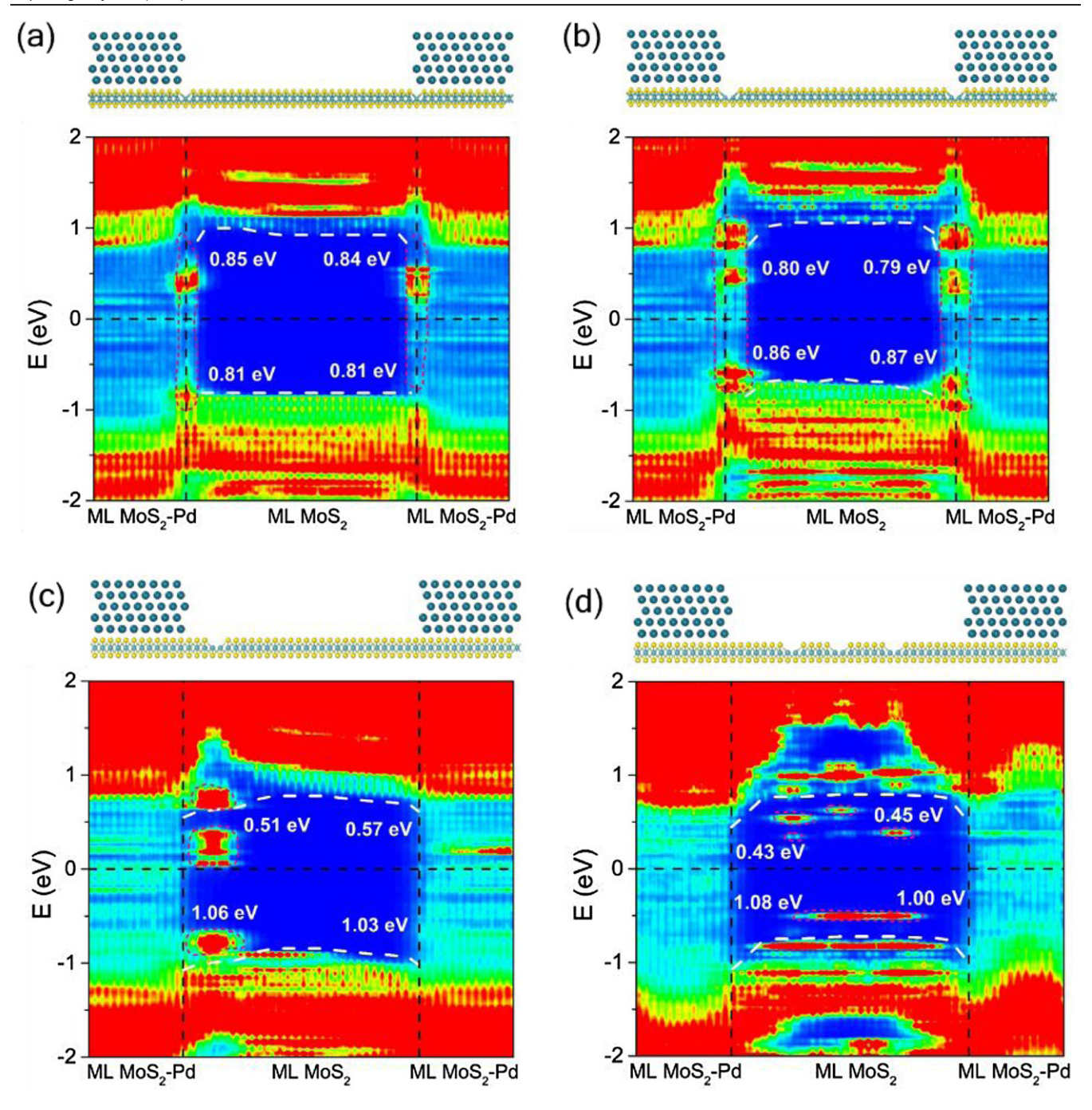


Figure 26. (a)—(d) Side views and LDDOS in color coding for the ML MoS_2 FET of Pd electrode with (a) two interfacial defects, (b) four interfacial defects, (c) two channel defects, and (d) six channel defects in the built device models, respectively. White dash lines represent the band edge of the channel ML MoS_2 . The defect-induced gap states are marked by the rose-red short dash circles. Adapted with permission from [164]. Copyright (2019) American Chemical Society.

MoS₂ contacted Pt, and the large overestimation of the SBHs from other calculations are ascribed to the ignorance of the complex coupling. The theoretical *S* of 0.187 from the QTS is closer to the experimental values of 0.097 [31] and 0.105 [158] for ML MoS₂ (figure 25(b)). While *S* from the Schottky–Mott limit or WFA evaluation is about 0.3, which is apparently overestimated [63–66]. Therefore, the QTS turns out to be an improved method to determine the lateral SBH and *S* of a FET.

The dangling-bond-free interfaces and no defects were also considered in the QTS. The slight overestimation of the SBH and *S* in the QTS is attributed to the defects in the experimental samples [158, 164].

Perfect crystal structure and homogeneous and sharp interface are assumed in the above QTS. However, atomic defects are observed at the interface of the 2D MoS_2 FETs [31, 166, 167]. The slight overestimation of the SBH and S in the above QTS is attributed to the existence of defects in the

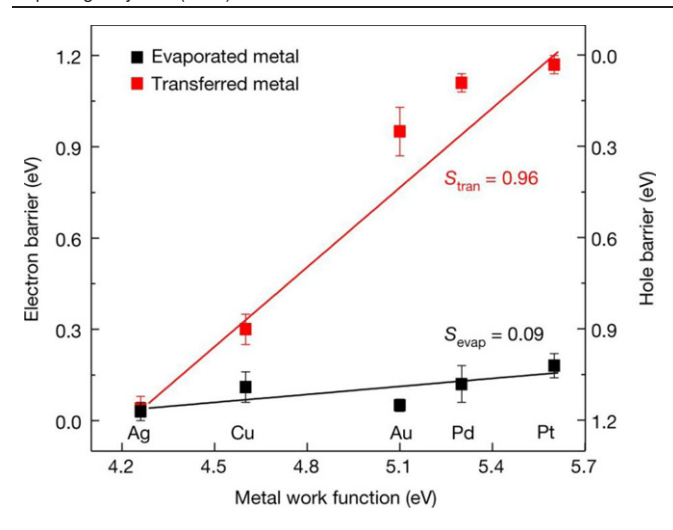


Figure 27. Experimentally determined SBHs in the ML MoS_2 FET for different transferred metals and evaporated metals. Reprinted by permission from Springer Nature Customer Service Centre GmbH: Nature [31] \otimes 2018.

experimental samples [158, 164]. The existence of defects in 2D MoS₂ leads to a variation of its electronic properties and can induce extra electron states in the band gap, which are referred to as defect-induced gap states. The defect-induced gap states at the interface function as the MIGS and surface states and usually determine the Fermi-level's effective pinning position (To be specific, the Fermi level is pinned close to the characteristic level of the defects) or even differences in CNL of different 2D materials if their concentration is high enough [17]. The effects of the interfacial and channel defects of the ML MoS₂ FETs are also investigated with Pd electrodes by using QTS, and the results are shown in figure 26 [164]. Both the interfacial and channel defects give rise to gap states in the ML MoS₂ FETs. With the increase of the defects, the electron SBH of the ML MoS₂ FETs decreases.

Moreover, Liu *et al* [31] fabricated vdW metal–ML MoS₂ junctions that contain dangling-bond-free ML MoS₂ and atomically thin electrodes laminated onto the ML MoS₂ surface. Such a chemical bond-free metal–ML MoS₂ interface essentially eliminates the gap states. Compared with the conventional evaporated metal–ML MoS₂ junctions with a low *S* of 0.09, these transferred metal–ML MoS₂ junctions overcome the FLP with a huge *S* of 0.96, approaching the Schottky–Mott limit (figure 27).

4.1.2. MoSe₂-metal top contacts. MoSe₂, as a Se counterpart of MoS₂, has a layer-dependent bandgap from 1.1 eV in bulk (indirect) to 1.5 eV in ML (direct) [61, 168]. The large size and high-quality ML and few-layer MoSe₂ have been synthesized by mechanical exfoliation and chemical vapor deposition [141, 169]. What is more, few-layer MoSe₂ FETs also have been fabricated with Ni and Ti as electrodes. The field-effect mobility of the MoSe₂ FETs is 150–200 cm² (V⁻¹·s⁻¹), and the current on-off ratio is up to 10⁶ [139–141, 170]. Thus, 2D MoSe₂ is comparable with 2D MoS₂ in the potential nanoelectronic applications.

Çakır *et al* studied the interfacial properties of ML MoSe₂ with Sc and Au electrodes by applying the first principles BSC and QTS (figure 28) [171]. Sc and Au electrodes form an n- and p-type Schottky contact with ML MoSe₂, respectively, with the corresponding electron/hole SBH of around 0.20 and 0.5 eV. Pan *et al* reported the contact properties in the ML MoSe₂ FETs with a series of metals Ag, Al, Ti, Cr, Ni, and Pt (figure 28) [172]. The QTS method predicts that an n-type lateral Schottky contact takes shape with Ag, Al, and Ti electrodes, characterized by electron SBH of 0.25, 0.56, and 0.29 eV, respectively, and a p-type lateral Schottky contact takes shape with Pt electrode with hole SBH of 0.78 eV.

4.1.3. $MoTe_2$ -metal top contacts. The ML MoTe₂ is reported as another promising TMDC with a smaller bandgap of 1.28 eV than the ML MoS₂ [173]. Different from the inherent n-type behavior of MoTe₂, the polarity of the 2D MoTe₂ can be modulated through light and electrostatic activation [174] and used in the ambipolar FETs [175]. The MoTe₂ FET fabricated in 2014 exhibits a high on-off ratio of $\sim 10^6$, a SS of 140 meV/dec, and field-effect mobility of 10 cm² V⁻¹ s⁻¹ [175, 176]. Later, the heterophase homojunction MoTe₂ transistors are reported to show significantly enhanced field-effect mobility of 50 cm² V⁻¹ s⁻¹ [177]. Recently, the sub-10 nm FETs are fabricated and show good switching characteristics with an on-off ratio of 10^5 and a SS of 73 meV/dec [174].

The interfaces between ML MoTe2 and metals are investigated both theoretically and experimentally, as shown in figure 29 [24, 158]. The experiment shows that the lowest effective hole SBH of 0.14 eV in ML MoTe₂-Au contact. The extraordinarily strong FLP effect with S = 0.07 is shown in the experiment [158]. The BSC predicted larger SBHs of 0.5-0.9 eV and a larger S = 0.17. The researchers ascribe such a discrepancy to that the BSC method ignores the coupling between the electrode and the channel. The charge neutrality level of ML MoTe₂ is 0.22 eV higher than the VBM; therefore, ML MoTe₂ is more likely to form p-type contact with metals. Besides, the contact resistance in the FET configuration is examined to be exponentially proportional to the SBHs. Chemical doping methods involving viologen or AuCl₃ is reported to weaken the FLP effect in ML MoTe₂-metal contact, which can realize the modulation of both the SBH and the contact resistance [11, 178].

4.1.4. WS_2 -metal top contacts. Another common TMDs material is WS_2 , whose ML form has a finite bandgap reported in a range of 1.8–2.2 eV [179, 180]. ML WS_2 is of reasonably high carrier mobility, reported as 214/486 cm² V⁻¹ s⁻¹ in room temperature/5 K [181], leading to the outstanding performance of ML WS_2 device. ML WS_2 FETs are predicted to surpass ML MoS_2 counterpart in terms of the on-current [179] and show a high on-off ratio of about 10^5 – 10^6 in experiments [182].

Tang et al studied the SBH between ML WS₂ and six common metals (Sc, Ti, Ag, Cu, Au, Pt) and compared with the previous experiments [180]. In the vertical interfaces, n-type SBs exist for Au, Ag, and Cu electrodes with the electron SBHs of 0.41, 0.17, and 0.50 eV, respectively, while ML WS₂ under

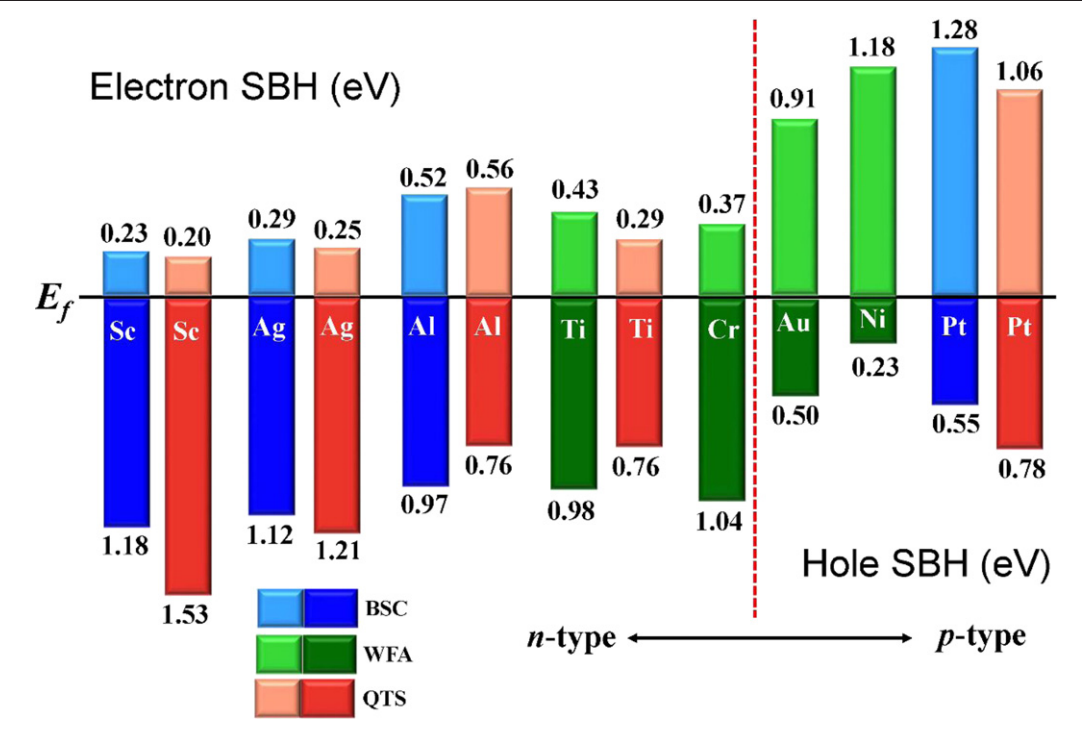


Figure 28. SBHs in the ML MoSe₂ FET with Sc, Ag, Al, Ti, Cr, Au, Ni, and Pt electrodes through the BSC, WFA, and QTS methods, respectively. Reprinted figure with permission from [171]. Copyright (2014) by the American Physical Society. Reprinted with permission from [172]. Copyright (2016) American Chemical Society.

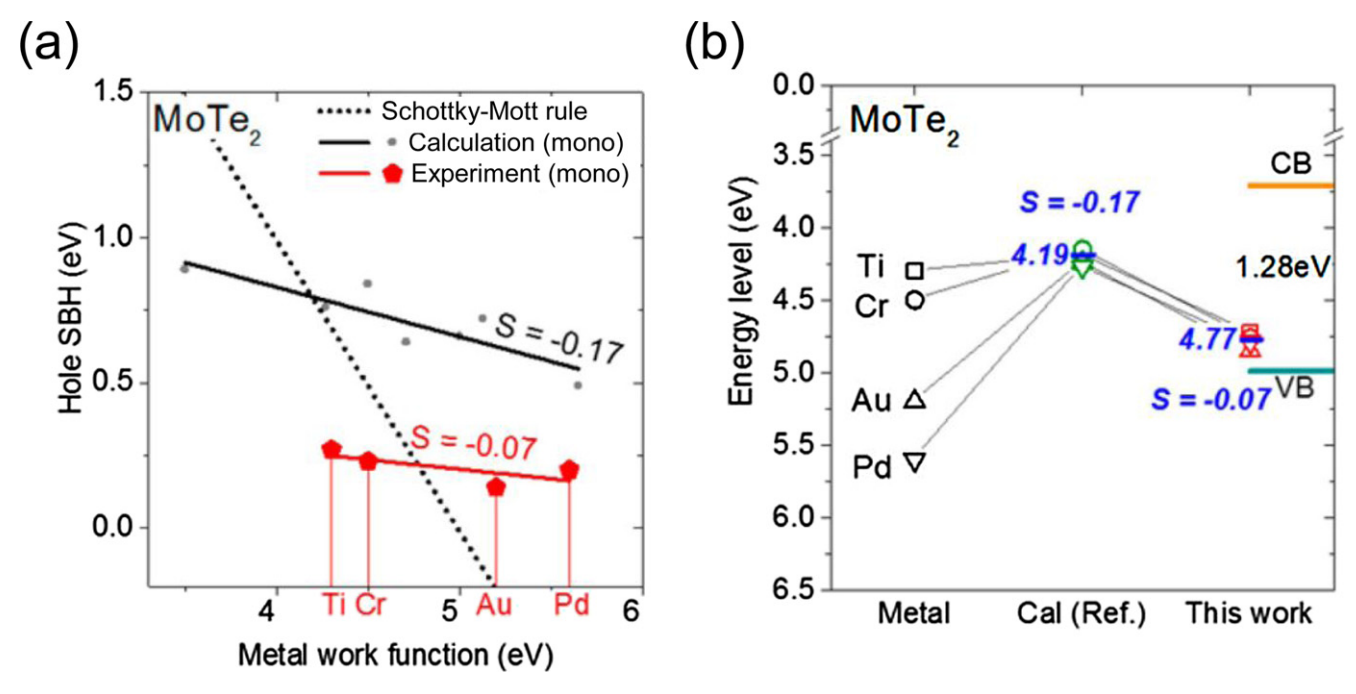


Figure 29. (a) Hole SBH of ML MoTe₂ as a function of metal work functions obtained from experiments (red) and calculations (black). The dotted line represents the prediction given by the Schottky–Mott rule. (b) FLP for the theoretical SBH and measured SBH for ML MoTe₂. Reprinted with permission from [158]. Copyright (2017) American Chemical Society.

Sc, Ti, and Pt are metalized without the existence of the vertical SBs. Unfortunately, lateral SBs form in all the investigated interfaces according to the QTS, as shown in figure 30(a). Ntype Schottky contact exists with the lateral electron SBHs of 0.28, 0.36, 0.25, 0.46, 1.00 eV for Sc, Ti, Ag, Cu, and Au

electrode, respectively, while p-type Schottky contact takes shape, accompanied by a lateral hole SBH of 0.98 eV for Pt electrode. Experiments show that the vertical electron SBH for Au is 0.40 eV, and the lateral electron SBH for Ti and Pt is 0.24 and 0.23 eV, respectively, close to the calculation results. The

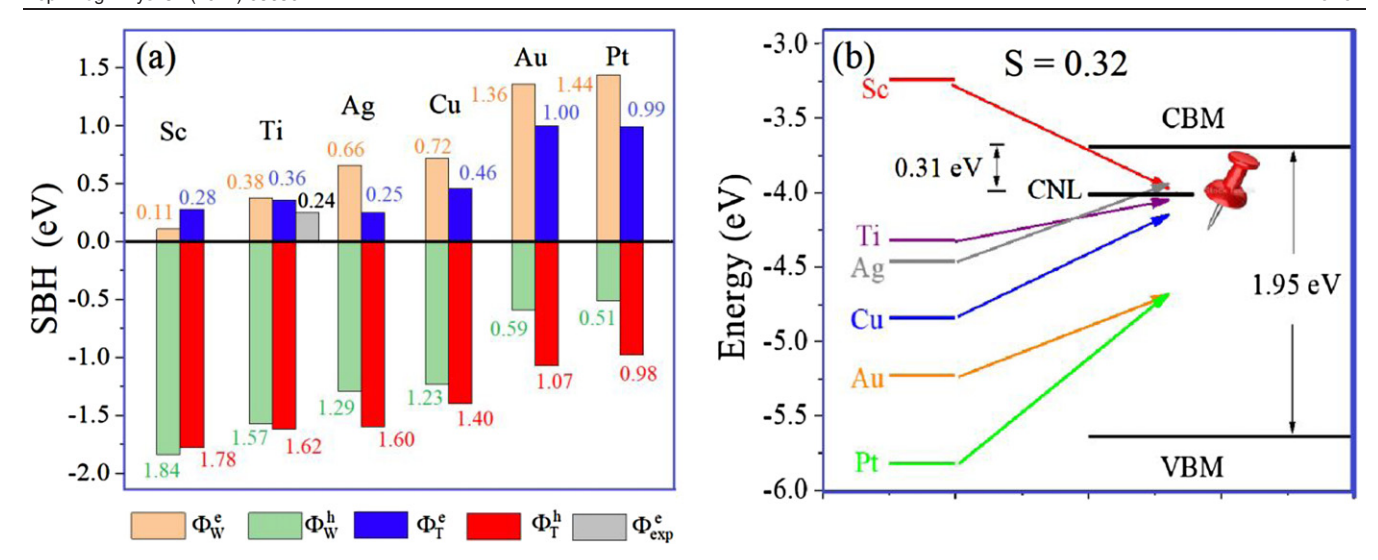


Figure 30. (a) Electron and hole SBHs for the ML WS $_2$ FETs calculated by the WFA ($\Phi_W^{e/h}$) and QTS ($\Phi_T^{e/h}$). Φ_{exp}^e is the experimental SBH value. (b) Illustration of FLP in ML WS $_2$ -metal contacts. The Fermi levels are pinned to the CNL, 0.31 eV below the CBM, and the average pinning factor \overline{S} is equal to 0.32, according to the QTS. [180] John Wiley & Sons. © 2019 WILEY-VCH Verlag GmbH & Co. KGaA, Weinheim

small discrepancy can be caused by the defects and/or impurities in the experimental condition in contrast with the ideal lattice in the calculation.

ML WS $_2$ is prone to n-type Schottky contact with metals, as metals' Fermi level is partly pinned to the CNL located 0.31 eV below the CBM in the upper part of the gap, as displayed in figure 30(b). The pinning factor is calculated by both the linear fitting of the SBHs and equation (4), showing S=0.32 and S=0.28, respectively. When using equation (4) for calculation, parameters N and δ are extracted from the LDDOS at the Fermi level. Such results show reasonable consistency, strengthening their reliability. The pinning factor of ML WS $_2$ is larger than some other TMDs like MoS $_2$ and MoTe $_2$, demonstrating the relatively weak pinning effect. This is probably because the influence of electrodes introduces fewer MIGS around the Fermi level to the ML WS $_2$ channel, as implied by the LDDOS results.

ML WS₂ is prone to n-type Schottky contact with metals, as metals' Fermi level is partly pinned to the CNL located 0.31 eV below the CBM in the upper part of the gap, as displayed in figure 30(b). The pinning factor is calculated by both the linear fitting of the SBHs and equation (4), showing S = 0.32and S = 0.28, respectively. When using equation (4) for calculation, parameters N and δ are extracted from the LDDOS at the Fermi level. Such results show reasonable consistency, strengthening their reliability. The pinning factor of ML WS₂ is larger than some other TMDs like MoS₂ and MoTe₂, demonstrating the relatively weak pinning effect. This is probably because the influence of electrodes introduces fewer MIGS around the Fermi level to the ML WS2 channel, as implied by the LDDOS results. Here we emphasize that the calculations in [180] do not consider the SOC effects that could be evident for the heavy element like W. The SOC splits the CBM and VBM and is likely to results in smaller SBs. However, the general trend in figure 30 holds true considering its consistency with experiments.

4.15. WSe₂-metal top contacts. The 2D WSe₂, another intensively studied 2D TMD, is characterized by its strong SOC [183, 184] and preference of p-type doping compared with other 2D TMDs [13, 14]. The bandgap of ML (BL) WSe₂ is 1.60 (1.43) and 1.33 (1.15) eV [185] with and without considering SOC, respectively, showing the evident reduction by the SOC of 0.27 (0.28) eV that makes 2D WS₂ suitable for spintronic applications. The WSe₂-MoS₂ p-n heterojunctions are fabricated in experiments with outstanding rectification and photoresponse [186, 187]. The experimentally fabricated WSe₂-based FETs are confronted with limited on-current [15, 188], which is possibly attributed to the high-resistance contact between WSe₂ and the electrodes. Such difficulties address the importance of searching for electrode materials with optimal interfacial properties.

Wang et al investigated the interfacial properties between 2D WSe₂ and common metals (Sc, Al, Ag, Au, Pd, Pt) by the first-principles BSC method considering the SOC effects [185]. The calculated SBs of ML and BL WSe₂ are shown in figures 31(a) and (b). The general comparison shows that two kinds of coupling effects can reduce the vertical SBH: (1) the SOC generally reduces the p-type vertical SBH. Remarkably, the p-type Ohmic contact is predicted for both ML WSe₂-Pt and BL WSe₂-Pt vertical interfaces. (2) The interlayer coupling in the BL WSe2 reduces both n-type SBH and p-type SBH. Besides the WSe₂-Pt contact, the ML (BL) WSe₂-Pd and WSe₂-Sc vertical interfaces are also predicted as low resistance contacts due to the low p-type SBs of 0.23 (0.09) and n-type SBs of 0.25 (0.25) eV, respectively. Therefore, Pt (the best) and Pd are recommended as electrode materials that form low resistance p-type contacts while Sc is recommended for n-type contacts in ML or BL WSe2 based devices.

The calculations of the lateral SBHs considering the SOC are still in lack due to computational costs. Generally, the lateral SBHs are not equal to the vertical SBHs because of the curve of band edges at interface II. Nevertheless, the band

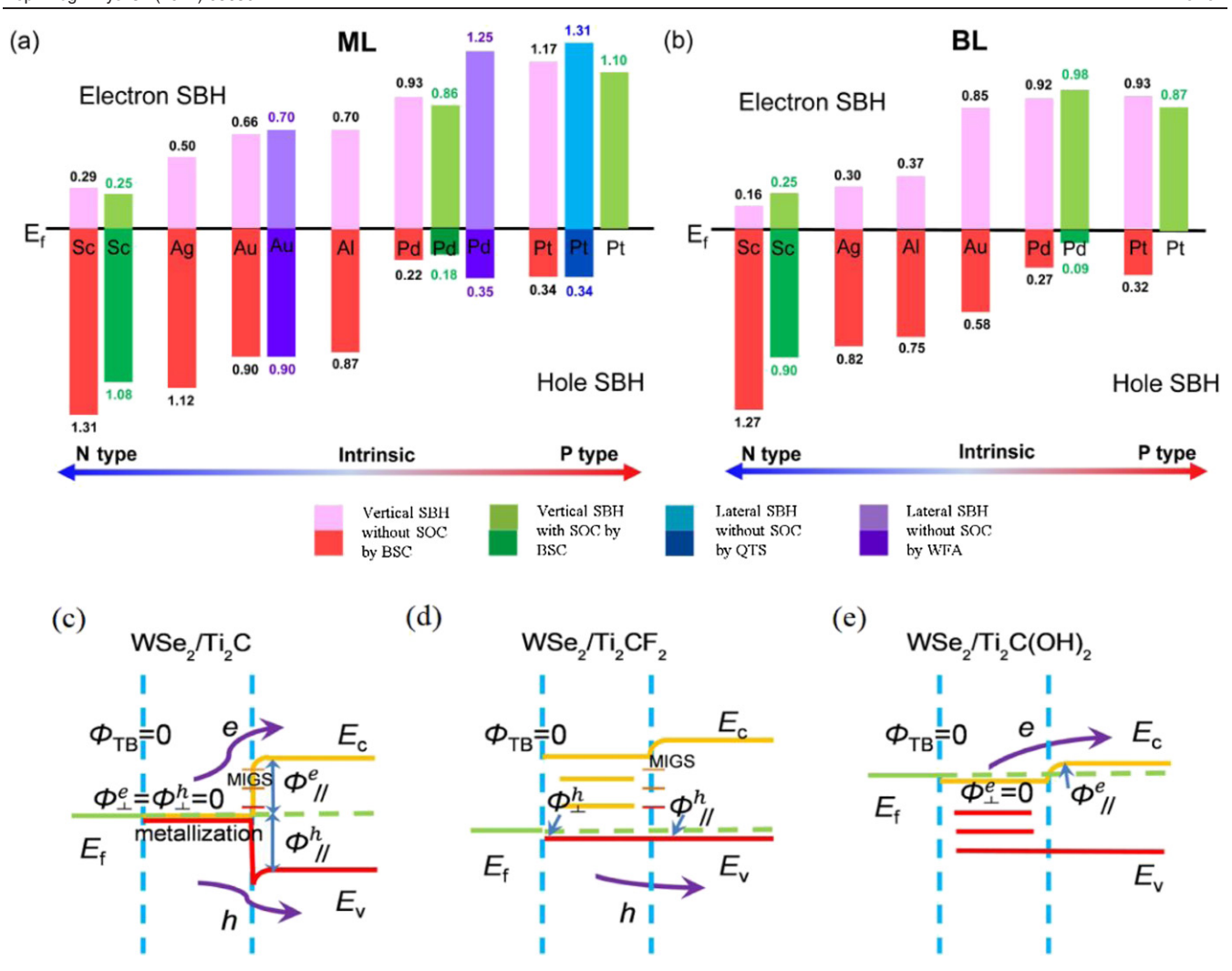


Figure 31. Calculated SBH of (a) ML WSe₂—metal contacts and (b) BL WSe₂—metal contacts by the GGA of DFT. The light (deep) red, green, and blue bars represent the electron (hole) vertical SBH without SOC, the vertical SBH with SOC, and the lateral SBH without SOC adopted from [185], the purple bar represents the lateral SBH without SOC adopted from [13]. (c) The real space band structures of ML WSe₂–2D titanium carbides contacts. The blue dash lines separate the space into 2D titanium carbides, the contact area, and ML WSe₂ from left to right. The green (solid/dash), yellow, and red lines represent the Fermi level, the CBM, and the VBM, respectively. (a), (b) Reproduced from [185] with permission of The Royal Society of Chemistry. (c)–(e) Reprinted from [189], Copyright (2018), with permission from Elsevier.

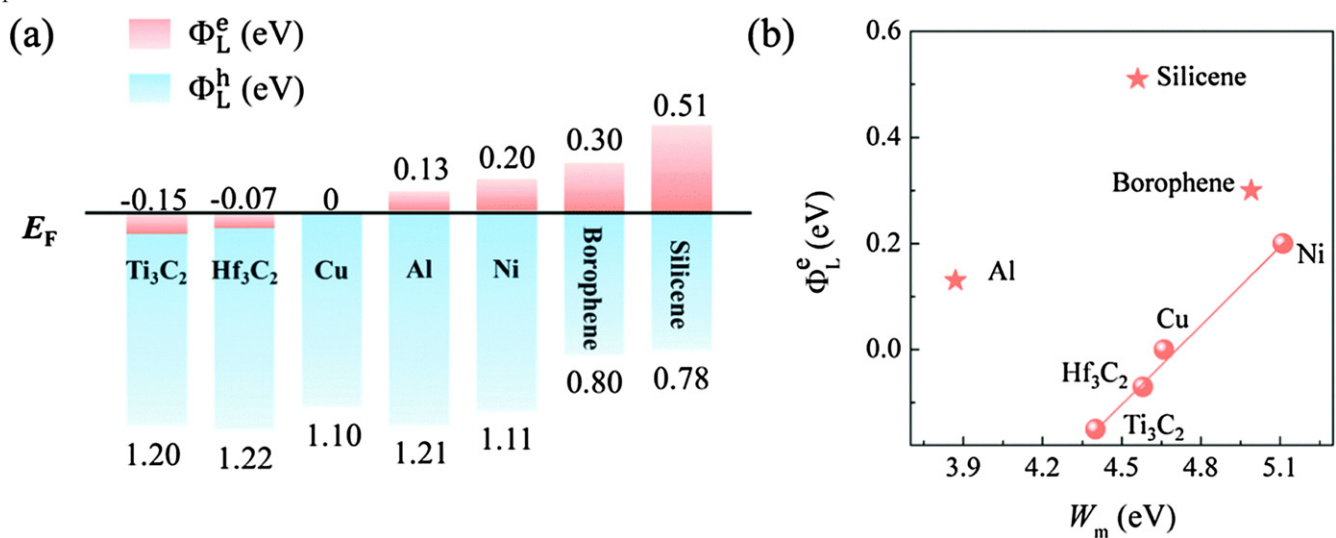


Figure 32. (a) Lateral SBHs for the ML ReS₂ FETs with metals. (b) The lateral electron SBHs as a function of the work function of metals. Reproduced from [191] with permission of The Royal Society of Chemistry.

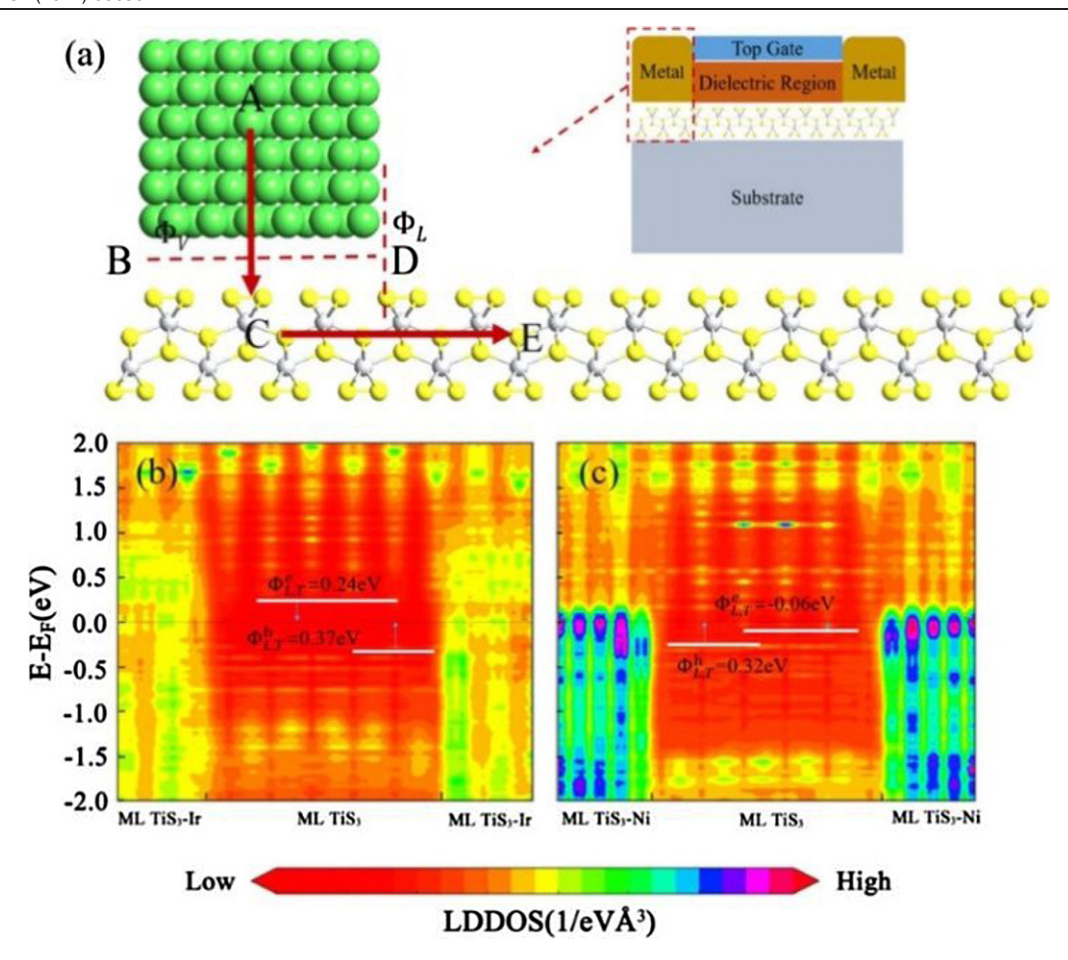


Figure 33. (a) Diagram of an ML TiS₃ transistors. LDDOS for ML TiS₃ transistors contacted with (b) Ir and (c) Ni electrodes. Reprinted with permission from [193]. Copyright (2019) American Chemical Society.

edge is flat using the QTS for WSe₂–Pt contact, and the lateral SBH without the SOC is equal to the vertical SBHs without SOC [185]. Therefore, the lateral SBH with the SOC also approximates the vertical SBH with the SOC. Therefore, the prediction of the p-type Ohmic contact between WSe₂ and Pt is suitable for both the vertical and lateral interfaces, and such a p-type Ohmic contact is confirmed in the experimental FET configuration [190].

The 2D titanium carbides are also proposed as promising electrode materials in WSe₂ devices [189]. The n-type lateral Schottky contact with an electron SBH of 0.4 eV is formed for the Ti_2C electrode, while the n-type Ohmic contact and p-type quasi-Ohmic contact (with a tiny SBH of 0.02 eV) are formed for Ti_2CF_2 and $Ti_2C(OH)_2$, respectively, as displayed in figures 31(c)–(e). TBs and vertical SBs are absent in all electrodes above. Therefore, the 2D Ti_2CY_2 (Y = F or OH) provides selections of electrode materials for both n-type and p-type low-resistance contacts in ML WSe₂ FETs.

4.1.6. Other TMCs-metal top contacts. Among the large family of TMCs, Mo- and W-based dichalcogenides are the most studied materials for their potential applications in electronics and optoelectronics. Nonetheless, many other TMC materials, which may have the same potential, are far unexplored. The scheme of BSC and QTS can also be applied to

study the SBH in FETs based on other TMCs. Zhao *et al* investigated the contact properties of the ML ReS₂ with silicene, borophene, Al, Ni, and Cu metals, Ti₃C₂, and Hf₃C₂ MXenes [191]. Freestanding ML ReS₂ possesses a direct bandgap of 1.45 eV [191]. In the vertical direction, ML ReS₂ forms n-type Schottky contacts and relatively large TB with silicene and borophene, indicating weak interactions. There is no vertical SBH in the other five considered heterostructures due to the metallization of the ML ReS₂. The lateral SBH is determined using the *ab initio* QTS [191]. As shown in figure 32(a), ML ReS₂ forms n-type lateral Schottky contacts with silicene, borophene, Al, and Ni. Lateral Ohmic contacts are formed for ML ReS₂ when contacted with Cu, Hf₃C₂, and Ti₃C₂ electrodes. Moreover, the pinning factor *S* of the ML ReS₂ is 0.49, as shown in figure 32(b).

TiS₃, one of the transition metal trichalcogenides, possesses highly anisotropic electronic properties. The few-layer TiS₃ nanoribbons FETs exhibit an n-type conduction behavior with on-off ratios as high as 10⁴ and mobilities up to 2.6 cm² V⁻¹ s⁻¹ [192]. Sun *et al* explored the interfacial properties of ML TiS₃ contacted with Au, Ag, Pd, Pt, Ir, and Ni electrodes by using the *ab initio* BSC and QTS [193]. In the vertical direction, there is no TB in all the considered ML TiS₃/metal systems. ML TiS₃ is metalized with vanishing

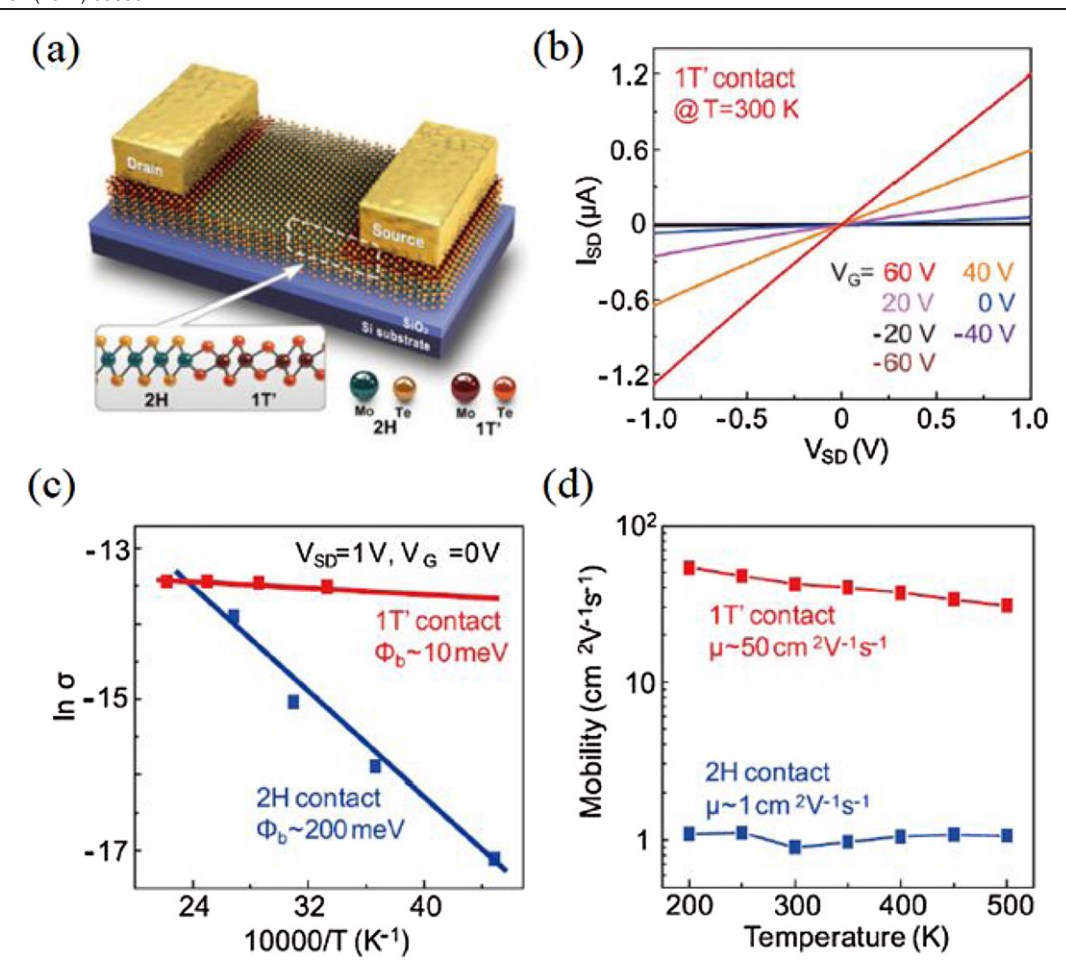


Figure 34. (a) Schematic diagrams of MoTe₂ transistors based on edge-contacted 1T'-2H phase. (b)-(d) Transport through phase homojunction structure in MoTe₂. (b) Output characteristics with gate voltage VG from -60 V to 60 V. (c) Conductance of the 1T'-2H MoTe₂ transistors. (d) The field-effect mobility of 1T'-2H MoTe₂ transistors changes with temperature. (a)-(d) From [177]. Reprinted with permission from AAAS.

vertical SBH when contacted with all these six metals, according to the BSC. In the lateral direction, Ir generates a p-type Schottky contact with the hole SBH of 0.37 eV while Ni realizes an Ohmic contact with ML TiS₃ from the *ab initio* QTS (figure 33).

4.1.7 TMD-metal edge contacts. Many efforts have been devoted to investigating the semiconducting 2H phase TMD transistors with edge-contacted metallic 1T'/1T phase TMD. These kinds of edge-contacted 1T'/1T-2H heterojunctions have been successfully fabricated in experiments by phase engineering, such as mechanical strain [194, 195], the organolithium chemical method [196–199], laser-irradiation [177], and electrostatic gating inducing [200]. Compared to the performance of MoS₂ and MoTe₂ transistors with a top-contacted bulk metal electrode, transistors based on their 1T'-2H phase edge-contact exhibit improved device performance with higher carrier mobility and lower contact resistance (figure 34) [177, 201, 202]. The observed lower contact resistance also means the lower and gate-tunable SBH in such a phase edge-contact [52, 201, 202].

Liu et al systematically studied the interfacial properties of SBFETs based on ML MX2 (MoS₂, MoTe₂, MoSe₂, WS₂, and

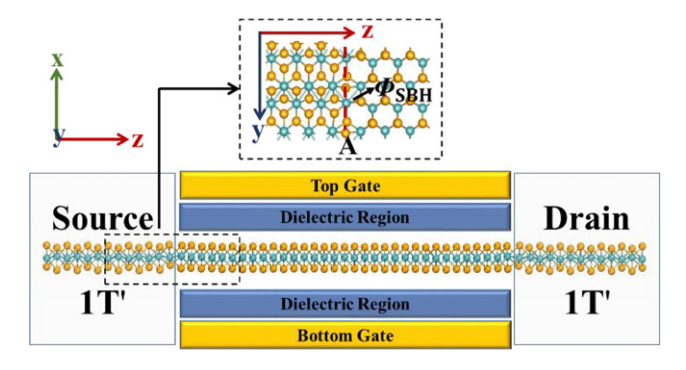


Figure 35. Schematic model of the ML MX_2 1T'-2H edge-contact transistor. Reproduced from [47] with permission of The Royal Society of Chemistry.

WSe₂) edge-contacted 1T'-2H phase using the QTS method [47]. In the two-probe model with double gates (figure 35), the 5 nm channel was built with semiconducting 2H MX₂, and the semi-infinite electrodes adopted the semi-metallic 1T' MX₂.

LDDOS (figure 36) shows specific edge states (not only the MIGS but also the hybridization states of the two phases) at the 1T'-2H edge-contacted interface. Such edge states distribute

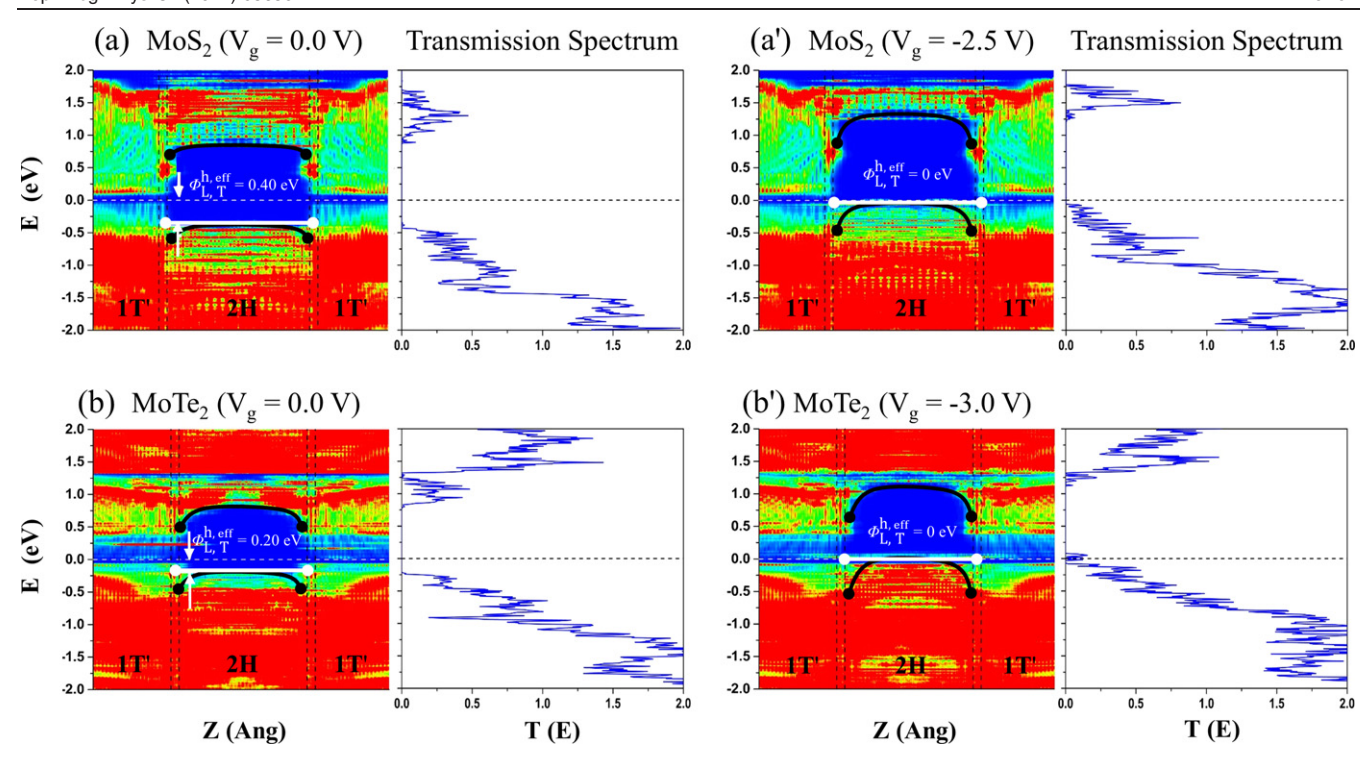


Figure 36. LDDOS and transmission spectra of the ML MoS₂ and MoTe₂ edge-contacted 1T'-2H transistors at $V_g=0$ ((a) and (b)) and $V_g\neq 0$ ((a') and (b')). Intrinsic VBM/CBM is represented by solid black curve. Reproduced from [47] with permission of The Royal Society of Chemistry.

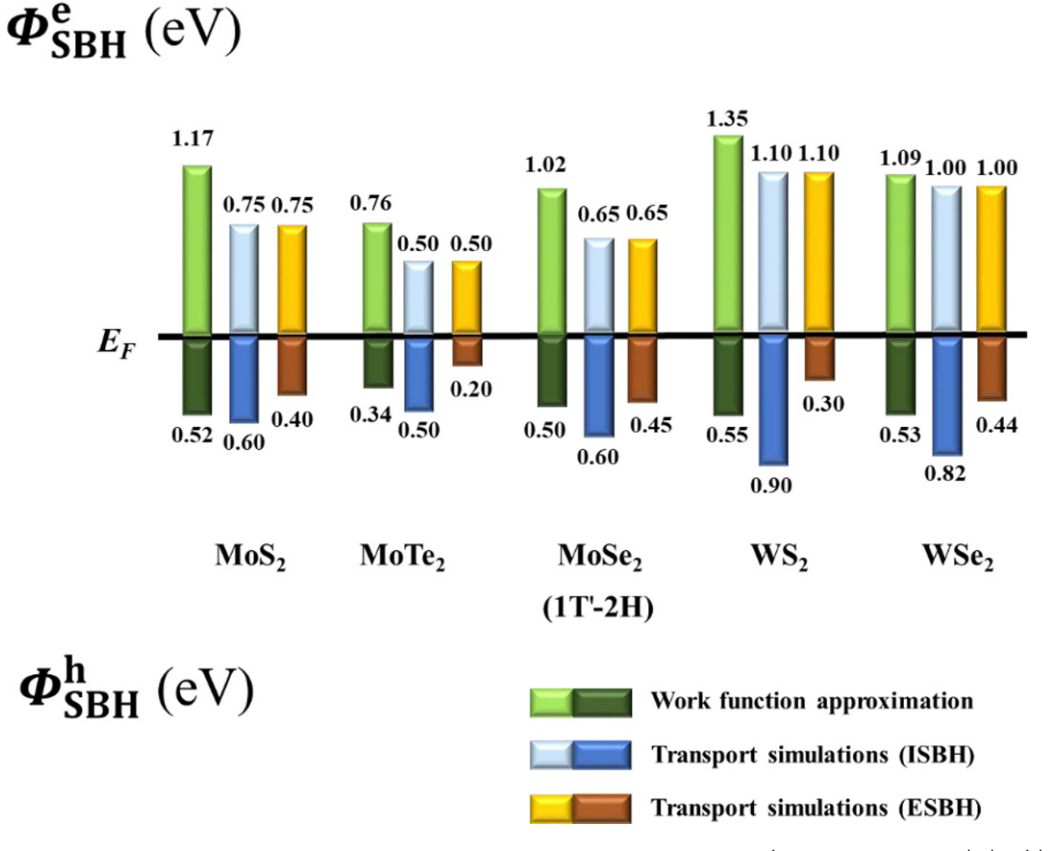


Figure 37. SBH of ML MX₂ 1T'-2H edge-contacted transistors obtained from the WFA (Φ_W^e/Φ_W^h) and the QTS ($\Phi_T^{e,intri}/\Phi_T^{h,intri}$, $\Phi_T^{e,eff}/\Phi_T^{h,eff}$). The blue bar and the yellow bar represent the ISBH and the ESBH, respectively. Reproduced from [47] with permission of The Royal Society of Chemistry.

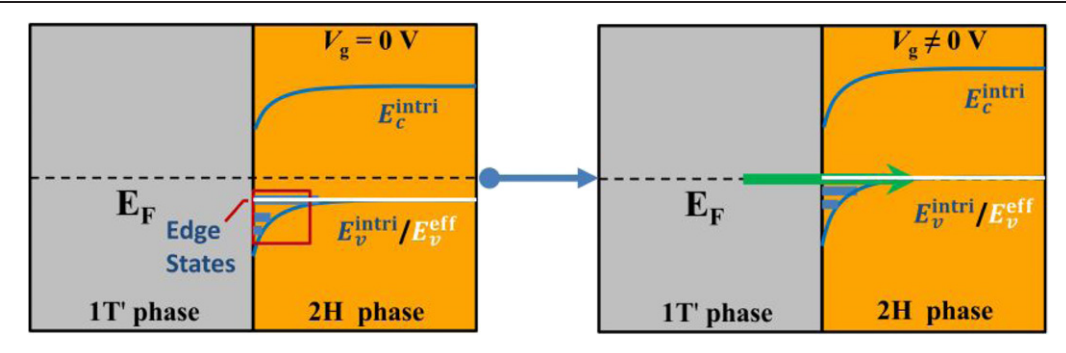


Figure 38. Left: schematic diagram of the band alignment of ML MX2 1T'-2H edge-contact heterojunction at $V_{\rm g}=0$ V. $E_{\rm F}$ is Fermi level (black dashed line). $E_{\rm v}^{\rm eff}$ is the effective VBM (white line). Right: illustration of band alignment of Ohmic contact at $V_{\rm g}\neq 0$. The green arrow points out the carrier injection pathway formed by deeply expanded edge states. Reproduced from [47] with permission of The Royal Society of Chemistry.

continuously and deep-enough to bridge the source/drain and channel, resulting in a lower hole ESBH extracted from the effective VBM (solid white line in figure 36) than intrinsic SBH (ISBH) extracted from the intrinsic VBM (solid black line in figure 35). [47]. Besides, the ESBH is tunable (see figures 36(a)–(a') and (b)–(b')), corresponding with experiment results that desirable Ohmic contact can be realized by tuning gate voltage [52, 202]. The comparison between SBHs from the WFA and SBHs from the QTS is shown in figure 37.

The widely-dispersed and deeply-expanded edge states originate from the strong coupling at the edge-contact interface. Besides, compared with bulk metal electrodes, low-dimensional electrodes shield the gate electric field less [82, 203, 204]. Therefore, the formation of new transport pathways by the gate-tunable edge states (a mixture of MIGS and hybridization state) and the improved gate control ability by adopting the 2D 1T' phase electrodes lead to a tunable ESBH and thus a better performance in the ML MX₂ 1T'-2H edge-contact (figure 38).

As for the low contact resistance in the fabricated edgecontacted 1T/1T'-2H MX₂ heterojunction, we also provide other points of view in addition to our opinion. The experimental works ascribe such a low contact resistance to the reduced physical separation between electrode and channel and the decreased TB [50], or the in-plane 1T/1T'-2H phase hybridization state that is still metallic with a high conductivity [205, 206], or the interfacial defects and adsorption from the technical process [50, 177]. For the ideal edge-contacted 1T/1T'-2H heterojunction, the theoretical works also give different viewpoints. Paz et al proposed that the Fermi level is pinned near the VBM, and the local upward bending of the VBM near the interface increases the DOS at the interface for hole injection [48]. Fan et al pointed out that the SB thickness can be changed by a gate voltage. If the thickness is smaller than the given value, the tunneling becomes very efficient (close to 1); in other words, the SBH is tunable by a gate voltage [49, 67]. Urquiza et al also found that the SBH can be tuned by a gate voltage [51]. All these theories come to the conclusion that a gate-tunable SB exists at the lateral 1T/1T'-2H interface (equivalent to the absence of the FLP), resulting in a more efficient carrier transmission and a lower contact resistance.

4.2. Group III-VI 2DSC

4.2.1. InSe/GaSe-metal top contacts. InSe (figure 39(a)), a new 2D III-VI semiconductor, has attracted much attention owing to its novel optical and electrical characters [106, 207-210]. ML InSe has an indirect bandgap of 1.52 eV, and the bandgap of InSe reduces as the thickness increases. BL, TL, and bulk InSe have a 0.97, 0.81, and 0.49 eV bandgap at the GGA-PBE level, respectively [211, 212]. The range of InSe bandgap is suitable for optical and electronics applications. The Hall mobility surpasses 10³ cm² V⁻¹ s⁻¹ in multilayer InSe FETs at room temperature [106, 213, 214]. These advantages make 2D InSe a promising next-generation channel material in electronics. The on-off ratio has achieved 10⁵ in the six-layer InSe transistors, but it becomes 10² in ML InSe transistor in Geim's experiment [106]. The big difference is due to the higher electrode-channel resistance in ML InSe transistor than that in a six-layer InSe transistor [106]. Besides, the sub-7 nm ML InSe MOSFETs achieve a remarkable device performance in the QTS, which makes the electrode-channel interface more important [54].

Several metals have been tested as the electrode of ML InSe based on first-principle BSC and QTS [215, 216]. The vertical Ohmic contacts are formed between ML InSe and Ag, Cu, In, Sc, Au, Cr, Pt, and Pd electrodes. Vertical quasi-Ohmic contact exists with a graphene electrode featured by a tiny electron SBH of 0.01 eV. The lateral n-type Schottky contacts are formed in the interface between ML InSe and Sc, Au, Cr, Pt, Pd, and graphene in QTS, with the electron SBHs of 0.25, 0.35, 0.41, 0.54, 0.61, and 0.55 eV, respectively (figure 40(a)). Moreover, n-type Ohmic contacts are formed in the lateral interface between Ag/Cu/In and ML InSe. The Schottky contact type in the simulations consists of the experimental data, including Ag, In, Au, Cr, and graphene as electrodes [106, 213, 217, 218]. A p-type Schottky contact is formed between ML O-Cr₂C and ML InSe due to a huge work function of ML O-Cr₂C. The hole SBHs are 0.68 and 0.76 eV in the vertical and lateral interface, respectively. The FLP exists with a pinning factor of 0.32 (figure 40(b)) in the lateral interface in the ML InSe FETs. The pinning factor is large owing to the large amount of MIGS, indicating a robust electrode-channel coupling in the ML InSe FETs [215]. Jin et al also investigated

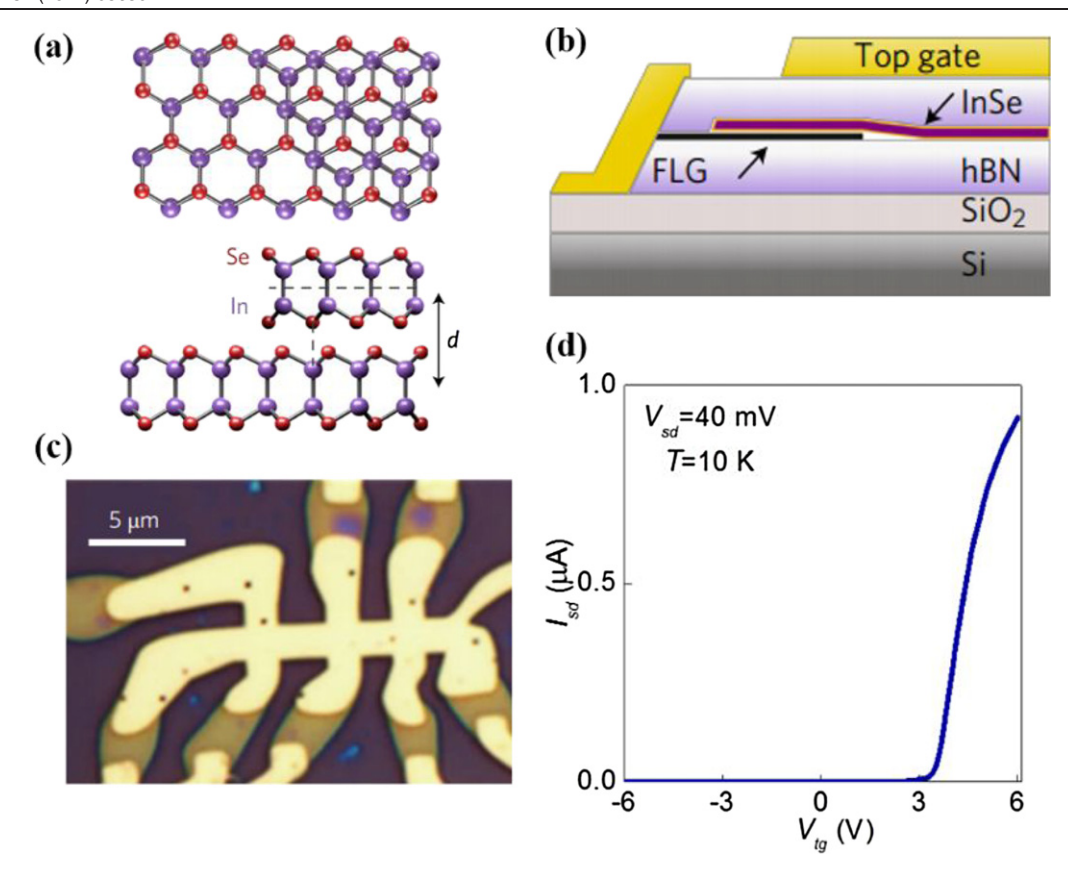


Figure 39. (a) Structure of the ML and BL InSe. Red and purple balls represent selenium and indium atoms, respectively. (b) Cross-sectional schematic of a 2D InSe FET. (c) Optical micrograph of an InSe device. The top gate is the bright central area that covers the encapsulated InSe. Peripheral Au contacts with FLG encapsulated by hBN, which is not covered by the top gate. The FLG region is dark yellow. (d) Transfer characteristic in 6L InSe FET using two-probe measurements. ($I_{\rm sd}$ is the current between the source and drain. $V_{\rm tg}$ is the voltage of the top gate. $V_{\rm sd}$ is the voltage between the source and drain.) Reprinted by permission from Springer Nature Customer Service Centre GmbH: Nature Nanotechnology [106] © 2017.

the interface between metals and ML InSe [216]. The electron SBHs calculated for Ag and Au electrodes are larger than those in the work of [215], as shown in figure 40(b). The reason may lie in that the hybrid functional (HSE06) is used in Jin's work and probably overestimates the transport gap and thereby the SBH [56, 219].

The vertical SBH is also revealed in the LDDOS when the ML InSe band structure can be identified in the electrode (Ag, Cu, In, ML graphene, and ML O-Cr₂C systems) [215]. The vertical hole/electron SBH is displayed as the energy difference between the Fermi level in the deep electrode part (far from the channel) and the VBM/CBM of ML InSe. A vertical n-type Ohmic contact is obtained from the LDDOS for Ag, Cu, and In, which is the same as the result in the BSC. However, for ML graphene, the LDDOS reveals a vertical Schottky contact while the band structure reveals a vertical quasi-Ohmic contact. The difference is because the VBM/CBM of ML InSe is downbent in the electrode region induced by the electrons transferring from the electrode to the channel. If the electrode region is long enough, the downbent will stop. An n-type quasi-Ohmic contact is expected in LDDOS, which is in agreement with the BSC. A vertical hole SBH (0.69 eV) is obtained in LDDOS for ML O-Cr₂C, which consists with the hole SBH (0.68 eV) obtained from the band structure [215].

As for BL InSe, electron SBs exist at the lateral interface between BL InSe and Sc, Au, Pt, and Pd with the electron SBHs 0.16, 0.20, 0.33, and 0.38 eV, respectively (figure 41) [220]. The FLP is 0.16, which is much smaller than ML InSe. Remarkably, n-type Ohmic contacts are formed between Ag/Cu and BL InSe.

GaSe shares similar electronic properties with InSe. ML GaSe has an indirect bandgap of 1.89 eV [221]. Zhao *et al* theoretically investigated the interfacial properties of ML GaSe contacted with various bulk metals and MXenes [221]. In the vertical direction, from the BSC, ML GaSe is completely metalized with zero SBH with V₂C, Mo₂C, Nb₂C, Cu, and Ni. Besides, Pt and Au form n-type vertical Schottky contact while V₂CO₂ and Nb₂CO₂ form p-type vertical Schottky contacts with ML GaSe. In the lateral direction, the lateral SBH values are shown in figure 42 obtained from the *ab initio* QTS. Mo₂C, Nb₂C, Cu, Ni, Pt, and Au generate n-type lateral Schottky contact as electrode materials in ML GaSe FET. Moreover, ML GaSe forms n-type Ohmic contacts with V₂CO₂ and P-type Ohmic contacts with V₂CO₂ and Nb₂CO₂. Pinning factor *S* of ML GaSe is 0.74, indicating a weak FLP (figure 42).

4.2.2. ln_2Se_3 -metal top contacts. Although 2D InSe performs well as a channel material for the FET, its ambient instability is a big issue, which restricts the further applications

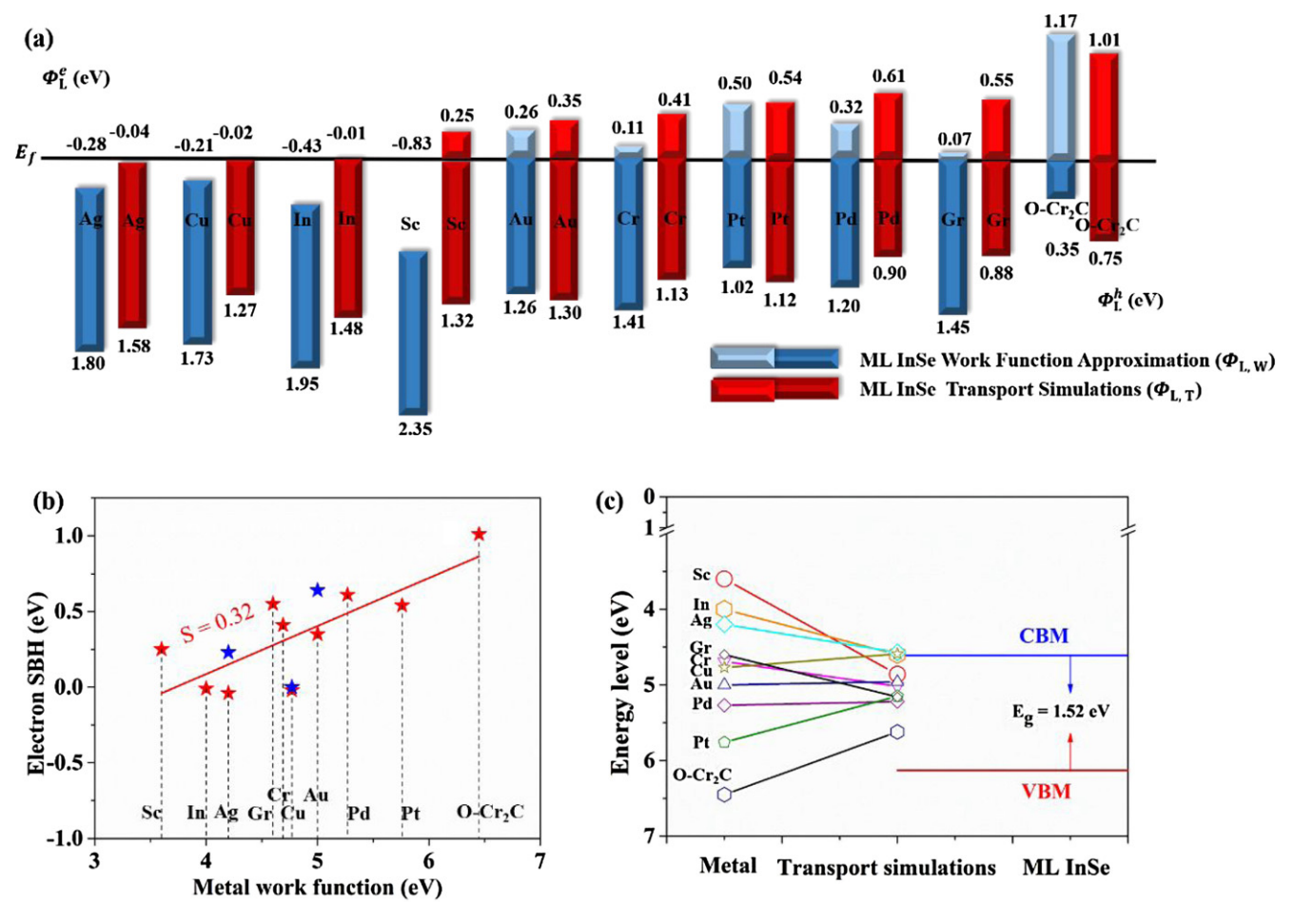


Figure 40. (a) Lateral electron SBHs obtain through WFA and QTS in the ML InSe FETs. (b) Lateral electron SBHs in the ML InSe FET from QTS versus the work function. *S* represents the pinning factor. The red stars (from [215]) and the blue stars (from [216]) represent the lateral SBHs of different metals. (c) Diagram of FLP in the ML InSe FETs. Reproduced from [215] with permission of The Royal Society of Chemistry.

[106, 217, 222]. By contrast, as one of the allotropies of 2D InSe, 2D In₂Se₃ (figure 43(a)) has been fabricated and possesses appropriate stability at ambient conditions [223–226]. ML In₂Se₃ has an indirect 0.82 eV bandgap based on the DFT calculations. A considerable electron (hole) carrier mobility of 920-960 (510-560) cm 2 V $^{-1}$ s $^{-1}$ is calculated for ML In₂Se₃ [227]. Ye et al successfully constructed 2D In₂Se₃-FETs (figure 43(b)) recently, which exhibit high performance with a high on-off ratio of over 10^8 at $V_{DS} = 1$ V, a large maximum current of 671 μ A μ m⁻¹, and the high electron mobility of 488 cm 2 V $^{-1}$ s $^{-1}$ (figure 43(c)) [228]. These unique properties make 2D In₂Se₃ a promising candidate as the channel material for the next-generation FETs. Furthermore, 2D In₂Se₃ is also a kind of 2D ferroelectric materials, which possesses the unique planar direction-dependent electrical properties [229]. The ferroelectric property potentially broadens the 2D In₂Se₃ based electronic device for wide applications, such as ferroelectric semiconductor FET with a large memory window [228].

Yang *et al* explored the contact properties between ML In₂Se₃ and Au, In, Sc, and Ag metal electrodes in a FET structure using the first principles BSC and QTS [230]. The planar-direction is defined by the built-in electric field of

ML In₂Se₃ due to its out-of-plane ferroelectric property. Both up and down planar-directions are considered [229]. As a result, all the ML In₂Se₃ band structures are hybridized in the contacting structures, indicating no vertical SBs at the metal-ML In₂Se₃ interfaces. In the lateral direction, the ab initio QTS was performed (as shown in figure 44). The planar direction-dependent interfacial properties were observed: n-type Schottky contacts occur in In, Sc electrodes with updirected ML In₂Se₃, but p-type Schottky contacts were formed at the interfaces between In, Sc electrodes and down-directed ML In₂Se₃. Furthermore, two metals could generate highly desirable Ohmic contacts: (1) Au electrode generated n-type Ohmic contact with the up-directed ML In₂Se₃. (2) Ag electrode generated n-type Ohmic contact with both two directions of ML In₂Se₃. The pinning factors are S = 0.04 and 0.05 for up and down directed ML In₂Se₃, respectively.

For the real FET devices, both n- and p-type contacts between semiconducting channel and metals are vital. Commonly, a semiconductor can only generate one kind of contact type with the same metal electrode. Changing electrodes always means extra costs. Yang *et al* demonstrated that contact types could be changed by the planar direction of ML In₂Se₃ with the same metal contact, which broadens the future

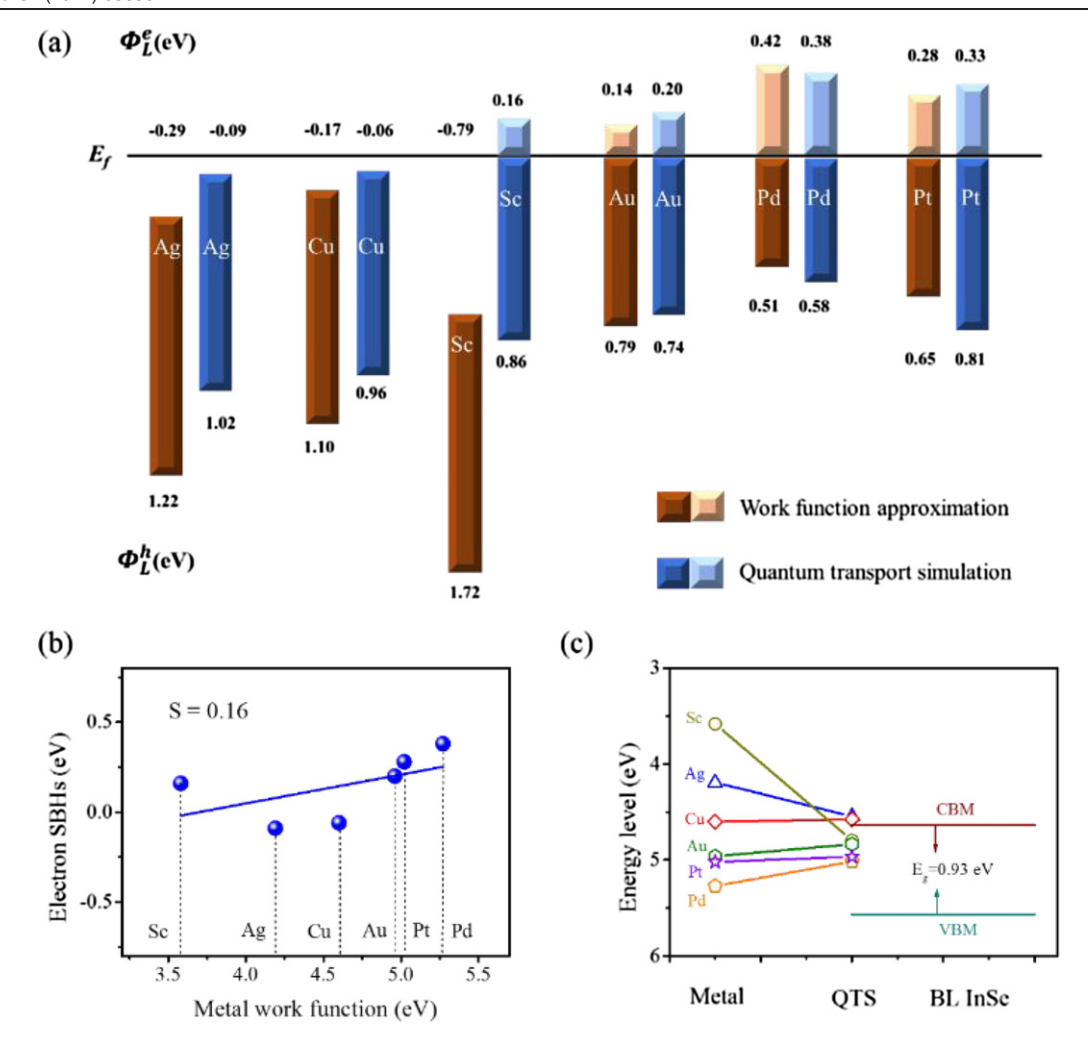


Figure 41. (a) Lateral electron SBHs obtain through WFA and QTS in the BL InSe FETs. (b) The comparison of the lateral electron SBHs between the QTS and the metal work function. *S* represents the pinning factor. (c) Diagram of the FLP effect in the BL InSe FETs. Reprinted with permission from [220]. Copyright (2019) American Chemical Society.

applications of In₂Se₃ material [230]. Besides, the Ohmic contacts found in ML In₂Se₃ make it a more competitive choice to be used as a channel material in next-generation transistors.

4.3. Group III-V 2DSC

Group III–V 2DSC is another semiconducting group material, such as GaN, having been widely researched for several years [231–236]. They are used in high-efficiency optoelectronics and electronic device, such as light-emitting diodes, laser diodes, and transistors [237–240]. J A Robinson group manufactured the 2D GaN via graphene encapsulation recently (figures 45(a) and (b)) [241]. Comparing with bulk material, the 2D GaN has quite promise applications in electronics and optoelectronic devices. It has two hexagonal structures after relaxation: a buckled and a planar one [231, 241]. The passivated buckled structure has a direct $E_{\rm g}=5.28~{\rm eV}$ (figures 45(c)–(f)) [241], and the planar GaN has a structure similar to graphene with an indirect $E_{\rm g}=2.17~{\rm eV}$ [242–244].

Guo *et al* studied the interfacial properties of the ML GaN FETs (with Pt, Au, Al, Ag, Ti, and Sc electrodes) [245]. In

the vertical interface, planar GaN is metalized, while the band structure is identifiable for buckled ML GaN. In the lateral interface, the planar GaN FET has n-type Schottky contact on the Ag electrode, p-type Schottky contacts on Ti, Au, and Al electrodes, and p-type/n-type Ohmic contact on the Pt/Sc electrode (figure 46(a)). In the vertical interface, the buckled GaN FETs have Ohmic contact (p-type) on Au/Pt electrodes and p-type Schottky contact on Ag, Al, Ti, and Sc electrodes. In the lateral direction, the buckled ML GaN FETs have Ohmic contact (p-type) on Au/Pt electrodes and Schottky contact (p-type) on Ag, Al, Ti, and Sc electrodes.

The ML GaN FETs have a moderate FLP. The calculated pinning factors of the ML GaN FETs (shown in figure 46(a)) are $S_L^e = 0.63$ (planar) and $S_L^h = 0.75$ (buckled), which are higher than those of other typical 2DSC FETs (arsenene ($S_L^e = 0.33$) [25], BlueP ($S_L^e = 0.42$) [94], BP ($S_L^e = 0.28$) [74], and and bismuthene ($S_L^e = 0.12$) [123]). Such a moderate FLP is attributed to the smaller amount of MIGS at the lateral interface [245]. Figure 46(b) shows the FLP effect of the GaN FETs, and the position of FLP of the ML buckled GaN FETs

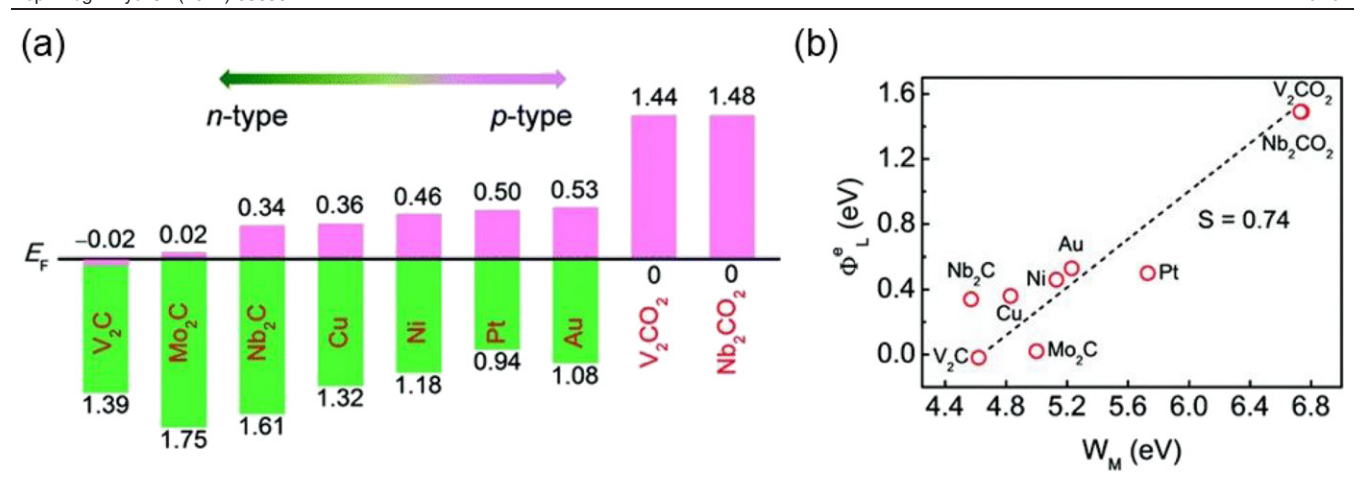


Figure 42. (a) Lateral SBH for the electron (red) and hole carriers (green) in the GaSe FETs. (b) Lateral electron SBH varies with the work function of metal electrodes. The black dashed line is a linear fitting of the data points. Reproduced from [221] with permission of The Royal Society of Chemistry.

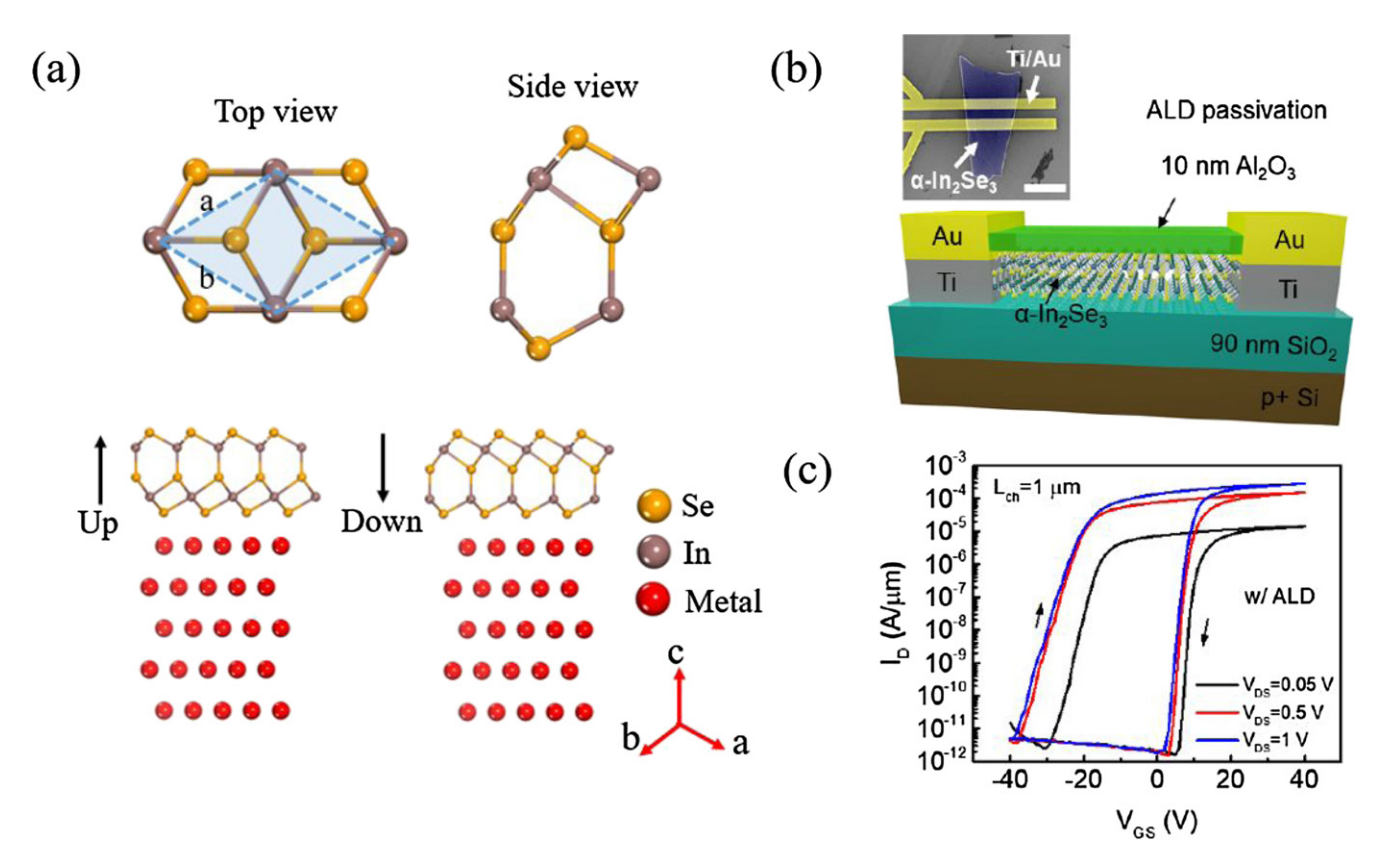


Figure 43. (a) Structure of freestanding ML In_2Se_3 and configurations of the ML In_2Se_3 —metal interfacial systems with up- and down-directed of In_2Se_3 . (b) Schematic diagram of the fabricated 2D In_2Se_3 -FET and the responding SEM image. (c) Transfer curve at room temperature of a representative 2D In_2Se_3 -FET. (a) [230] John Wiley & Sons © 2019 WILEY-VCH Verlag GmbH & Co. KGaA, Weinheim. (b), (c) Adapted by permission from Springer Nature Customer Service Centre GmbH: Nature Electronics [228] © 2019.

drops by about 2 eV because of the coupling at the interface [245].

4.4. Group IV-VI 2DSC

4.4.1. SnS-metal top contacts. Another well-studied family of vdW solids is the compounds with IV-VI elements, such as SnS₂, SnSe₂, SnS, and SnSe [14, 147]. A high on-off ratio

n-type FET by using 2D SnS was produced in 2016 [246]. Theoretically, FL SnS is predicted to have high carrier mobility with a sizeable bandgap [247]. The interfacial properties of ML SnS in contact with Ag, Al, Au, Pd, Cu, and Ni were explored in 2018 [248].

Based on the BSC, ML SnS undergoes a metallization after contact with metals, and SB is absent in the vertical direction.

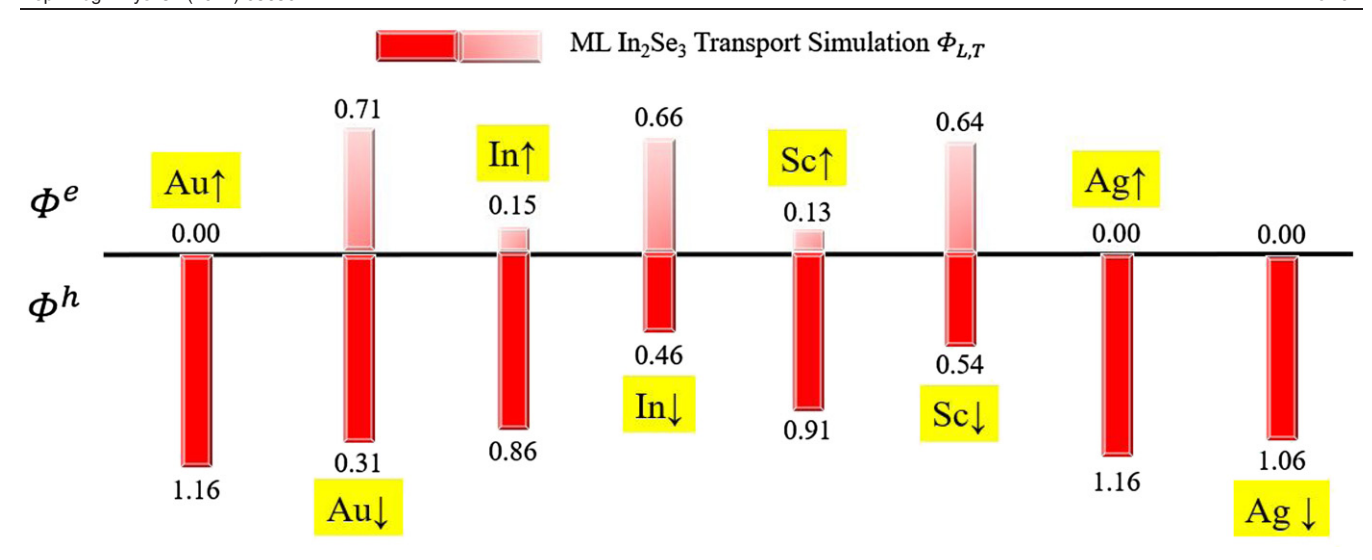


Figure 44. Lateral electron and hole SBHs of the Au/In/Sc/Ag contacting up- and down-directed ML In₂Se₃ (obtained from the QTS). [230] John Wiley & Sons © 2019 WILEY-VCH Verlag GmbH & Co. KGaA, Weinheim.

Lateral SBH is calculated by WFA and QTS, and the results are compared in figure 47. By using the QTS, n-type lateral Schottky contact is observed between ML SnS and Cu, Ni, and Ag with an electron SBH of 0.38, 0.43, and 0.62 eV, respectively. P-type lateral Schottky contact is observed between ML SnS and Pd, Au, and Al with a hole SBH of 0.44, 0.68, and 0.80 eV, respectively. The pinning factor is estimated to be 0.28 for electron and 0.17 for the hole [248].

These small pinning factors indicate a strong FLP effect, resulting in a pinned Fermi level around the center of the band gap of ML SnS and large lateral SBHs. These large lateral SBHs will degrade the device performance of the ML SnS FETs. By using vdW contact with 2D metal such as graphene or intercalating 2D material between ML SnS and bulk metal, a small SBH or even an Ohmic contact in the lateral direction is possible to obtain for ML SnS.

4.4.2. GeSe-metal top contacts. Germanium selenide (GeSe), as one of the IV-VI 2DSC family, is very stable in ambient air and easily fabricated [251, 252]. GeSe has a puckered structure (figure 48(a)) and anisotropic properties similar to isoelectronic phosphorene [253]. ML GeSe has band gaps (including direct and indirect) of 1.1–1.2 eV (figure 48(b)) overlapping with the solar spectrum [105, 251, 254, 255]. GeSe have been fabricated on SiO₂/Si substrates with the Au electrode to produce the photodetectors and solar cells [254, 256].

Guo *et al* used the *ab initio* BSC and QTS to calculate the interface properties of ML GeSe FETs (Ag, Pt, Au, Pd, Ti, Cu, graphene–Cu, and graphene electrodes) [250]. The devices have excellent Ohmic contacts in the vertical interface because of metalized ML GeSe. In the lateral interface, the puckered ML GeSe has anisotropic Schottky contacts. Along the zigzag direction (*a*-axis), the ML GeSe FETs have n-type Schottky contacts on Pt and Ag electrodes and p-type Schottky contacts on Pd, Ti, Cu, and Au electrodes (as shown in figure 49(a)). Along the armchair direction (*b*-axis), the ML GeSe FETs have n-type Schottky contacts on Cu and Ag electrodes and

p-type Schottky contacts on Au, Pd, Ti, and Pt electrodes. In the zigzag and armchair direction, the FLP factor is $S_a = -0.03$ and $S_b = 0.14$, respectively (figure 49), which is rather strong compared with other 2DSCs.

The vdW contact with 2D metal is an effective approach to low the SBH. By using graphene–Cu hybrid electrode, the ML GeSe FETs form quasi p-type Ohmic contact along zigzag (*a*-axis) direction. By using graphene electrode, the ML GeSe FETs form quasi p-type Ohmic contact along both the two directions (figure 49(b)). Hence, using graphene–Cu and graphene electrodes can make high-performance ML GeSe FETs with low contact resistance [250].

4.5. Oxychalcogenide 2DSC

Bi₂O₂Se is an emerging 2D material with a layered structure. Its tetragonal structure with I4/mmm space group (a =3.88 Å, c = 12.16 Å and Z = 2) is shown in figure 50(a) [257]. Each layer of Bi₂O₂Se has one oxide layer $[Bi₂O₂]^{2+}$ sandwiched by Se²⁻ square arrays through weak electrostatic interactions. Recently, large-area and the thin atomic layers Bi₂O₂Se with high quality have been synthesized on the mica substrate by the CVD method (figures 50b) and (c)) [257-259]. The experiment showed that the electron mobility of CVD-grown Bi₂O₂Se could reach \approx 450 cm² V⁻¹ s⁻¹, and the value can even reach 2000 $cm^2\ V^{-1}\ s^{-1}$ for thicker Bi₂O₂Se at around 300K [257, 258]. The bandgap of 2D Bi₂O₂Se is thickness-dependent [257]. At the LDA-MBJ level with the inclusion of SOC, ML Bi₂O₂Se's bandgap is 1.14 eV while the BL Bi₂O₂Se's bandgap shrinks to 0.18 eV. The band structures of Bi₂O₂Se are given in figure 50(d). The fabricated 2D Bi₂O₂Se samples exhibited robust stability in the air, moisture, or thermal conditions [257, 258, 260]. Remarkably, even down to ML, the surface roughness of Bi₂O₂Se remains almost the same when exposed to air for ~4 months, far superior to few-layer black phosphorus. Easy-accessibility to large production, high electron mobility, layer-dependent bandgap, and excellent environmental stability, all these satisfactory

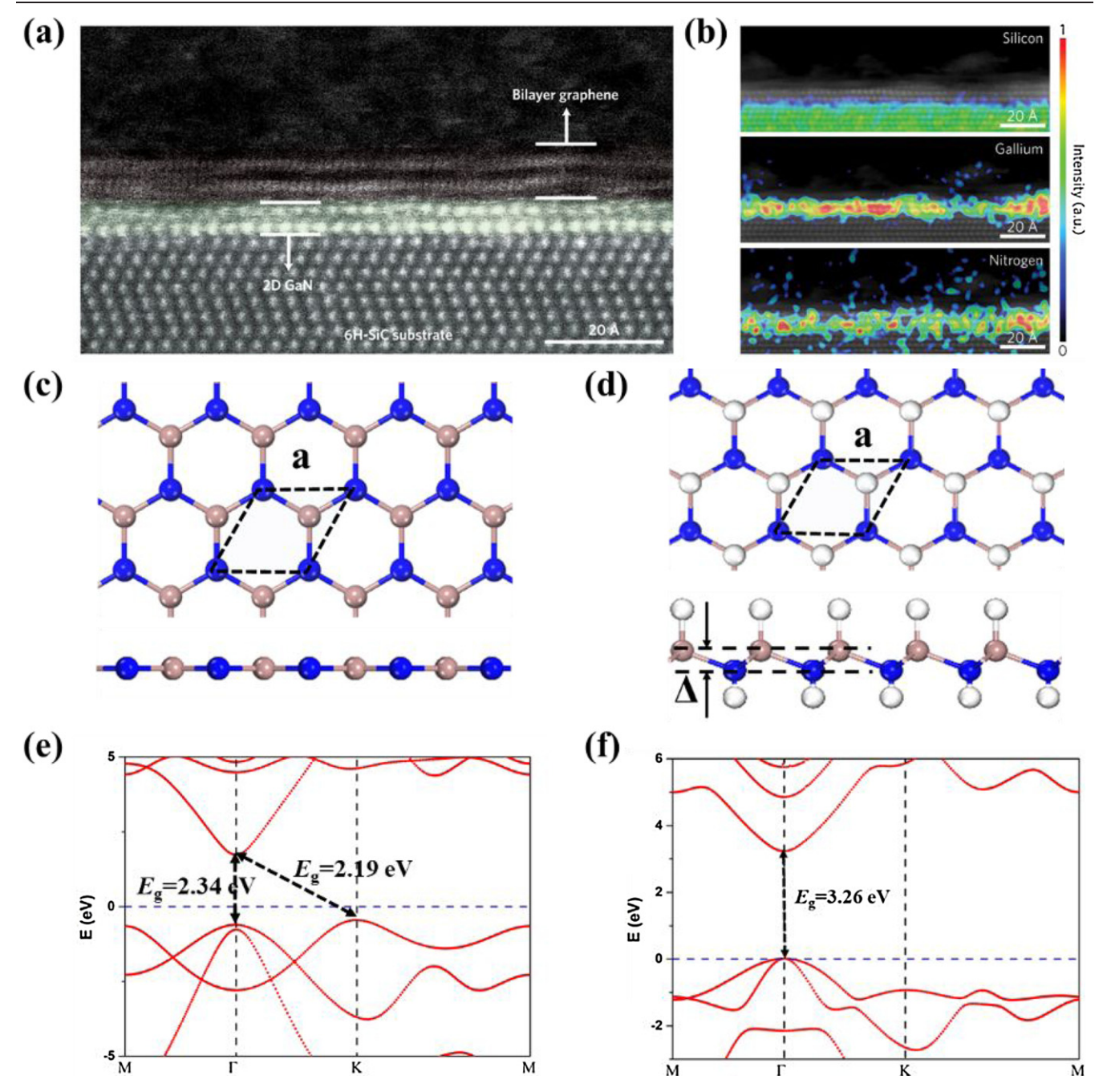


Figure 45. (a) Cross-section of 2D GaN by high-angle annular dark-field-STEM. (b) Elemental energy dispersive x-ray mapping of 2D GaN. The structure (c), (d) and the band structure (e), (f) of planar/buckled ML GaN. (a), (b) Reprinted by permission from Springer Nature Customer Service Centre GmbH: Nature Materials [241] © 2016. (c), (d) Reproduced from [245] with permission of The Royal Society of Chemistry.

features make Bi_2O_2Se become one of the most competitive 2D channel materials for next-generation FET [257, 258].

The fabricated BL Bi₂O₂Se SBFETs with Au/Pd electrodes already achieved Ohmic contact. The contact resistance for a 6.2 nm-thick Bi₂O₂Se FET is calculated to be 5 k Ω · μ m by analyzing its linear $I_{\rm ds}$ – $V_{\rm ds}$ curve. An ideal SS value (~65 mV/dec) and a large current on-off ratio (~10⁶) are also achieved at room temperature (figure 51) [257, 261]. For ML Bi₂O₂Se, reaching Ohmic contact is still a big issue [257].

Liu et al studied the SBH in ML Bi₂O₂Se FETs with Au, Pd, Pt, Ag, Sc, and Ti electrodes through the BSC and QTS methods [261]. For all the studied interfacial systems, band analysis reveals that the pristine ML Bi₂O₂Se undergoes metalization, featured by Bi₂O₂Se's bandgap disappearing after contact with metal. This illustrates that no vertical SBH at interface I. At interface II, ML Bi₂O₂Se–Au/Pd/Ag FETs witness n-type SBs (figure 52) [261]. However, the desirable lateral n-type Ohmic contacts observed at the ML Bi₂O₂Se–Pt/Sc/Ti FETs imply

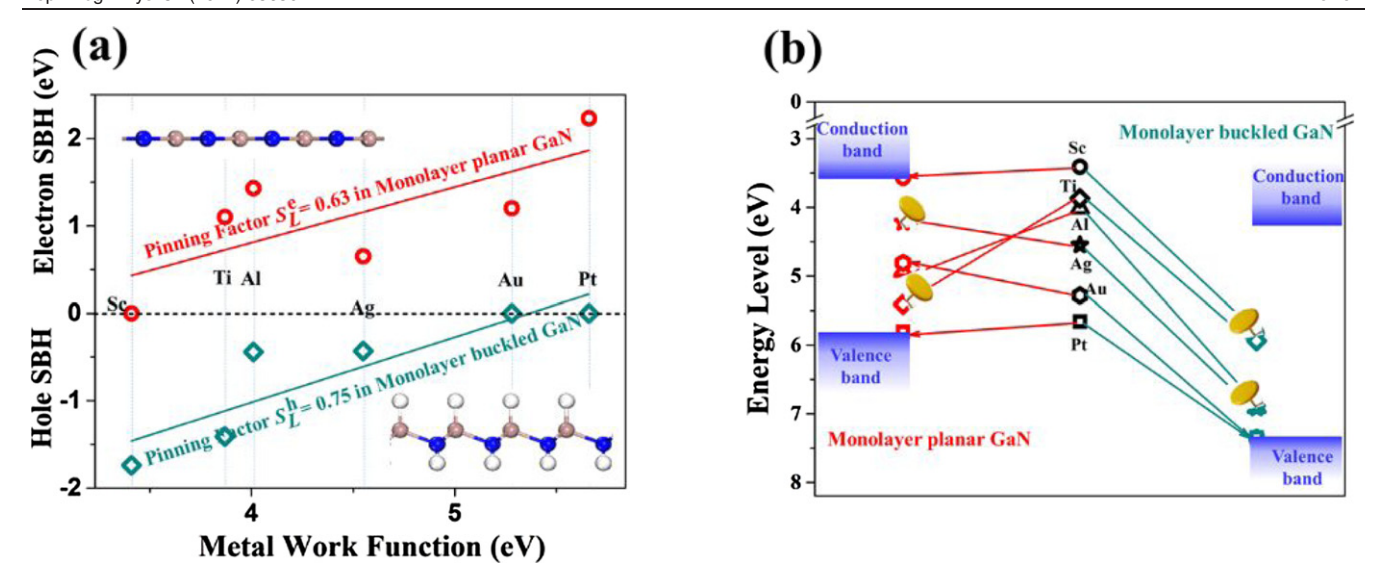


Figure 46. (a) Comparison of lateral contact properties of the ML GaN FETs with the metalwork function. S_L^e and S_L^h are the pinning factor of the planar and buckled ML GaN FETs from the Schottky-Mott rule. (b) Illustration of FLP in the ML GaN FETs. Reproduced from [245] with permission of The Royal Society of Chemistry.

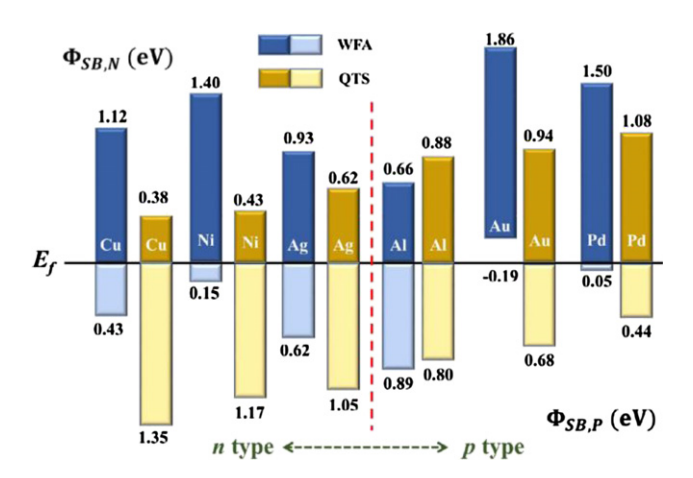


Figure 47. Comparison of the lateral SBH on the interface between metal and ML SnS between using the WFA and QTS. Reprinted with permission from [248]. Copyright (2018) American Chemical Society.

that such devices with low contact resistance are still worthy of expectation.

The strong coupling at the interface of the composite electrode and channel can induce MIGS, which can be used to explain the formation of 0.52 eV electron SBH within Ag-ML $\rm Bi_2O_2Se~SBFET$. The interfacial coupling can also modulate the Fermi level of the metal– $\rm Bi_2O_2Se$ electrode (The Fermi levels of Pt/Ti-ML $\rm Bi_2O_2Se$ are even lifted over the CBM (3.51 eV) of the channel so that the devices directly reach Ohmic contact. The average $\rm \overline{S}$ of FLP is 0.12, with the withingap $\rm S$ of $\rm -0.07$ and the beyond-gap $\rm S$ of 0.05, indicating a strong FLP at the lateral interface II [261].

As the simplest multilayer of Bi₂O₂Se, the experimental BL Bi₂O₂Se has realized desirable Ohmic contact with top-contacted Au/Pd electrodes. Xu *et al* carried out a systematic exploration of the contact properties in BL Bi₂O₂Se SBFETs with Au, Pd, Pt, Ag, Sc, and Ti electrodes [262]. Their

investigation shows Bi_2O_2Se-Pd SBFET forms n-type Ohmic contacts at its lateral interface, matching well with the experimental result [257, 258]. For the discrepancy that experimental BL Bi_2O_2Se transistor with Au/Pd electrode shows Ohmic contact while the ML Bi_2O_2Se cannot work well, the simulation demonstrates that the dramatic band gap increase from BL (0.43 eV) to ML limit (1.32 eV) is the main reason. Compared to its ML counterpart, BL Bi_2O_2Se prefers establishing (quasi) Ohmic contact with all the six investigated metals due to the relatively small band gap. Meanwhile, BL Bi_2O_2Se is believed to be a promising channel material for technology nodes under 5 nm in the future [262].

5. Summary and outlook

This review provides a comprehensive overview of the SB in 2DSC FETs from theory to experiment. In 2DSC FETs with vdW or weak chemical bonding top electrodes, the carriers transport first from the metal electrode to the underneath 2DSC in the vertical direction and then inject into the 2DSC channel region in the lateral direction. The SB may exist both in the vertical and lateral directions. If the energy band is flat from the contacted 2DSC to the channel 2DSC region at zero bias, which usually occurs in the vdW bonding type, the vertical and lateral SBHs are equal. In this case, the BSC based on an interfacial system is enough to provide the correct SBH. Such a calculation has taken into consideration the metal-2DSC coupling in the vertical direction. If there is band bending from the contacted 2DSC to the channel 2DSC, the vertical and lateral SBHs are no longer equal. The vertical and lateral SBHs should be determined from the spatially-resolved band edges generated from the ab initio QTS, which includes the coupling between the 2DSC underneath the metal and channel 2DSC.

In 2DSC FETs with robust chemical bonding top electrodes, the 2DSC underneath the metal electrode undergoes a metallization, and vertical SBH vanishes. Due to the existence

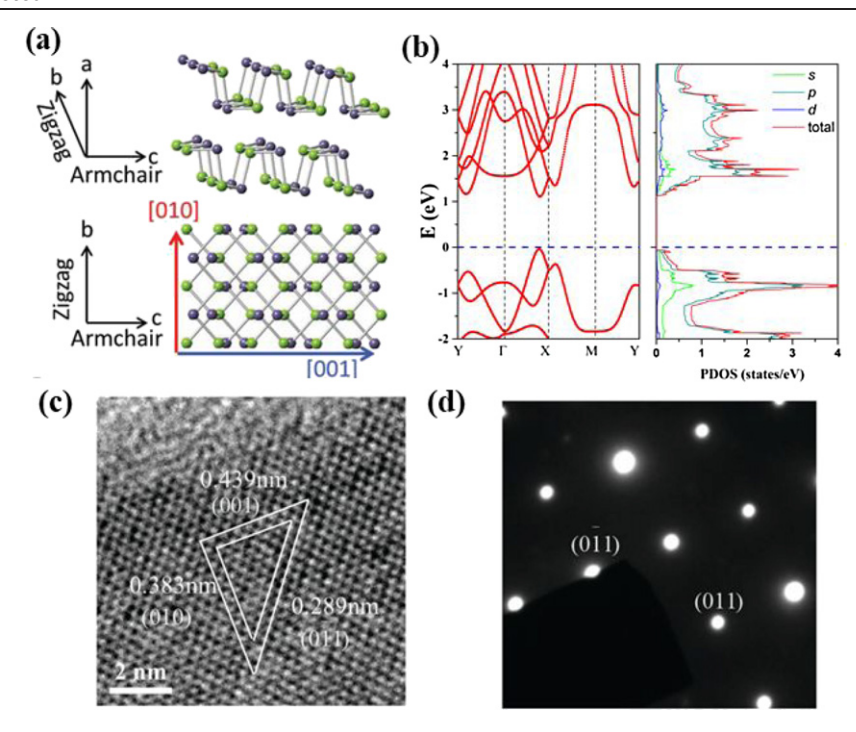


Figure 48. (a) Structure of GeSe. (b) Band structure and PDOS of ML GeSe. (c) HRTEM image of 2D GeSe nanosheet. (d) SAED pattern of GeSe. (a), (c) and (d) Reproduced from [249]. CC BY 4.0. (b) Reproduced from [250]. © IOP Publishing Ltd. All rights reserved.

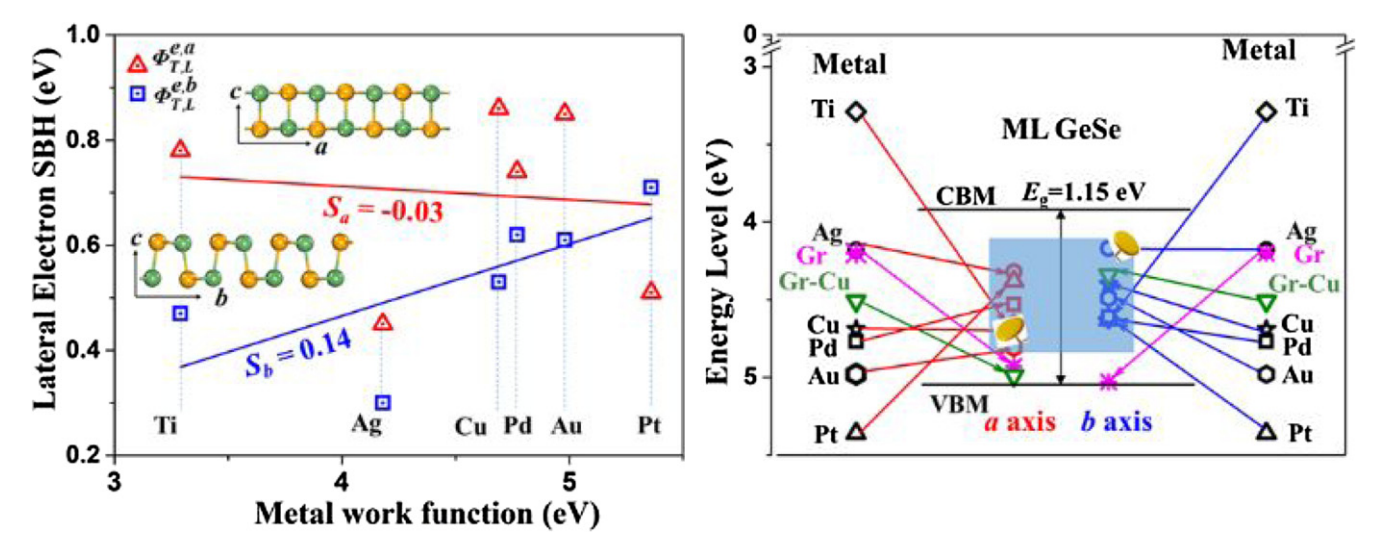


Figure 49. (a) Lateral electron SBH of the ML GeSe FETs as a function of the metals work function. S_a and S_b are the FLP factor of devices along the zigzag (a-axis) and armchair (b-axis) directions. (b) Illustration of FLP in the ML GeSe FETs. Reproduced from [250]. © IOP Publishing Ltd. All rights reserved.

of the FLP induced chiefly by the MIGS, the lateral SBH is not merely a difference between the work function of metalized 2DSC and the CBM/VBM of the channel 2DSC (namely WFA). It is imperative to fully consider the complex coupling between the metalized 2DSC and the channel 2DSC through the *ab initio* QTS. Actually, the lateral SBHs derived from the *ab initio* QTS are in significantly better agreement with the experimental results.

The theoretical pinning factor *S* with bulk metal contacts as a function of the bandgap from the *ab initio* BSC and QTS

is shown in figure 53. Except for ML GaN and ML GaSe, the Femi level of the 2DSC was strongly pinned with a pinning factor S < 0.5, due to the interface dipole, chemical bonding, and the most crucial factor of all, MIGS. A linear fit to these data gives $S = 0.30 E_{\rm g} - 0.14$. A smaller bandgap generally corresponds to a smaller S and thus a stronger FLP. Moreover, the theoretical S from the QTS is close to the experimental values for ML MoS₂ [31, 158]. Therefore, the *ab initio* QTS provides the most powerful theoretical tool to predict the SBH and pinning factor of a 2DSC FET.

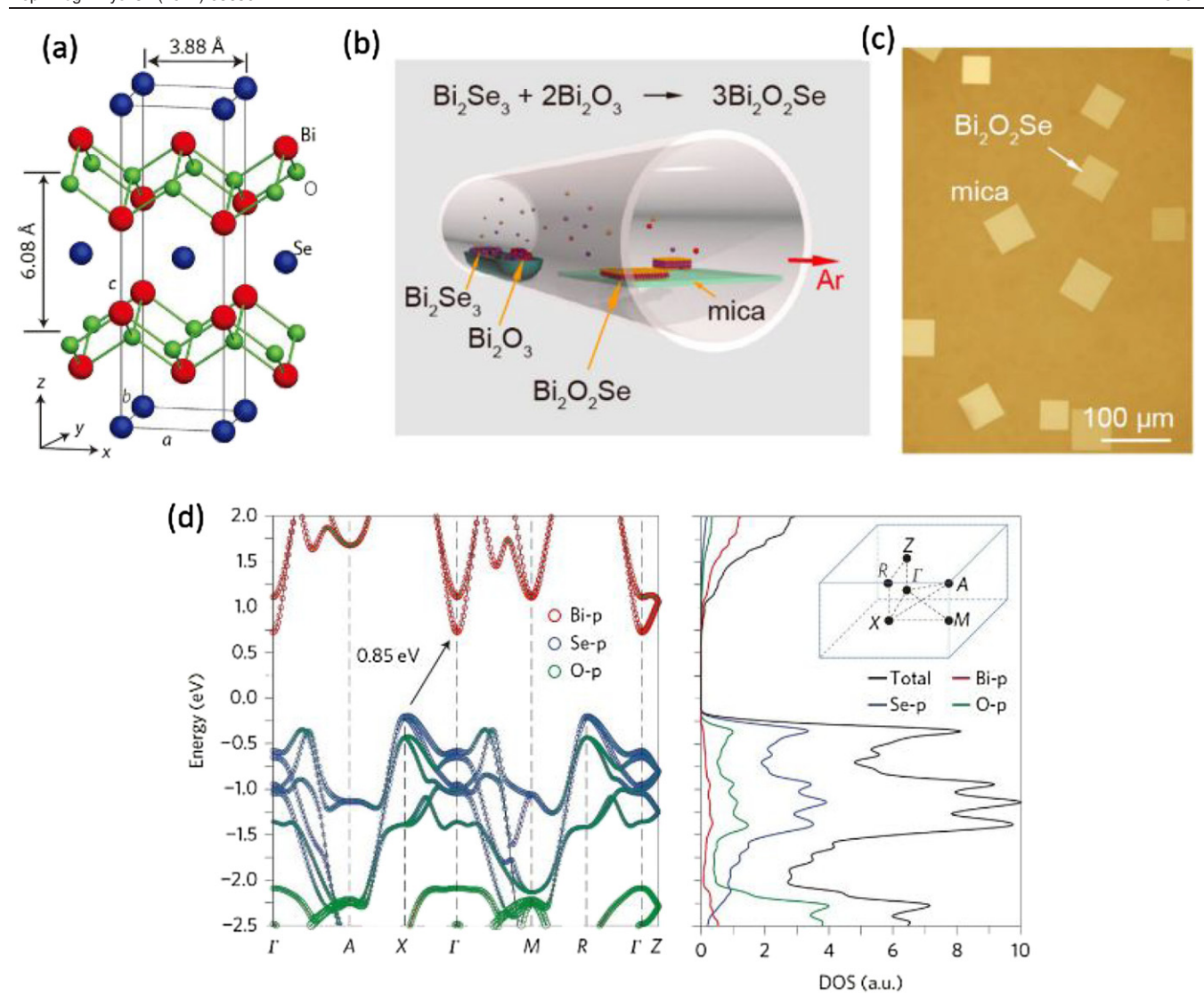


Figure 50. (a) Layered crystal structure of Bi_2O_2Se . (b) Bi_2O_2Se nanoplates synthesized through the CVD process. (c) Typical OM image of synthesized 2D Bi_2O_2Se crystals grown on mica. Reprinted with permission from [259]. Copyright (2017) American Chemical Society. (d) DFT-calculated band structures of bulk Bi_2O_2Se . Reprinted by permission from Springer Nature Customer Service Centre GmbH: Nature Nanotechnology [257] \otimes 2017.

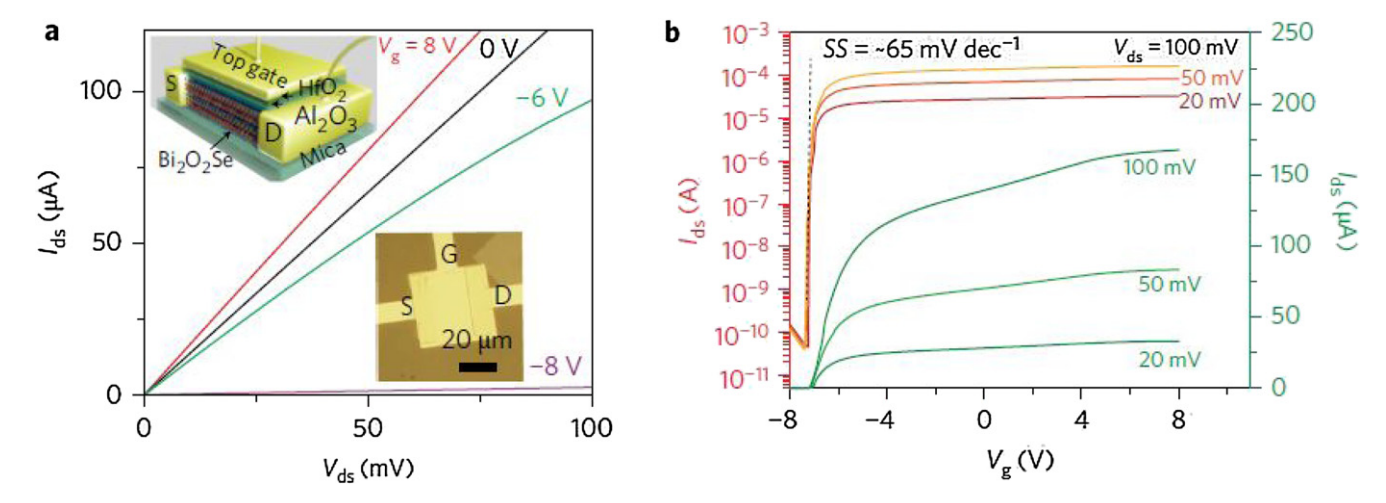


Figure 51. SBFET based on 2D Bi_2O_2Se . (a) Output curves of a 6.2 nm-thick and 21-um-long Bi_2O_2Se transistor. The insets are a schematic device model of a top-gated Bi_2O_2Se transistor (top row) and an optical microscopy image of this device on mica substrate with Al_2O_3 and HfO_2 as the dielectrics (bottom row). (b) Transfer characteristics of the 6.2 nm-thick 21-um-long Bi_2O_2Se transistor with a different bias. Reprinted by permission from Springer Nature Customer Service Centre GmbH: Nature Nanotechnology [257] \otimes 2017.

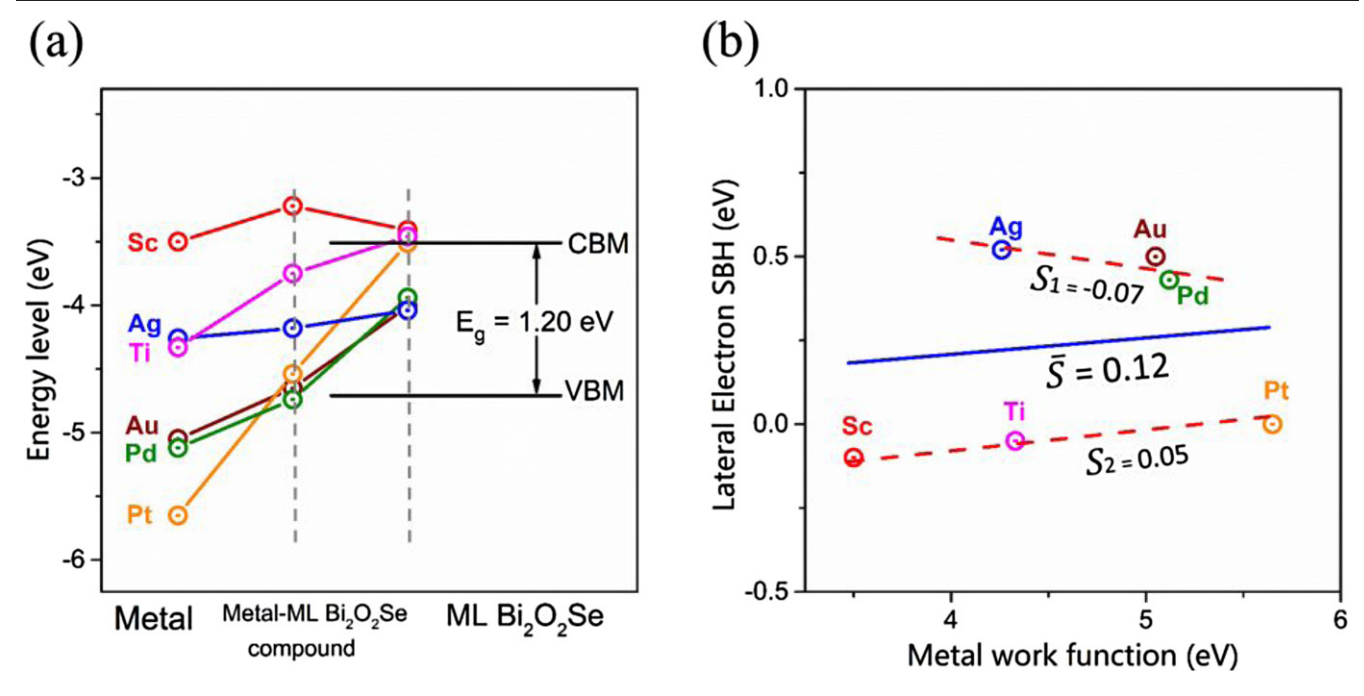


Figure 52. (a) Fermi level change during device construction. (b) Lateral electron SBH of the ML Bi₂O₂Se FETs changes with metal work function. The average \overline{S} of FLP is 0.12, with the within-gap S of -0.07 and the beyond-gap S of 0.05. [261] John Wiley & Sons. © 2019 WILEY-VCH Verlag GmbH & Co. KGaA, Weinheim.

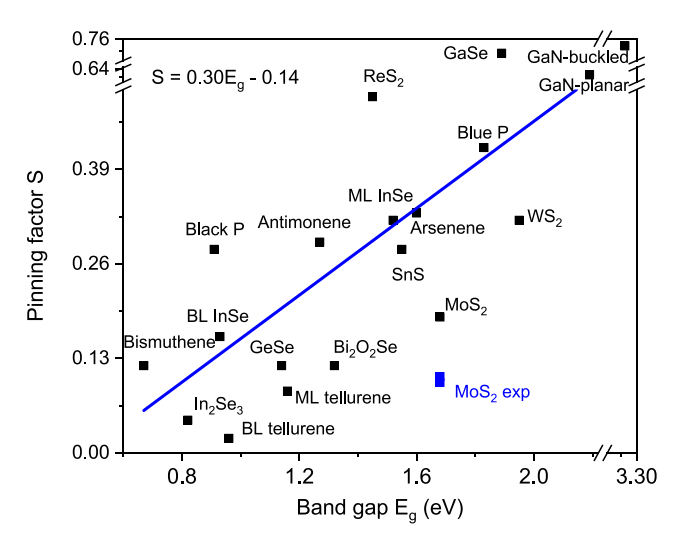


Figure 53. Pinning factor of 2DSC FETs versus the bandgap of 2DSCs. Black dots denote the theoretical values obtained from the BSC and QTS, and blue dots denote the experimental values [31, 158]. The data in this figure are for MLs unless explicitly stated. The pinning factor *S* is averaged over the two directions for ML In₂Se₃, ML GeSe, and ML tellurene.

vdW type of top metal electrode can be used to reduce the FLP, including 2D metal electrodes, 2D material-bulk metal hybrid electrode, and atomically flat bulk metals, which can create a clean interface with 2DSC with suppression of direct chemical bonding, defects, and chemical disorders. The damage-free top electrode integration has been experimentally demonstrated [31] and has shown great potential for high-performance electronics.

Although the edge contact electrode is not as common as the top one, it provides a solution to contact length scaling in 2DSC FETs [53]. The SBH in FETs with the electrode of edge contact geometry can also be determined by the QTS method. The TMDC MX₂ has semiconductor and metal phases, which can form trap-free lateral heterostructures with seamless bonding. The 1T'/1T-2H edge contacted MX₂ transistors generally reveal a lower SBH than the top-contacted ones according to the QTS method, which is consistent with the observed low contact resistance in experiments [52, 201, 202]. For 2DSCs without metallic phase, *in situ* edge contacts with various bulk metal could be fabricated using a directional ion beam [53]. Nonetheless, a systemic theoretical investigation is still lacking to understand better the carrier injection mechanism in 2DSC transistors with edge bulk metal electrodes.

The transistor model built for the QTS is generally defectless with ideal geometry. The intrinsic defects of the 2DSC channel have a severe impact on the SBH and FLP, which has been verified in the QTS study of MoS_2 transistors [164]. Therefore, defects should not be ignored in the modeling of 2DSC FETs, and their effect on the SBH should be evaluated in the future state-of-the-art computer-aided design of 2DSC FETs.

Acknowledgments

This work was supported by the National Natural Science Foundation of China (Nos. 11704406/11674005/91964101/11904409/12004307), the National Materials Genome Project of China (No. 2016YFB0700600), the Fundamental Research Funds for the Central Universities (No. 19CX05002A), China Postdoctoral Science Foundation (No. 2018M642721), Natural Science Basic Research Program of Shaanxi, China (Program No. 2019JM-355), Research Foundation of Education Bureau of Shaanxi Province, China (No.

19JS009), Open Fund of State Key Laboratory of Information Photonics and Optical Communications (Beijing University of Posts and Telecommunications), and the High Performance Computing Platform of Peking University.

Data availability statement

All data that support the findings of this study are included within the article (and any supplementary files).

ORCID iDs

Yangyang Wang https://orcid.org/0000-0003-3992-3796
Qiuhui Li https://orcid.org/0000-0002-4767-3523
Ruge Quhe https://orcid.org/0000-0001-8991-8640
Chen Yang https://orcid.org/0000-0001-9820-0833
Ying Guo https://orcid.org/0000-0002-3039-9425
Jinbo Yang https://orcid.org/0000-0003-3517-9701
Feng Pan https://orcid.org/0000-0002-8216-1339

References

- [1] ITRS 2015 The International Technology Roadmap for Semiconductors (ITRS) http://itrs2.net/itrs-reports.html
- [2] Cao W, Jiang J, Xie X, Pal A, Chu J H, Kang J and Banerjee K 2018 2-D layered materials for next-generation electronics: opportunities and challenges *IEEE Trans. Electron Devices* 65 4109–21
- [3] Bhimanapati G R et al 2015 Recent advances in twodimensional materials beyond graphene ACS Nano 9 11509–39
- [4] Das S, Robinson J A, Dubey M, Terrones H and Terrones M 2015 Beyond graphene: progress in novel two-dimensional materials and van der Waals solids *Annu. Rev. Mater. Res.* 45 1–27
- [5] Kim S J, Choi K, Lee B, Kim Y and Hong B H 2015 Materials for flexible, stretchable electronics: graphene and 2D materials Annu. Rev. Mater. Res. 45 63–84
- [6] Liu Y, Duan X, Huang Y and Duan X 2018 Two-dimensional transistors beyond graphene and TMDCs Chem. Soc. Rev. 47 6388–409
- [7] Schaibley J R et al 2016 Valleytronics in 2D materials Nat. Rev. Mater. 1 16055
- [8] Allain A, Kang J, Banerjee K and Kis A 2015 Electrical contacts to two-dimensional semiconductors *Nat. Mater.* 14 1195
- [9] Chuang H-J, Chamlagain B, Koehler M, Perera M M, Yan J, Mandrus D, Tománek D and Zhou Z 2016 Low-resistance 2D/2D ohmic contacts: a universal approach to highperformance WSe₂, MoS₂, and MoSe₂ transistors *Nano Lett.* 16 1896–902
- [10] Zhang X, Shao Z, Zhang X, He Y and Jie J 2016 Surface charge transfer doping of low-dimensional nanostructures toward high-performance nanodevices Adv. Mater. 28 10409–42
- [11] Kiriya D, Tosun M, Zhao P, Kang J S and Javey A 2014 Airstable surface charge transfer doping of MoS₂ by benzyl viologen J. Am. Chem. Soc. 136 7853-6
- [12] Xiang D et al 2015 Surface transfer doping induced effective modulation on ambipolar characteristics of few-layer black phosphorus Nat. Commun. 6 6485

- [13] Kang J et al 2014 Computational study of metal contacts to monolayer transition-metal dichalcogenide semiconductors Phys. Rev. X 4 031005
- [14] Radisavljevic B, Radenovic A, Brivio J, Giacometti V and Kis A 2011 Single-layer MoS₂ transistors *Nat. Nanotech*nol. 6 147–50
- [15] Liu W, Kang J, Sarkar D, Khatami Y, Jena D and Banerjee K 2013 Role of metal contacts in designing high-performance monolayer N-type WSe₂ field effect transistors *Nano Lett.* 13 1983–90
- [16] Liu W et al 2013 Proc. IEEE Int. Electron Devices Meeting (New York) 499–502
- [17] Tung R T 2014 The physics and chemistry of the Schottky barrier height Appl. Phys. Rev. 1 011304
- [18] Gong K et al 2014 Electrical contacts to monolayer black phosphorus: a first-principles investigation Phys. Rev. B 90 125441
- [19] Popov I et al 2012 Designing electrical contacts to MoS₂ monolayers: a computational study Phys. Rev. Lett. 108 156802
- [20] Tung R T 2001 formation of an electric dipole at metal-semiconductor interfaces Phys. Rev. B 64 205310
- [21] Tung R T 2000 Chemical bonding and Fermi level pinning at metal-semiconductor interfaces *Phys. Rev. Lett.* 84 6078–81
- [22] Gong C et al 2013 Metal contacts on physical vapor deposited monolayer MoS₂ ACS Nano 7 11350-7
- [23] Saidi W A 2014 Influence of strain and metal thickness on metal–MoS₂ contacts J. Chem. Phys. 141 094707
- [24] Guo Y, Liu D and Robertson J 2015 3D behavior of Schottky barriers of 2D transition-metal dichalcogenides ACS Appl. Mater. Interfaces 7 25709–15
- [25] Wang Y et al 2017 Electrical contacts in monolayer arsenene devices ACS Appl. Mater. Interfaces 9 29273–84
- [26] Qiu H et al 2013 Hopping transport through defect-induced localized states in molybdenum disulphide Nat. Commun. 4 2642
- [27] Lin J, Pantelides S T and Zhou W 2015 Vacancy-induced formation and growth of inversion domains in transition-metal dichalcogenide monolayer ACS Nano 9 5189–97
- [28] Liu Y, Stradins P and Wei S-H 2016 Air passivation of chalcogen vacancies in two-dimensional semiconductors *Angew*. *Chem.* 128 977–80
- [29] McDonnell S, Addou R, Buie C, Wallace R M and Hinkle C L 2014 Defect-dominated doping and contact resistance in MoS₂ ACS Nano 8 2880–8
- [30] Zan R, Ramasse Q M, Jalil R, Georgiou T, Bangert U and Novoselov K S 2013 Control of radiation damage in MoS₂ by graphene encapsulation ACS Nano 7 10167–74
- [31] Liu Y et al 2018 Approaching the Schottky–Mott limit in van der Waals metal–semiconductor junctions Nature 557 696–700
- [32] Bardeen J 1947 Surface states and rectification at a metal semiconductor contact *Phys. Rev.* 71 717–27
- [33] Cowley A M and Sze S M 1965 Surface states and barrier height of metal-semiconductor systems J. Appl. Phys. 36 3212–20
- [34] Arutchelvan G, Lockhart de la Rosa C J, Matagne P, Sutar S, Radu I, Huyghebaert C, De Gendt S and Heyns M 2017 From the metal to the channel: a study of carrier injection through the metal/2D MoS₂ interface *Nanoscale* 9 10869-79
- [35] Seo D and Chang J 2019 Doping-free arsenene heterostructure metal-oxide-semiconductor field effect transistors enabled by thickness modulated semiconductor to metal transition in arsenene Sci. Rep. 9 3988
- [36] Wang Y et al Carrier injection pathways in 2DSC FETs: the case of black phosphorene (unpublished)

- [37] Liu Y, Stradins P and Wei S-H 2016 Van der Waals metal-semiconductor junction: weak Fermi level pinning enables effective tuning of Schottky barrier Sci. Adv. 2 e1600069
- [38] Liu Y *et al* 2015 Toward barrier free contact to molybdenum disulfide using graphene electrodes *Nano Lett.* **15** 3030–4
- [39] Cui X et al 2015 Multi-terminal transport measurements of MoS₂ using a van der Waals heterostructure device Platform Nat. Nanotechnol. 10 534
- [40] Lee Y T, Choi K, Lee H S, Min S-W, Jeon P J, Hwang D K, Choi H J and Im S 2014 Graphene versus ohmic metal as source-drain electrode for MoS₂ nanosheet transistor channel Small 10 2356–61
- [41] Cui X et al 2017 Low-temperature ohmic contact to monolayer MoS₂ by van der Waals bonded Co/h-BN electrodes Nano Lett. 17 4781-6
- [42] Hill H M, Rigosi A F, Rim K T, Flynn G W and Heinz T F 2016 Band Alignment in MoS₂/WS₂ transition metal dichalcogenide heterostructures probed by scanning tunneling microscopy and spectroscopy *Nano Lett.* 16 4831–7
- [43] Farmanbar M and Brocks G 2016 Ohmic contacts to 2D semiconductors through van der Waals bonding Adv. Electron. Mater. 2 1500405
- [44] Jiang B et al 2018 Impact of thickness on contact issues for pinning effect in black phosphorus field-effect transistors Adv. Funct. Mater. 28 1801398
- [45] Wang L et al 2013 One-dimensional electrical contact to a twodimensional material Science 342 614
- [46] Khatami Y, Li H, Xu C and Banerjee K 2012 Metal-to-multilayer-graphene contact-part I: contact resistance modeling *IEEE Trans. Electron Devices* 59 2444–52
- [47] Liu S *et al* 2018 Gate-tunable interfacial properties of in-plane ML MX2 1T'-2H heterojunctions *J. Mater. Chem.* C **6** 5651-61
- [48] Paz W S and Palacios J J 2017 A theoretical study of the electrical contact between metallic and semiconducting phases in monolayer MoS₂ 2D Mater. 4 015014
- [49] Fan Z Q et al 2017 In-plane Schottky-barrier field-effect transistors based on 1T/2H heterojunctions of transition-metal dichalcogenides Phys. Rev. B 96 165402
- [50] Nourbakhsh A et al 2016 MoS₂ field-effect transistor with sub-10 nm channel length Nano Lett. 16 7798–806
- [51] Urquiza M L and Cartoixà X 2020 Schottky barriers, emission regimes and contact resistances in 2H-1T' MoS₂ lateral metal-semiconductor junctions from first-principles 2D Mater. 7 045030
- [52] Sung J H et al 2017 Coplanar semiconductor-metal circuitry defined on few-layer MoTe₂ via polymorphic heteroepitaxy Nat. Nanotechnol. 12 1064–70
- [53] Cheng Z, Yu Y, Singh S, Price K, Noyce S G, Lin Y-C, Cao L and Franklin A D 2019 Immunity to contact scaling in MoS₂ transistors using in situ edge contacts Nano Lett. 19 5077-85
- [54] Wang Y et al 2018 Many-body effect and device performance limit of monolayer InSe ACS Appl. Mater. Interfaces 10 23344-52
- [55] Wang Y, Huang P, Ye M, Quhe R, Pan Y, Zhang H, Zhong H, Shi J and Lu J 2017 Many-body effect, carrier mobility, and device performance of hexagonal arsenene and antimonene *Chem. Mater.* 29 2191–201
- [56] Liang Y and Yang L 2015 Carrier plasmon induced nonlinear band gap renormalization in two-dimensional semiconductors *Phys. Rev. Lett.* 114 063001
- [57] Datta S 1995 Electronic Transport in Mesoscopic Systems (Cambridge: Cambridge University Press)
- [58] Das S, Zhang W, Demarteau M, Hoffmann A, Dubey M and Roelofs A 2014 Tunable transport gap in phosphorene *Nano Lett.* 14 5733–9

- [59] Tran V et al 2014 Layer-controlled band gap and anisotropic excitons in few-layer black phosphorus Phys. Rev. B 89 235319
- [60] Wang X et al 2015 Highly anisotropic and robust excitons in monolayer black phosphorus Nat. Nanotechnol. 10 517–21
- [61] Cai Y et al 2014 Layer-dependent band alignment and work function of few-layer phosphorene Sci. Rep. 4 6677
- [62] Ugeda M M et al 2014 Giant bandgap renormalization and excitonic effects in a monolayer transition metal dichalcogenide semiconductor Nat. Mater. 13 1091
- [63] Berthod C et al 2003 Schottky barrier heights at polar metal/semiconductor interfaces Phys. Rev. B 68 085323
- [64] Zhong H *et al* 2016 Interfacial properties of monolayer and bilayer MoS₂ contacts with metals: beyond the energy band calculations *Sci. Rep.* **6** 21786
- [65] Das S, Chen H-Y, Penumatcha A V and Appenzeller J 2013 High performance multilayer MoS₂ transistors with scandium contacts *Nano Lett.* 13 100–5
- [66] Kaushik N, Nipane A, Basheer F, Dubey S, Grover S, Deshmukh M M and Lodha S 2014 Schottky barrier heights for Au and Pd contacts to MoS₂ Appl. Phys. Lett. 105 113505
- [67] Fan Z-Q, Jiang X-W, Chen J and Luo J-W 2018 Improving performances of in-plane transition-metal dichalcogenide Schottky barrier field-effect transistors ACS Appl. Mater. Interfaces 10 19271-7
- [68] Fei R and Yang L 2014 Strain-engineering the anisotropic electrical conductance of few-layer black phosphorus *Nano Lett.* 14 2884–9
- [69] Das S, Demarteau M and Roelofs A 2014 Ambipolar phosphorene field effect transistor ACS Nano 8 11730–8
- [70] Samuel Reich E 2014 Phosphorene excites materials scientists Nature 506 19
- [71] Wang L, Kutana A, Zou X and Yakobson B I 2015 Electro-mechanical anisotropy of phosphorene *Nanoscale* 7 9746–51
- [72] Qiao J et al 2014 High-mobility transport anisotropy and linear dichroism in few-layer black phosphorus Nat. Commun. 5 4475
- [73] Liu H, Neal A T, Zhu Z, Luo Z, Xu X, Tománek D and Ye P D 2014 Phosphorene: an unexplored 2D semiconductor with a high hole mobility ACS Nano 8 4033–41
- [74] Pan Y et al 2016 Monolayer phosphorene–metal contacts Chem. Mater. 28 2100–9
- [75] Yuan H and Li Z 2018 Interfacial properties of black phosphorus/transition metal carbide van der Waals heterostructures Front. Phys. 13 138103
- [76] Dathbun A, Kim Y, Kim S, Yoo Y, Kang M S, Lee C and Cho J H 2017 Large-area CVD-grown sub-2 V ReS₂ transistors and logic gates *Nano Lett.* 17 2999–3005
- [77] Leong W S, Luo X, Li Y, Khoo K H, Quek S Y and Thong J T L 2015 Low resistance metal contacts to MoS₂ devices with nickel-etched-graphene electrodes ACS Nano 9 869–77
- [78] Wang J *et al* 2016 High mobility MoS₂ transistor with low Schottky barrier contact by using atomic thick h-BN as a tunneling layer *Adv. Mater.* **28** 8302–8
- [79] Dankert A, Langouche L, Kamalakar M V and Dash S P 2014 High-performance molybdenum disulfide field-effect transistors with spin tunnel contacts ACS Nano 8 476–82
- [80] Avsar A, Vera-Marun I J, Tan J Y, Watanabe K, Taniguchi T, Castro Neto A H and Özyilmaz B 2015 Air-stable transport in graphene-contacted, fully encapsulated ultrathin black phosphorus-based field-effect transistors ACS Nano 9 4138–45
- [81] Kamalakar M V, Madhushankar B N, Dankert A and Dash S P 2015 Low Schottky barrier black phosphorus fieldeffect devices with ferromagnetic tunnel contacts Small 11 2209–16

- [82] Quhe R, Wang Y, Ye M, Zhang Q, Yang J, Lu P, Lei M and Lu J 2017 Black phosphorus transistors with van der Waals-type electrical contacts *Nanoscale* 9 14047–57
- [83] Pan Y et al 2017 Schottky barriers in bilayer phosphorene transistors ACS Appl. Mater. Interfaces 9 12694–705
- [84] Zhang X *et al* 2017 Three-layer phosphorene–metal interfaces *Nano Res.* **11** 707–21
- [85] Du Y, Liu H, Deng Y and Ye P D 2014 Device perspective for black phosphorus field-effect transistors: contact resistance, ambipolar behavior, and scaling ACS Nano 8 10035–42
- [86] Miao J, Zhang S, Cai L, Scherr M and Wang C 2015 Ultrashort channel length black phosphorus field-effect transistors ACS Nano 9 9236–43
- [87] Perello D J *et al* 2015 High-performance N-type black phosphorus transistors with type control via thickness and contact-metal engineering *Nat. Commun.* **6** 7809
- [88] Li L, Yu Y, Ye G J, Ge Q, Ou X, Wu H, Feng D, Chen X H and Zhang Y 2014 Black phosphorus field-effect transistors Nat. Nanotechnol. 9 372–7
- [89] Xia F et al 2014 Rediscovering black phosphorus as an anisotropic layered material for optoelectronics and electronics Nat. Commun. 5 4458
- [90] Zhang J L et al 2016 Epitaxial growth of single layer blue phosphorus: a new phase of two-dimensional phosphorus Nano Lett. 16 4903–8
- [91] Zhang W, Enriquez H, Tong Y, Bendounan A, Kara A, Seit-sonen A P, Mayne A J, Dujardin G and Oughaddou H 2018 Epitaxial synthesis of blue phosphorene Small 14 1804066
- [92] Guan J et al 2014 Phase coexistence and metal-insulator transition in few-layer phosphorene: a computational study Phys. Rev. Lett. 113 046804
- [93] Zhu Z and Tomanek D 2014 Semiconducting layered blue phosphorus: a computational study *Phys. Rev. Lett.* 112 176802
- [94] Li J et al 2018 Electrical contacts in monolayer blue phosphorene devices Nano Res. 11 1834–49
- [95] Kaur S et al 2016 Electronic properties of phosphorene/graphene heterostructures: effect of external electric field AIP Conf. Proc. 1731 050012
- [96] Kaur S, Kumar A, Srivastava S and Tankeshwar K 2017 Van der Waals heterostructures based on allotropes of phosphorene and MoSe₂ Phys. Chem. Chem. Phys. 19 22023–32
- [97] Zhu J, Zhang J and Hao Y 2016 Tunable Schottky barrier in blue phosphorus—graphene heterojunction with normal strain Jpn. J. Appl. Phys. 55 080306
- [98] Yang J, Quhe R, Feng S, Zhang Q, Lei M and Lu J 2017 Interfacial properties of borophene contacts with two-dimensional semiconductors *Phys. Chem. Chem. Phys.* 19 23982–9
- [99] Wang H, Si C, Zhou J and Sun Z 2017 Vanishing Schottky barriers in blue phosphorene/MXene heterojunctions *J. Phys. Chem.* C 121 25164–71
- [100] Kamal C and Ezawa M 2015 Arsenene: two-dimensional buckled and puckered honeycomb arsenic systems *Phys. Rev.* B 91 085423
- [101] Kou L, Ma Y, Tan X, Frauenheim T, Du A and Smith S 2015 Structural and electronic properties of layered arsenic and antimony arsenide J. Phys. Chem. C 119 6918–22
- [102] Zhong M, Xia Q, Pan L, Liu Y, Chen Y, Deng H-X, Li J and Wei Z 2018 Thickness-dependent carrier transport characteristics of a new 2D elemental semiconductor: black arsenic Adv. Funct. Mater. 28 1802581
- [103] Jamdagni P, Thakur A, Kumar A, Ahluwalia P K and Pandey R 2018 Two dimensional allotropes of arsenene with a wide range of high and anisotropic carrier mobility *Phys. Chem. Chem. Phys.* 20 29939–50
- [104] Zhang S, Yan Z, Li Y, Chen Z and Zeng H 2015 Atomically thin arsenene and antimonene: semimetal–semiconductor and indirect-direct band-gap transitions *Angew. Chem.*, *Int.* Ed. 54 3112–5

- [105] Zhang Z, Xie J, Yang D, Wang Y, Si M and Xue D 2015 Manifestation of unexpected semiconducting properties in few-layer orthorhombic arsenene Appl. Phys. Express 8 055201
- [106] Bandurin D A *et al* 2017 High electron mobility, quantum Hall effect and anomalous optical response in atomically thin InSe *Nat. Nanotechnol.* **12** 223–7
- [107] Koroteev Y M et al 2008 First-principles investigation of structural and electronic properties of ultrathin Bi films Phys. Rev. B 77 045428
- [108] Ares P, Aguilar-Galindo F, Rodríguez-San-Miguel D, Aldave D A, Díaz-Tendero S, Alcamí M, Martín F, Gómez-Herrero J and Zamora F 2016 Mechanical isolation of highly stable Antimonene under ambient conditions *Adv. Mater.* **28** 6332
- [109] Gibaja C *et al* 2016 Few-layer antimonene by liquid-phase exfoliation *Angew. Chem., Int. Ed.* **55** 14345–9
- [110] Wu X *et al* 2016 Epitaxial growth and air-stability of monolayer antimonene on PdTe₂ *Adv. Mater.* **29** 1605407
- [111] Shao Y et al 2018 Epitaxial growth of flat antimonene monolayer: a new honeycomb analogue of graphene Nano Lett. 18 2133
- [112] Zhang H et al 2019 Interfacial properties of monolayer antimonene devices Phys. Rev. Appl. 11 064001
- [113] Liu Z *et al* 2011 Stable nontrivial Z2 topology in ultrathin Bi (111) films: a first-principles study *Phys. Rev. Lett.* **107** 136805
- [114] Jnawali G *et al* 2012 Manipulation of electronic transport in the Bi(111) surface state *Phys. Rev. Lett.* **108** 266804
- [115] Yang F et al 2012 Spatial and energy distribution of topological edge states in single Bi(111) bilayer Phys. Rev. Lett. 109 016801
- [116] Reis F, Li G, Dudy L, Bauernfeind M, Glass S, Hanke W, Thomale R, Schäfer J and Claessen R 2017 Bismuthene on a SiC substrate: a candidate for a high-temperature quantum spin Hall material *Science* 357 287–90
- [117] Nagao T *et al* 2004 Nanofilm allotrope and phase transformation of ultrathin Bi film on Si(111)-7 × 7 *Phys. Rev. Lett.* **93** 105501
- [118] Walker E S et al 2016 Large-area dry transfer of singlecrystalline epitaxial bismuth thin films Nano Lett. 16 6931–8
- [119] Song Z *et al* 2014 Quantum spin Hall insulators and quantum valley Hall insulators of BiX/SbX (X = H, F, Cl and Br) monolayers with a record bulk band gap *NPG Asia Mater.* 6 e147
- [120] Luo W and Xiang H 2015 Room temperature quantum spin Hall insulators with a buckled square lattice *Nano Lett.* 15 3230-5
- [121] Hsu C-H, Huang Z-Q, Chuang F-C, Kuo C-C, Liu Y-T, Lin H and Bansil A 2015 The nontrivial electronic structure of Bi/Sb honeycombs on SiC(0001) New J. Phys. 17 025005
- [122] Ji W-x et al 2016 Giant gap quantum spin Hall effect and valley-polarized quantum anomalous Hall effect in cyanided bismuth bilayers New J. Phys. 18 083002
- [123] Guo Y et al 2017 Monolayer bismuthene-metal contacts: a theoretical study ACS Appl. Mater. Interfaces 9 23128-40
- [124] Qiao J, Pan Y, Yang F, Wang C, Chai Y and Ji W 2018 Few-layer tellurium: one-dimensional-like layered elementary semiconductor with striking physical properties *Sci. Bull.* 63 159–68
- [125] Chen J, Dai Y, Ma Y, Dai X, Ho W and Xie M 2017 Ultrathin β -tellurium layers grown on highly oriented pyrolytic graphite by molecular-beam epitaxy *Nanoscale* 9 15945–8
- [126] Huang X, Guan J, Lin Z, Liu B, Xing S, Wang W and Guo J 2017 Epitaxial growth and band structure of Te film on graphene *Nano Lett.* 17 4619–23

- [127] Wang Y et al 2018 Field-effect transistors made from solution-grown two-dimensional tellurene Nat. Electron. 1 228–36
- [128] Xiang Y, Gao S, Xu R-G, Wu W and Leng Y 2019 Phase transition in two-dimensional tellurene under mechanical strain modulation *Nano Energy* 58 202–10
- [129] Wu W, Qiu G, Wang Y, Wang R and Ye P 2018 Tellurene: its physical properties, scalable nanomanufacturing, and device applications *Chem. Soc. Rev.* 47 7203–12
- [130] Yan J et al 2018 Monolayer tellurene–metal contacts J. Mater. Chem. C 6 6153–63
- [131] Pang H *et al* 2019 Bilayer tellurene–metal interfaces *J. Semi-cond.* **40** 062003
- [132] Zhu Z et al 2017 Multivalency-driven formation of Te-based monolayer materials: a combined first-principles and experimental study Phys. Rev. Lett. 119 106101
- [133] Anzin V B, Eremets M I, Kosichkin Y V, Nadezhdinskii A I and Shirokov A M 1977 Measurement of the energy gap in tellurium under pressure *Phys. Status Solidi a* 42 385–90
- [134] Coker A, Lee T and Das T P 1980 Investigation of the electronic properties of tellurium-energy-band structure *Phys. Rev.* B 22 2968–75
- [135] Cherin P and Unger P 1967 Two-dimensional refinement of the crystal structure of tellurium *Acta Crystallogr.* **23** 670–1
- [136] Bao W et al 2013 High mobility ambipolar MoS₂ field-effect transistors: substrate and dielectric effects Appl. Phy. Lett. 102 042104
- [137] Kim S *et al* 2012 High-mobility and low-power thinfilm transistors based on multilayer MoS₂ crystals *Nat. Commun.* **3** 1011
- [138] Larentis S et al 2012 Field-effect transistors and intrinsic mobility in ultra-thin MoSe₂ layers Appl. Phys. Lett. 101 193
- [139] Chamlagain B et al 2014 Mobility improvement and temperature dependence in MoSe₂ field-effect transistors on parylene-c substrate ACS Nano 8 5079–88
- [140] Pradhan N R, Rhodes D, Xin Y, Memaran S, Bhaskaran L, Siddiq M, Hill S, Ajayan P M and Balicas L 2014 Ambipolar molybdenum diselenide field-effect transistors: field-effect and Hall mobilities Acs Nano 8 7923-9
- [141] Wang X *et al* 2014 Chemical vapor deposition growth of crystalline monolayer MoSe₂ ACS Nano **8** 5125–31
- [142] Zhou G et al 2018 High-mobility helical tellurium field-effect transistors enabled by transfer-free, low-temperature direct growth Adv. Mater. 30 1803109
- [143] Gang Q et al 2018 High-performance few-layer tellurium CMOS devices enabled by atomic layer deposited dielectric doping technique 76th Device Research Conference (DRC) 18071254
- [144] Amani M et al 2018 Solution-synthesized high-mobility tellurium nanoflakes for short-wave infrared photodetectors ACS Nano 12 7253–63
- [145] Qiu G, Huang S, Segovia M, Venuthurumilli P K, Wang Y, Wu W, Xu X and Ye P D 2019 Thermoelectric performance of 2D tellurium with accumulation contacts *Nano Lett.* **19** 1955–62
- [146] Kuc A et al 2011 Influence of quantum confinement on the electronic structure of the transition metal sulfide TS₂ Phys. Rev. B 83 245213
- [147] Podzorov V, Gershenson M E, Kloc C, Zeis R and Bucher E 2004 High-mobility field-effect transistors based on transition metal dichalcogenides Appl. Phys. Lett. 84 3301–3
- [148] Mak K F et al 2010 Atomically thin MoS₂: a new direct-gap semiconductor Phys. Rev. Lett. 105 136805
- [149] Baugher B W H, Churchill H O H, Yang Y and Jarillo-Herrero P 2013 Intrinsic electronic transport properties of

- high-quality monolayer and bilayer MoS_2 *Nano Lett.* **13** 4212-6
- [150] Bertolazzi S, Brivio J and Kis A 2011 Stretching and breaking of ultrathin MoS₂ ACS Nano 5 9703–9
- [151] Guo Y, Sun D, Ouyang B, Raja A, Song J, Heinz T F and Brus L E 2015 Probing the dynamics of the metallic-to-semiconducting structural phase transformation in MoS_2 Crystals Nano Lett. 15 5081–8
- [152] Cheng P, Sun K and Hu Y H 2016 Memristive behavior and ideal memristor of 1T phase MoS₂ nanosheets *Nano Lett*. 16 572-6
- [153] Wang L, Xu Z, Wang W and Bai X 2014 Atomic mechanism of dynamic electrochemical lithiation processes of MoS₂ nanosheets J. Am. Chem. Soc. 136 6693-7
- [154] Wang Q H, Kalantar-Zadeh K, Kis A, Coleman J N and Strano M S 2012 Electronics and optoelectronics of twodimensional transition metal dichalcogenides *Nat. Nan-otechnol.* 7 699–712
- [155] Qiu H et al 2012 Electrical characterization of back-gated bi-layer MoS₂ field-effect transistors and the effect of ambient on their performances Appl. Phys. Lett. 100 123104
- [156] Beal A R, Knights J C and Liang W Y 1972 Transmission spectra of some transition metal dichalcogenides. II. Group VIA: trigonal prismatic coordination J. Phys. C: Solid State Phys. 5 3540–51
- [157] Desai S B *et al* 2016 MoS₂ transistors with 1-nanometer gate lengths *Science* **354** 99–102
- [158] Kim C et al 2017 Fermi level pinning at electrical metal contacts of monolayer molybdenum dichalcogenides ACS Nano 11 1588–96
- [159] Fontana M et al 2013 Electron-hole transport and photovoltaic effect in gated MoS₂ Schottky junctions Sci. Rep. 3 1634
- [160] Das S, Prakash A, Salazar R and Appenzeller J 2014 Toward low-power electronics: tunneling phenomena in transition metal dichalcogenides ACS Nano 8 1681–9
- [161] Liu W et al 2013 High-performance few-layer-MoS₂ field-effect-transistor with record low contact-resistance IEEE Int. Electron Devices Meeting 19.14.11–4
- [162] Chen W, Santos E J G, Zhu W, Kaxiras E and Zhang Z 2013 Tuning the electronic and chemical properties of monolayer MoS₂ adsorbed on transition metal substrates *Nano Lett.* 13 509–14
- [163] Gong C, Colombo L, Wallace R M and Cho K 2014 The unusual mechanism of partial Fermi level pinning at metal–MoS₂ interfaces *Nano Lett.* **14** 1714–20
- [164] Pan Y et al 2019 Reexamination of the Schottky barrier heights in monolayer MoS₂ field-effect transistors ACS Appl. Nano Mater. 2 4717–26
- [165] Kang J, Liu W and Banerjee K 2014 High-performance MoS₂ transistors with low-resistance molybdenum contacts Appl. Phys. Lett. 104 093106
- [166] Hong J et al 2015 Exploring atomic defects in molybdenum disulphide monolayers Nat. Commun. 6 6293
- [167] Bampoulis P, van Bremen R, Yao Q, Poelsema B, Zandvliet H J W and Sotthewes K 2017 Defect dominated charge transport and Fermi level pinning in MoS₂/metal contacts ACS Appl. Mater. Interfaces 9 19278–86
- [168] Tongay S, Zhou J, Ataca C, Lo K, Matthews T S, Li J, Grossman J C and Wu J 2012 Thermally driven crossover from indirect toward direct bandgap in 2D semiconductors: MoSe₂ versus MoS₂ Nano Lett. 12 5576–80
- [169] Bougouma M, Batan A, Guel B, Segato T, Legma J B, Reniers F, Delplancke-Ogletree M-P, Buess-Herman C and Doneux T 2013 Growth and characterization of large, high quality MoSe₂ single crystals J. Cryst. Growth 363 122-7

- [170] Larentis S, Fallahazad B and Tutuc E 2012 Field-effect transistors and intrinsic mobility in ultra-thin MoSe₂ layers Appl. Phys. Lett. 101 223104
- [171] Çakır D and Peeters F M 2014 Dependence of the electronic and transport properties of metal–MoSe₂ interfaces on contact structures *Phys. Rev.* B 89 245403
- [172] Pan Y et al 2016 Interfacial properties of monolayer MoSe₂-metal contacts J. Phys. Chem. C 120 13063-70
- [173] Kang J, Tongay S, Zhou J, Li J and Wu J 2013 Band offsets and heterostructures of two-dimensional semiconductors Appl. Phys. Lett. 102 012111
- [174] Wu E, Xie Y, Zhang J, Zhang H, Hu X, Liu J, Zhou C and Zhang D 2019 Dynamically controllable polarity modulation of MoTe₂ field-effect transistors through ultraviolet light and electrostatic activation Sci. Adv. 5 eaav3430
- [175] Lin Y-F *et al* 2014 Ambipolar MoTe₂ transistors and their applications in logic circuits *Adv. Mater.* **26** 3263–9
- [176] Pradhan N R, Rhodes D, Feng S, Xin Y, Memaran S, Moon B-H, Terrones H, Terrones M and Balicas L 2014 Field-effect transistors based on few-layered α -MoTe₂ ACS Nano **8** 5911–20
- [177] Cho S *et al* 2015 Phase patterning for ohmic homojunction contact in MoTe₂ *Science* **349** 625–8
- [178] Liu X, Qu D, Ryu J, Ahmed F, Yang Z, Lee D and Yoo W J 2016 P-type polar transition of chemically doped multilayer MoS₂ transistor Adv. Mater. 28 2345–51
- [179] Liu L, Kumar S B, Ouyang Y and Guo J 2011 Performance limits of monolayer transition metal dichalcogenide transistors IEEE Trans. Electron Devices 58 3042–7
- [180] Tang H et al 2019 Schottky contact in monolayer WS₂ field-effect transistors Adv. Theory Simul. 2 1900001
- [181] Iqbal M W et al 2015 High-mobility and air-stable single-layer WS₂ field-effect transistors sandwiched between chemical vapor deposition-grown hexagonal BN films Sci. Rep. 5 10699
- [182] Sik Hwang W *et al* 2012 Transistors with chemically synthesized layered semiconductor WS₂ exhibiting 105 room temperature modulation and ambipolar behavior *Appl. Phys. Lett.* **101** 013107
- [183] Yuan H *et al* 2013 Zeeman-type spin splitting controlled by an electric field *Nat. Phys.* **9** 563–9
- [184] Xiao D et al 2012 Coupled spin and valley Physics in monolayers of MoS₂ and other group-VI dichalcogenides Phys. Rev. Lett. 108 196802
- [185] Wang Y et al 2016 Does p-type ohmic contact exist in WSe₂-metal interfaces? Nanoscale 8 1179-91
- [186] Lee C-H *et al* 2014 Atomically thin p-n junctions with van der Waals heterointerfaces *Nat. Nanotechnol.* **9** 676–81
- [187] Cheng R et al 2014 Electroluminescence and photocurrent generation from atomically sharp WSe₂/MoS₂ heterojunction p-n diodes Nano Lett. 14 5590-7
- [188] Fang H, Chuang S, Chang T C, Takei K, Takahashi T and Javey A 2012 High-performance single layered WSe₂ P-FETs with chemically doped contacts *Nano Lett.* 12 3788-92
- [189] Li Q, Yang J, Quhe R, Zhang Q, Xu L, Pan Y, Lei M and Lu J 2018 Ohmic contacts between monolayer WSe₂ and two-dimensional titanium carbides *Carbon* 135 125–33
- [190] Movva H C P, Rai A, Kang S, Kim K, Fallahazad B, Taniguchi T, Watanabe K, Tutuc E and Banerjee S K 2015 High-mobility holes in dual-gated WSe₂ field-effect transistors ACS Nano 9 10402–10
- [191] Gao N, Zhou S, Liu N, Bai Y and Zhao J 2018 Selecting electrode materials for monolayer ReS₂ with an ohmic contact *J. Mater. Chem.* C 6 6764–70
- [192] Island J O *et al* 2014 Ultrahigh photoresponse of few-layer TiS₃ nanoribbon transistors *Adv. Opt. Mater.* **2** 641–5

- [193] Sun R, Gu Y, Yang G, Wang J, Fang X, Lu N, Hua B and Yan X 2019 Theoretical study on the interfacial properties of monolayer TiS₃-metal contacts for electronic device applications J. Phys. Chem. C 123 7390-6
- [194] Duerloo K A N et al 2014 Structural phase transitions in twodimensional Mo- and W-dichalcogenide monolayers Nat. Commun. 5 4214
- [195] Lin X Q and Ni J 2017 Topological phase transition due to strain-controlled evolution of the inverted bands in 1T'-MX2 Phys. Rev. B 95 245436
- [196] Eda G, Fujita T, Yamaguchi H, Voiry D, Chen M and Chhowalla M 2012 Coherent atomic and electronic heterostructures of single-layer MoS₂ Acs Nano 6 7311-7
- [197] Gao G, Jiao Y, Ma F, Jiao Y, Waclawik E and Du A 2015 Charge mediated semiconducting-to-metallic phase transition in molybdenum disulfide monolayer and hydrogen evolution reaction in new 1T' phase J. Phys. Chem. C 119 13124–8
- [198] Kan M, Wang J Y, Li X W, Zhang S H, Li Y W, Kawazoe Y, Sun Q and Jena P 2014 Structures and phase transition of a MoS₂ monolayer J. Phys. Chem. C 118 1515–22
- [199] Kang Y et al 2014 Plasmonic hot electron induced structural phase transition in a MoS₂ monolayer Adv. Mater. 26 6467–71
- [200] Li Y et al 2016 Structural semiconductor-to-semimetal phase transition in two-dimensional materials induced by electrostatic gating Nat. Commun. 7 10671
- [201] Kappera R, Voiry D, Yalcin S E, Branch B, Gupta G, Mohite A D and Chhowalla M 2014 Phase-engineered low-resistance contacts for ultrathin MoS₂ transistors *Nat. Mater.* 13 1128–34
- [202] Katagiri Y et al 2016 Gate-tunable atomically thin lateral MoS₂ Schottky junction patterned by electron beam Nano Lett. 16 3788–94
- [203] Li H et al 2010 Functionalized metallic single-walled carbon nanotubes as a high-performance single-molecule organic field effect transistor: an ab initio study J. Phys. Chem. C 114 15816–22
- [204] Qi P, Javey A, Rolandi M, Wang Q, Yenilmez E and Dai H 2004 Miniature organic transistors with Carbon nanotubes as quasi-one-dimensional electrodes J. Am. Chem. Soc. 126 11774–5
- [205] Ke Q, Zhang X, Zang W, Elshahawy A M, Hu Y, He Q, Pennycook S J, Cai Y and Wang J 2019 Strong charge transfer at 2H–1T phase boundary of MoS₂ for superb high-performance energy storage Small 15 1900131
- [206] Jiang L, Zhang S, Kulinich S A, Song X, Zhu J, Wang X and Zeng H 2015 Optimizing hybridization of 1T and 2H phases in MoS₂ monolayers to improve capacitances of supercapacitors *Mater. Res. Lett.* 3 177–83
- [207] Tamalampudi S R, Lu Y-Y, Kumar R U, Sankar R, Liao C-D, Moorthy B K, Cheng C-H, Chou F C and Chen Y-T 2014 High performance and bendable few-layered InSe photodetectors with broad spectral response *Nano Lett.* 14 2800-6
- [208] Mudd G W et al 2013 Tuning the bandgap of exfoliated InSe nanosheets by quantum confinement Adv. Mater. 25 5714–8
- [209] Lei S et al 2014 Evolution of the electronic band structure and efficient photo-detection in atomic layers of InSe Acs Nano 8 1263–72
- [210] Lei S et al 2015 An atomically layered InSe avalanche photodetector Nano Lett. 15 3048–55
- [211] Guo Y and Robertson J 2017 Band structure, band offsets, substitutional doping, and Schottky barriers of bulk and monolayer InSe *Phys. Rev. Mater* 1 044004–9
- [212] Sun Y, Luo S, Zhao X-G, Biswas K, Li S-L and Zhang L 2018 InSe: a two-dimensional material with strong interlayer coupling *Nanoscale* 10 7991–8

- [213] Sucharitakul S, Goble N J, Kumar U R, Sankar R, Bogorad Z A, Chou F-C, Chen Y-T and Gao X P A 2015 Intrinsic electron mobility exceeding 103 cm² (V⁻¹ s⁻¹) in multilayer InSe FETs Nano Lett. 15 3815-9
- [214] Feng W, Zheng W, Cao W and Hu P 2014 Back gated multilayer InSe transistors with enhanced carrier mobilities via the suppression of carrier scattering from a dielectric interface *Adv. Mater.* **26** 6587–93
- [215] Shi B et al 2018 N-type ohmic contact and P-type Schottky contact of monolayer InSe transistors Phys. Chem. Chem. Phys. 20 24641–51
- [216] Jin H et al 2017 Ohmic contact in monolayer InSe-metal interface 2D Mater. 4 5116
- [217] Feng W, Zhou X, Tian W Q, Zheng W and Hu P 2015 Performance improvement of multilayer InSe transistors with optimized metal contacts *Phys. Chem. Chem. Phys.* 17 3653–8
- [218] Feng W, Zheng W, Chen X, Liu G and Hu P 2015 Gate modulation of threshold voltage instability in multilayer InSe field effect transistors ACS Appl. Mater. Interfaces 7 26691–5
- [219] Quhe R *et al* 2012 Tunable and sizable band gap in silicene by surface adsorption *Sci. Rep.* **2** 853
- [220] Xu L et al 2019 Computational study of ohmic contact at bilayer InSe-metal interfaces: implications for field-effect transistors ACS Appl. Nano Mater. 2 6898–908
- [221] Liu N, Zhou S, Gao N and Zhao J 2018 Tuning Schottky barriers for monolayer GaSe FETs by exploiting a weak Fermi level pinning effect *Phys. Chem. Chem. Phys.* 20 21732–8
- [222] Nan H, Guo S, Cai S, Chen Z, Zafar A, Zhang X, Gu X, Xiao S and Ni Z 2018 Producing air-stable InSe nanosheet through mild oxygen plasma treatment Semicond. Sci. Technol. 33 074002
- [223] Cui C et al 2018 Intercorrelated in-plane and out-of-plane ferroelectricity in ultrathin two-dimensional layered semiconductor In₂Se₃ Nano Lett. 18 1253–8
- [224] Xue F et al 2018 Multidirection piezoelectricity in mono- and multilayered hexagonal α-In₂Se₃ ACS Nano 12 4976–83
- [225] Feng W, Gao F, Hu Y, Dai M, Li H, Wang L and Hu P 2018 High-performance and flexible photodetectors based on chemical vapor deposition grown two-dimensional In₂Se₃ nanosheets *Nanotechnology* 29 445205
- [226] Feng W, Zheng W, Gao F, Chen X, Liu G, Hasan T, Cao W and Hu P 2016 Sensitive electronic-skin strain sensor array based on the patterned two-dimensional α-In₂Se₃ Chem. Mater. 28 4278–83
- [227] Zhao P, Ma Y, Lv X, Li M, Huang B and Dai Y 2018 Twodimensional III2-VI3 materials: promising photocatalysts for overall water splitting under infrared light spectrum *Nano Energy* 51 533-8
- [228] Si M et al 2019 A ferroelectric semiconductor field-effect transistor Nat. Electron. 2 580–6
- [229] Ding W et al 2017 Prediction of intrinsic two-dimensional ferroelectrics in In₂Se₃ and other III2-VI3 van der Waals materials Nat. Commun. 8 14956
- [230] Yang C et al 2020 Planar direction-dependent interfacial properties in monolayer In₂Se₃-metal contacts Phys. Status Solidi b 257 1900198
- [231] Singh A K et al 2014 Ab initio synthesis of single-layer III–V materials Phys. Rev. B 89 245431
- [232] Zhuang H L *et al* 2013 Computational discovery of single-layer III–V materials *Phys. Rev.* B **87** 165415
- [233] Dingle R, Sell D D, Stokowski S E and Ilegems M 1971 Absorption, reflectance, and luminescence of GaN epitaxial layers *Phys. Rev.* B 4 1211–8
- [234] Kim J C, Li X, Moore C J, Bo S-H, Khalifah P G, Grey C P and Ceder G 2014 Analysis of charged state stability for monoclinic LiMnBO₃ cathode *Chem. Mater.* 26 4200-6

- [235] Lin Z et al 2016 2D materials advances: from large scale synthesis and controlled heterostructures to improved characterization techniques, defects and applications 2D Mater. 3 042001
- [236] Tangi M et al 2017 Band alignment at GaN/single-layer WSe₂ interface ACS Appl. Mater. Interfaces 9 9110-7
- [237] Jo G et al 2010 Large-scale patterned multi-layer graphene films as transparent conducting electrodes for GaN lightemitting diodes Nanotechnology 21 175201
- [238] Chandramohan S et al 2013 Impact of interlayer processing conditions on the performance of GaN light-emitting diode with specific NiOx/graphene electrode ACS Appl. Mater. Interfaces 5 958–64
- [239] Seo T H et al 2011 Graphene network on indium tin oxide nanodot nodes for transparent and current spreading electrode in InGaN/GaN light emitting diode Appl. Phys. Lett. 98 251114
- [240] Avramescu A, Lermer T, Müller J, Tautz S, Queren D, Lutgen S and Strauß U 2009 InGaN laser diodes with 50 mW output power emitting at 515 nm Appl. Phys. Lett. 95 071103
- [241] Al Balushi Z Y *et al* 2016 Two-dimensional gallium nitride realized via graphene encapsulation *Nat. Mater.* **15** 1166–71
- [242] Zhao Q, Xiong Z, Luo L, Sun Z, Qin Z, Chen L and Wu N 2017 Design of a new two-dimensional diluted magnetic semiconductor: Mn-doped GaN monolayer Appl. Surf. Sci. 396 480-3
- [243] Singh A K and Hennig R G 2014 Computational synthesis of single-layer GaN on refractory materials Appl. Phys. Lett. 105 051604
- [244] Qin Z, Qin G, Zuo X, Xiong Z and Hu M 2017 Orbitally driven low thermal conductivity of monolayer gallium nitride (GaN) with planar honeycomb structure: a comparative study *Nanoscale* 9 4295–309
- [245] Guo Y et al 2018 N- and P-type ohmic contacts at monolayer gallium nitride-metal interfaces *Phys. Chem. Chem. Phys.* **20** 24239–49
- [246] Sucharitakul S, Rajesh Kumar U, Sankar R, Chou F-C, Chen Y-T, Wang C, He C, He R and Gao X P A 2016 Screening limited switching performance of multilayer 2D semiconductor FETs: the case for SnS *Nanoscale* 8 19050–7
- [247] Xin C, Zheng J, Su Y, Li S, Zhang B, Feng Y and Pan F 2016 Few-layer tin sulfide: a new black-phosphorus-analogue 2D material with a sizeable band gap, odd-even quantum confinement effect, and high carrier mobility *J. Phys. Chem.* C 120 22663–9
- [248] Li S, Xiao W, Pan Y, Jie J, Xin C, Zheng J, Lu J and Pan F 2018 Interfacial properties of monolayer SnS-metal contacts *J. Phys. Chem.* C **122** 12322–31
- [249] Zhou X, Hu X, Jin B, Yu J, Liu K, Li H and Zhai T 2018 Highly anisotropic GeSe nanosheets for phototransistors with ultrahigh photoresponsivity Adv. Sci. 5 1800478
- [250] Guo Y, Pan F, Ren Y, Wang Y, Yao B, Zhao G and Lu J 2019 Anisotropic interfacial properties of monolayer GeSe-metal contacts Semicond. Sci. Technol. 34 095021
- [251] Liu S-C, Mi Y, Xue D-J, Chen Y-X, He C, Liu X, Hu J-S and Wan L-J 2017 Investigation of physical and electronic properties of GeSe for photovoltaic applications Adv. Electron. Mater. 3 1700141
- [252] Zhou Y 2016 MX (M = Ge, Sn; X = S, Se) sheets: theoretical prediction of new promising electrode materials for Li ion batteries J. Mater. Chem. A 4 10906–13
- [253] Xu L *et al* 2017 Electronic and optical properties of the monolayer group-IV monochalcogenides MX (M = Ge, Sn; X = S, Se, Te) *Phys. Rev.* B **95** 235434

- [254] Zhao H, Mao Y, Mao X, Shi X, Xu C, Wang C, Zhang S and Zhou D 2018 Band structure and photoelectric characterization of GeSe monolayers Adv. Funct. Mater. 28 1704855
- [255] Vaughn D D II, Patel R J, Hickner M A and Schaak R E 2010 Single-crystal colloidal nanosheets of GeS and GeSe J. Am. Chem. Soc. 132 15170–2
- [256] Xue D-J, Tan J, Hu J-S, Hu W, Guo Y-G and Wan L-J 2012 Anisotropic photoresponse properties of single micrometersized GeSe nanosheet Adv. Mater. 24 4528–33
- [257] Wu J et al 2017 High electron mobility and quantum oscillations in non-encapsulated ultrathin semiconducting Bi₂O₂Se Nat. Nanotechnol. 12 530
- [258] Wu J, Liu Y, Tan Z, Tan C, Yin J, Li T, Tu T and Peng H 2017 Chemical patterning of high-mobility semiconducting

- 2D Bi₂O₂Se crystals for integrated optoelectronic devices *Adv. Mater.* **29** 1704060
- [259] Wu J, Tan C, Tan Z, Liu Y, Yin J, Dang W, Wang M and Peng H 2017 Controlled synthesis of high-mobility atomically thin bismuth oxyselenide crystals *Nano Lett.* 17 3021–6
- [260] Chen C et al 2018 Electronic structures and unusually robust bandgap in an ultrahigh-mobility layered oxide semiconductor, Bi₂O₂Se Sci. Adv. 4 eaat8355
- [261] Liu S et al 2019 Unusual Fermi-level pinning and ohmic contact at monolayer Bi₂O₂Se-metal interface Adv. Theory Simul. 2 1800178
- [262] Xu L et al 2019 Pervasive ohmic contacts in bilayer Bi₂O₂Se-metal interfaces J. Phys. Chem. C 123 8923-31



Jing Lu is a Professor at the Department of Physics, Peking University, China. He received his BS and PhD degrees from Peking University in 1990 and 1997, respectively. During 2001–2003, he was a JSPS postdoc fellow at Institute for Molecular Science, Japan. During 2005-2006, He was a visiting scholar at the Department of Physics, University of Nebraska at Omaha. He was selected as New Century Talent of Ministry of Education of China in 2008. During 2016-2018, he was the 'Hanjiang Scholars' Project Distinguished Professor at Shaanxi University of Science and Technology, China. He is focused on exploring the properties of the two-dimensional (2D) semiconductors-metal interfaces, 2D semiconductors MOSFETs, 2D materials optoelectronic devices, 2D magnetic material devices, and ion battery by using the first-principles calculation and quantum transport simulations. His personal homepage is at http://faculty.pku.edu.cn/lvjing/en/index.htm, and Research ID is at http://www.researcherid.com/rid/H-4248-2013



Feng Pan is a Chair-Professor, Founding Dean of the School of Advanced Materials Peking University Shenzhen Graduate School, Director of National Center of Electric Vehicle Power Battery and Materials for International Research, Shenzhen, China. He got his BS degree from the Department of Chemistry, Peking University, China, in 1985 and PhD degree from the Department of P & A Chemistry, University of Strathclyde, Glasgow, UK, with Patrick D. Ritchie Prize" for the best PhD in 1994. He has been engaged in fundamental research and product development of novel energy conversion and storage materials & devices. As Chief Scientist, He led 12 entities to win the National Key project of Material Genomic Engineering for Solid State Li-ion Battery in China in 2016. He has been selected as one of the 2018 winners of ECS Battery Division Technology Award. His personal homepage is at http://www.pkusam.cn/English/MembersInfo.html, and Google Scholar is at https://scholar.google.com/citations?user=OZJPZK8AAAAJ & hl=zh-CN.



Lin Xiao is the Director of Nanophotonics and Optoelectronics Research Center, Qian Xuesen Laboratory of China Academy of Space Technology. He got BS and PhD degree from the Department of Physics, Tsinghua University, in 2004 and 2009, respectively. As a Principal Investigator, he is engaged in the fabrication and basic understanding of nanomaterials and optoelectronic devices, with their potential applications in space technology and science. More information can be found at his Google Scholar: https://scholar.google.com/citations?user=LcnUO0sAAAAJ & ht=zh-CN



Yangyang Wang is an Associate Researcher in Qian Xuesen Laboratory of Space Technology, China Academy of Space Technology, Beijing. She received her BS degree at the Department of Physics from Central China Normal University, Wuhuan, China, in 2011, and then received her PhD degree in condensed matter physics from the Department of Physics, Peking University, China, in 2016. She has worked in Qian Xuesen Laboratory of Space Technology, China Academy of Space Technology, as a Research Assistant from 2016 to 2019 and as an Associate Researcher currently. She has been focusing on the research of electronic, optical, and transport properties of low dimensional materials and their potential electronic and optoelectronic application. More information can be found at her website: https://www.researchgate.net/profile/Yangyang_Wang5/research



Shiqi Liu is a PhD candidate at the Department of Physics, Peking University, China. She received her BS from the Department of Physics, Renmin University, China, in 2017. Her current research interest includes the ab initio device simulation of nanoscale materials. More information can be found at her Google Scholar: https://scholar.google.com/citations?hl=zh-CN & user=kwahpYoAAAAJ



Qiuhui Li is a PhD candidate at the Department of Physics, Peking University, China. She received her BS degree at the Department of Material Physics from Anhui University in 2016 and then received her MS degree at the Department of Physics from Beijing University of Posts and Telecommunications in 2019. Her research interests mainly focus on the electronic and transport properties of low-dimensional materials. More information can be found at her ORCID ID: https://orcid.org/0000-0002-4767-3523